Flexible Silicon Photodiode Probes for Diffuse Reflectance Spectroscopy

by

David Michael Miller

Department of Electrical and Computer Engineering
Duke University

Date:_____

Approved:

_____
Nan M. Jokerst, Supervisor

_____
Richard Fair

_____
Aaron Franklin

_____
Jeffrey Glass

_____
Gregory Palmer

Dissertation submitted in partial fulfillment of
the requirements for the degree of Doctor
of Philosophy in the Department of
Electrical and Computer Engineering
in the Graduate School of Duke University

2016

ABSTRACT

Flexible Silicon Photodiode Probes for Diffuse Reflectance Spectroscopy

by

David Michael Miller

Department of Electrical and Computer Engineering
Duke University

Date:_____

Approved:

_____
Nan M. Jokerst, Supervisor

_____
Richard Fair

_____
Aaron Franklin

_____
Jeffrey Glass

_____
Gregory Palmer

An abstract of a dissertation submitted in partial fulfillment of the requirements for the degree of Doctor of Philosophy in the Department of Electrical and Computer Engineering in the Graduate School of Duke University

2016

Abstract

The optical properties of biological tissue provide quantitative information about the physiological structure and chemical composition of a tissue sample. The investigation of tissue optical properties through Diffuse Reflectance Spectroscopy (DRS) is a rapid, non-invasive technique with extensive applications in healthcare diagnostics and therapeutics. Breast conservation surgery, a clinical practice performed for nearly 15,000 patients annually, requires accurate diagnosis of the tissue margin, the healthy layer of tissue surrounding the excised tumor. This margin assessment has traditionally been performed via post-operative pathology through one of multiple time-intensive processes that are performed after the surgery is completed. However, the margin assessment can also be rapidly performed by DRS, leading towards pathological evaluations concurrent with the excision surgery.

Presently, DRS probe designs are limited to laboratory settings. They include illumination and collection optical fibers, spectrometers, and CCD detectors, which all add to the complexity, cost, and size of a diagnostic system. Recently, DRS probes have been designed with Silicon photodetectors (Si PDs), including detector arrays that enable simultaneous DRS imaging of multiple tissue sites. The Si PDs reduce probe system complexity by replacing the cumbersome fiber-based collection probes and CCD detectors.

However, these monolithic Si PD probes are rigid and flat. When imaging non-planar tissue samples, a rigid probe may experience reduced accuracy from uneven tissue pressure and loss of contact with the tissue surface. A physically flexible DRS probe can improve sensing accuracy by conforming to a tissue surface with arbitrary curvature.

This thesis presents the design, fabrication, and test of flexible DRS Si PD probes constructed with thin film single crystalline silicon heterogeneously bonded to a flexible polymer substrate. The PDs have dark currents and responsivities comparable to high performance standard thickness Si PDs. The responsivity and zero bias dark current of the flexible PDs were evaluated while flat and while curved up to a 10 mm radius of curvature, with measured variations in responsivity (±0.61%) and dark current (±3 pA).

The flexible DRS probe was evaluated on benign and malignant breast tissue representative liquid phantoms. DRS measurements were performed with the flexible DRS probe on both liquid phantoms over a wavelength range of 470 – 600 nm at five radii of curvature: flat, 50 mm, 25 mm, 15 mm, and 10 mm. The optical contrast between the benign and malignant phantom DRS measurements ranged from 4.0-13.6% across all measured wavelengths for the flat test case and 5.9-15.5% while curved. For both phantoms at all wavelengths, the DRS signal increased in response to increasing curvature. The increase in reflectance signal ranged from 4.8-12.3% when the liquid phantom curvature was brought from flat to a 10 mm radius of curvature. The

experimental results were then compared to theoretical reflectance values generated through a forward Monte Carlo model. The mean error between experiment and theory was 2.33% for the benign phantom and 1.23% for the malignant phantom.

Pixel-to-pixel crosstalk, the portion of diffusely reflected light that enters the tissue near one PD but is detected at a different PD, was also evaluated using the same test setup as for the DRS signal. The crosstalk signal also increases due to curvature, with an increase of 33.2-40.0% across all measured wavelengths for the benign phantom. The experimental crosstalk signal for the benign phantom was compared to a forward Monte Carlo model with mean error of 4.85%. The crosstalk could not be measured on the malignant phantom due to lower reflected light levels that were below the noise floor of the PD.

The flexible Si PD probe presented herein shows promising results for optical tissue analysis and feature extraction on both flat and curved tissue surfaces. This flexible probe technology facilitates conformal tissue DRS imaging, potentially in a clinical diagnostic device.

Dedication

To my friends and family.

To my parents, Brian and Marcy, for providing for me and giving me a path.

To my brother, Jacob, for being my mentor and compatriot.

To Nicole, for her love, support, and understanding.

Contents

List of Tables

List of Figures

Acknowledgements

Thanks first to my advisor, Nan Jokerst, whose support and advice were key to my graduation. Her well-placed pressure gave me the drive needed to complete my research. Her positivity and humor have been particularly helpful when my PhD work appeared hopeless.

Thanks to the faculty at Duke, especially Dr. Richard Fair and Dr. Adrienne Stiff-Roberts, whose classes on semiconductor fabrication and quantum mechanics I took in my first year of graduate education here. The education I received from the Duke faculty has been top-notch, providing a foundation for continuation of my research.

Thank you to my dissertation committee, Drs. Richard Fair, Aaron Franklin, Jeffrey Glass, and Gregory Palmer, who have taken the time out of their schedules to offer me the opportunity to earn my degree.

Thank you to my lab group, who have, in spite of my terrible sense of humor, remained my friends. Talmage, for being the ultimate resource for any problems in the clean room. Ozlem, for leading the way and showing us all that graduation is indeed possible! Ben, for sitting right next to me and putting up with my complaints, jokes, incessant internet references, and still managing to offer sound advice ranging in topics from research to bicycles. Ugo, for always dressing better than me, for riveting discussions on politics, science, and current events, and for a sympathetic ear when I just needed to let it all out. Aditi, for her endless positivity, her tales from back home, and

her fantastic choices in fine dining. And Callie, who is always willing to lend a helping hand, and to insist that I'm not as bad at dancing as I think I am.

Thank you to the staff of Duke Shared Materials and Instrumentation Facility. Thank you to Dr. Mark Walters, who provided my very first introduction to the clean room and provided much needed assistance with a wide assortment of tools. Thank you to Jay Dalton, who treated me like a friend, and was always ready to help me fix the metal evaporator that I may have been responsible for inadvertently changing the pocket rotation order. Thank you to Kirk Bryson, whose experience and technical expertise saved me from hours and hours of process development on the tools that I needed for my research.

And finally, thank you to my friends and family. Thank you to my parents, my brother, and my sister-in-law, who are always on my side. Thank you, all of my friends I have made in my stay at Duke. And thank you Nicole, my partner in this struggle towards higher education, who relentlessly pushed me to succeed and provided much needed hugs.

1. Motivation and Objectives

This chapter offers motivation for the work presented in this thesis. Section 1.1 briefly discusses semiconductor optical sensors and thin film devices, including their usefulness in tissue optical diagnostics. Section 1.2 outlines the objectives of the thesis and the organization of each chapter.

1.1 Motivation of this Thesis

New methodologies and implementations for optical sensing are emerging, including the heterogeneous integration of multiple distinct materials onto a common substrate to form unique integrated systems. Characterization methods for tissue and other turbid media, realizable through these integrated systems, are powerful tools that can quantify optical properties, including absorption and scattering, which in turn can be used to identify underlying structure and biochemical composition. Optical sensing and imaging are typically performed with detectors such as semiconductor photodetectors and charge-coupled devices (CCDs). Traditionally, these devices have been rigid and flat, fabricated from relatively thick, hard semiconductor materials. The research reported herein focuses on implementing sensing and imaging devices for applications that may benefit from a flexible and conformal integrated optical implementation that utilizes both flexible substrates and flexible thin film photodetectors. These flexible detectors can be used for conformal sensing and imaging

of tissue, particularly when the surface of an interrogated tissue is curved or soft, as in the case of most excised human tissues.

One significant application of flexible photodetectors is to determine tissue optical properties, particularly the coefficients of absorption and scattering. By measuring the wavelength-dependent reflection from the surface of a tissue sample, and subsequently applying one of many optical parameter extraction methods, a photonic system can make a diagnostic evaluation of the tissue. This measurement technique is called Diffuse Reflectance Spectroscopy (DRS). Through DRS, biological tissue can be characterized to determine chromophore concentrations in skin, diagnose skin, oral, colon, and breast cancers, and perform intra-operative breast cancer margin assessment. Herein, the work in this thesis focuses on excised breast tissue analysis (*ex vivo*), but noninvasive optical tissue interrogation can also be performed externally or internally (e.g., through mounting a detector in an endoscope) on live subjects.

This thesis reports on the design, fabrication, and test of photodetector probes fabricated in thin film silicon from Silicon-on-Insulator (SOI) wafers. The detectors, once they are separated from their handle wafers, are thin film optoelectronic devices. The final device thickness is on the same order as that of the SOI wafer device layer. Additionally, due to the thin film mechanical structure, these devices can be mechanically flexible. For use in the systems described above, thin film photodetectors

were bonded to a host substrate to provide durability and to enable external electrical interconnection. Testing of these thin film photodetectors on flexible substrates shows that the photodetector performance, i.e. dark current and responsivity, are not degraded by the thin film fabrication process. In addition, herein it is proposed that flexible thin film photodetectors bonded to a flexible substrate can be successfully used for tissue sensing and diagnostic applications.

1.2 Objectives and Organization of this Thesis

The objective of this thesis is to develop a flexible DRS sensor probe with sensing accuracy on par to that of previously demonstrated sensors. The first actions toward this objective were the design, fabrication, and characterization of a flexible thin film silicon photodiode probe. The second goal was to use this probe to perform DRS signal measurements on turbid liquid phantoms representing benign and malignant breast tissue. Finally, the DRS measurements were compared to theoretical estimations of reflection generated by Monte Carlo simulations.

Chapter 2 of this thesis presents the background germane to the work herein. Section 2.1 discusses the current status of breast conservation surgery margin assessment. Section 2.2 provides an overview of Diffuse Reflectance Spectroscopy, and section 2.3 applies DRS to tissue identification and property extraction. Section 2.4 describes the theory behind semiconductor photodetectors. Section 2.5 introduces thin

film electronics. Section 2.6 discusses flexible semiconductors, Section 2.7 presents flexible substrates, and Section 2.8 covers flexible metallization, all necessary components of fully flexible electronics. Section 2.9 delves into the heterogeneous bonding of thin film semiconductors onto flexible substrates, and the challenges associated with flexible electronic circuits.

Chapter 3 discusses the design, fabrication, and characterization of the thin film flexible photodiode probe. The system design is addressed in section 3.1, including the selection of photodiode shape and size, material selection and layer design, and heterogeneous bonding. Fabrication of the flexible probe is covered in section 3.2.

In Chapter 4, the test results of the flexible probe are presented. In Section 4.1 the results of characterization testing is presented, both in a flat and cylindrically flexed state. Section 4.2 discusses the design of the test setup for DRS on curved liquid phantoms. Section 4.3 reports on the selection of the liquid phantom optical properties, representing both benign and malignant tissues. Section 4.4 presents and discusses the results of the DRS measurements.

Chapter 5 focuses on the optical simulations of the liquid phantoms. Section 5.1 discusses the modeling of turbid media. Sections 5.2 and 5.3 present the simulations of DRS signals and crosstalk signals, respectively.

In Chapter 6, the experimental and simulation results are compared and discussed. Section 6.1 discusses the comparison of the DRS signal, and Section 6.2 discusses the same for the crosstalk signal.

Finally, Chapter 7 concludes the thesis and provides a framework for future research in this field.

2. Background and Theory

This chapter discusses the scientific theory and previous research into tissue optics, imaging technology, and diagnostic methods that inform the work in this thesis.

2.1 Breast Conservation Surgery Margin Assessment

Nearly 400,000 cases of invasive breast cancer were diagnosed in U.S. women ages 40-85 in nine registry areas (CT, HI, IA, NM, UT, Atlanta, Detroit, San Francisco-Oakland, and Seattle) between 1975 to 2003, which corresponds to a rate of approximately 100 out of every 100,000 women [1]. While these incidence rates show a downward trend of 4.1% annually, breast cancer remains a widespread disease. Even with treatment, breast cancer is a potentially deadly disease; it is the leading cause of cancer deaths in women worldwide, with 458,000 deaths in 2008 [2].

For treating small breast cancer tumors, the standard treatment is lumpectomy followed by radiation therapy [3]. Breast conservation surgeries, including lumpectomies, remove less total tissue from a patient than a full mastectomy, but the surgery requires validation of a "negative margin", a layer of healthy tissue surrounding an excised sample [4]. There is some controversy regarding the recommended width of this negative margin. While some studies show that a negative margin width of at least 2 mm reduce the possibility of recurrence [5], others find no link between margin width and recurrence [6]. However, positive margins where carcinoma exists on the surface of

the excised tissue show a two-fold increase in the risk of recurrence [6]. Positive margins require re-excision surgery to fully remove the remaining cancerous tissue. These additional surgeries are reported for up to 70% of all patients [7]. Examination of the margin is usually performed by frozen section or touch preparation cytology. Frozen section is a time intensive process, and is usually performed off-site at a pathological lab, and the results are returned days after the initial surgery is complete. Frozen section biopsies require a pathologist to first freeze the tissue in a cryostat, cut sections with a microtome, apply stains with various dyes, and finally examine the sections under a microscope. In cases where margins are indeterminate from frozen section, a pathologist may instead elect to perform a permanent section biopsy, where the sections are fixated in solution and embedded in wax. The procedure time for permanent section requires, on average, an additional day over frozen section [8]. Touch prep cytology can only detect surface cancer, but does require less procedure time than frozen section. In touch prep cytology (also known as touch imprint cytology), a prepared glass slide is placed in contact with the sample tissue. The tissue smears that remain on the slide are fixed with alcohol and stained with dye. A pathologist then manually examines the slides under a microscope [9]. While touch prep cytology may be performed intraoperatively, the accuracy of margin assessment is decreased as compared to frozen section. Additionally, touch prep cannot detect carcinoma below the tissue surface. With these current

methods, accurate margins are determined after the surgery is complete, typically days after the patient has left the clinic. If further surgeries are deemed necessary, the patient may be required to return for a second surgery at a later date. Reexcision surgery is effective at reducing local relapses in patients, especially when margin assessment finds a positive (carcinoma tissue at the surface) or close (carcinoma near the surface) margin. For patients with close and positive margins, 96% of patients did not experience a local relapse after 10 years with reexcision surgery, compared to 76-78% for those patients who did not have additional surgery [10].

It is clear that accurate margin assessment, which may directly dictate the requirement for reexcision surgeries, is vital in reducing breast cancer recurrence rates. However, with every surgery, there is a non-zero risk of complications due to the surgery itself, especially risks due to anesthesia. In non-cardiac surgery, the 30-day mortality rate can exceed 1%, although this mortality rate is strongly dependent on risk factors, including diabetes and obesity [11]. While reexcision surgery reduces recurrence and mortality, there is a clear need to reduce the risk and cost of additional surgeries.

Rapidly detecting cancerous tissue at the excised tissue margin can reduce the number of additional surgeries required per patient. With DRS, the margin status can be examined in the UV-visible spectrum [12]. Reflectance data is taken at multiple wavelengths and multiple tissue sites. The composition of the tissue surface, and depth

up to 2.2 mm [13], can be determined from this reflectance data through extraction of the scattering and absorption properties. Based on these properties, the tissue may be identified as malignant or non-cancerous. This diagnosis can be made immediately after the first excision surgery, intraoperatively in the surgical clinic. With a rapid diagnosis of lumpectomy margins, the surgeon may then take additional shavings as necessary to achieve negative margins, negating the demand for a patient's return visit to surgery.

Recently, multiple DRS probes have been developed to meet the need for intra-clinical margin assessment. Early generations of DRS probes included fiber-based light sources and detectors. Illumination is provided to the tissue surface from a wideband light source, directed through a fiber optic bundle, and diffuse reflection is collected through optical fibers and coupled into a spectrophotometer and CCD or photodiode detector [13]. An example of an early generation DRS probe is shown in Figure 1.

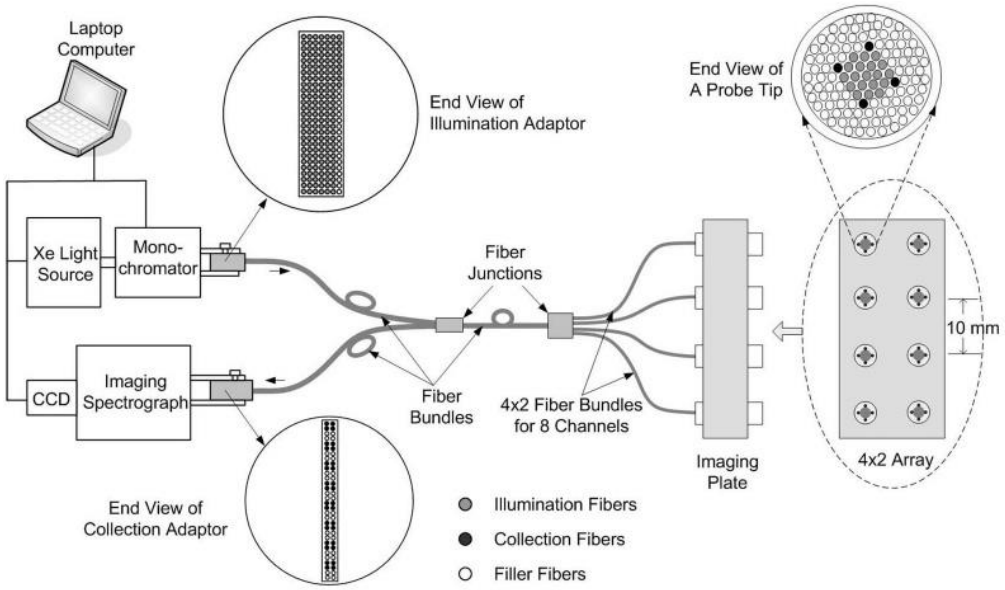

Figure 1. Block diagram of fiber-based eight channel DRS probe. Illumination and detection fibers are co-located in each fiber bundle [13].

The next generation of probe design removed with the collection fibers, replacing them with modified commercial photodiodes (PD) placed directly on the sample tissue. In this design, Yu *et al* demonstrated improved collection efficiency due to the increased numerical aperture (NA) and collection area of a semiconductor PD [14], shown in Figure 2. However, the DRS probe design was single-channel. To perform measurements on large margin areas (excised breast tissue areas often reach up to 20 cm^2), multiple probe placements are necessary.

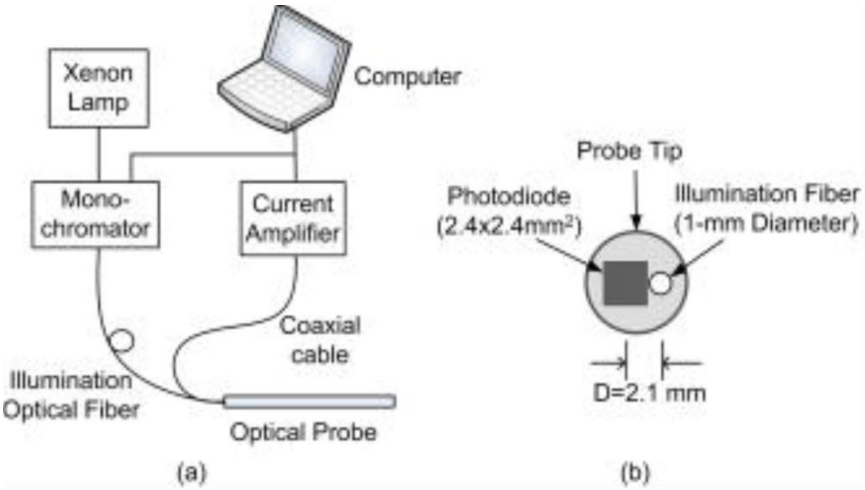

Figure 2. Schematic of (a) PD-based DRS probe, (b) probe tip, showing illumination fiber and collection PD [14].

Further improvements were reported by Dhar *et al* with a custom fabricated annular silicon PD array [15]. The custom array, shown in Figure 3, enabled higher resolution imaging as compared to the fiber based probe, and 16 measurement channels enabled rapid assessment of large tissue areas. The PD array demonstrated increased collection efficiency as compared to fiber-based detectors.

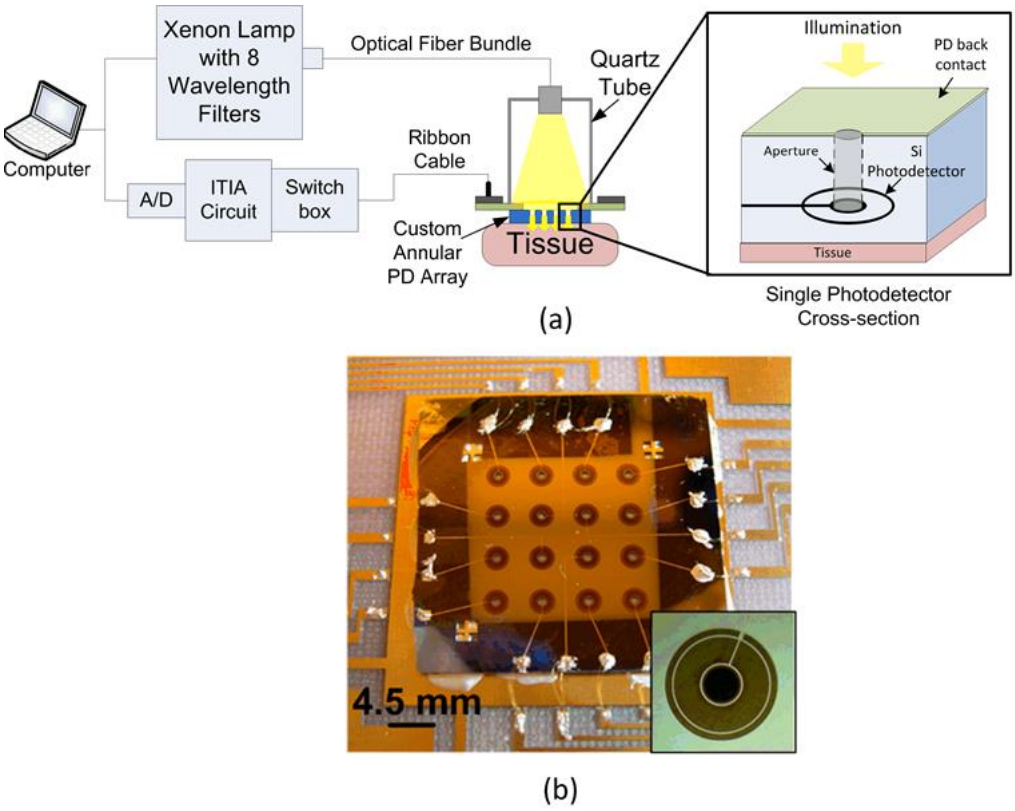

Figure 3. Custom silicon PD array probe (a) system schematic and (b) PD array surface, showing 16 annular photodiodes with individual light-delivery apertures [15].

Integrating traditional semiconductor fabrication techniques for measurement of biological tissue leads to a number of challenges. A rigid detector array constructed in bulk silicon cannot conform to an arbitrary non-planar tissue surface. When placed in contact, there may be high pressure regions (at tissue peaks) or air gaps (at tissue valleys), impairing the measurement error. To alleviate these sources of inaccuracy, the array is applied with sufficient force to homogenize pressure differences [16] or pressure sensors are utilized with the array [17]. Additionally, since the sensor contacts the tissue directly,

there is the risk of damage to the sensor surface, leading to weakened signal integrity and lower signal-to-noise ratio (SNR) exacerbated with higher probe pressure. Tissue contact may also leave behind a residue on the surface of the detection array. Biofouling of the sensor surface can create an opaque barrier, preventing reflection power from reaching the photodiodes. Cleaning the sensor of this blockage can also lead to damage when harsh chemicals or abrasives are necessary to completely clear the surface of tissue residue.

This thesis concentrates on overcoming the challenge of integrating traditional flat and rigid electronics with non-planar tissue by introducing a fully flexible DRS silicon photodiode sensor, as a part of an accurate, efficient, and miniaturized breast cancer margin assessment probe.

2.2 Diffuse Reflectance Spectroscopy

Diffuse reflectance spectroscopy (DRS) non-invasively measures the optical properties of various media, such as tissue. When illuminating a diffusely reflective sample, photons that interact with the media can return to the surface through scattering interactions. These photons can then be observed and measured with a photodetector. The optical intensity at the surface can be used to infer information about the wavelength-dependent absorption and scattering within the media. The extraction of these properties can be performed by methods that include a look up table that can be based upon a forward model of photon interactions. This forward model requires

knowledge of the biological tissue composition, particularly the probability of photon absorption and scattering events.

Tissues contains quantities of interaction centers, such as particles or organelles that scatter or absorb photons, that vary in location and density. The probability that a photon will be absorbed by the tissue is defined as the *absorption coefficient*, μ_a. Similarly, the *scattering coefficient*, μ_s, is the probability that a photon will scatter in the tissue. These coefficients are determined by the concentration of the tissue interaction centers and by the wavelength-dependent characteristics of their interaction with incident light. The absorption coefficients of the tissue chromophores can vary significantly over the visible wavelength range. For an example, the oygenated Hemoglobin (Hb), deoxygenated Hb, and beta-carotene absorption spectra are shown in Figure 4 [18] and Figure 5 [19].

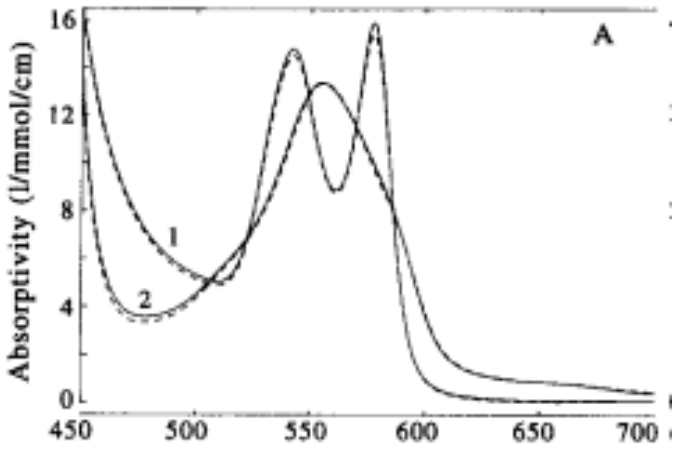

Figure 4. Oxygenated (1) and deoxygenated (2) Hb absorption spectra [18]

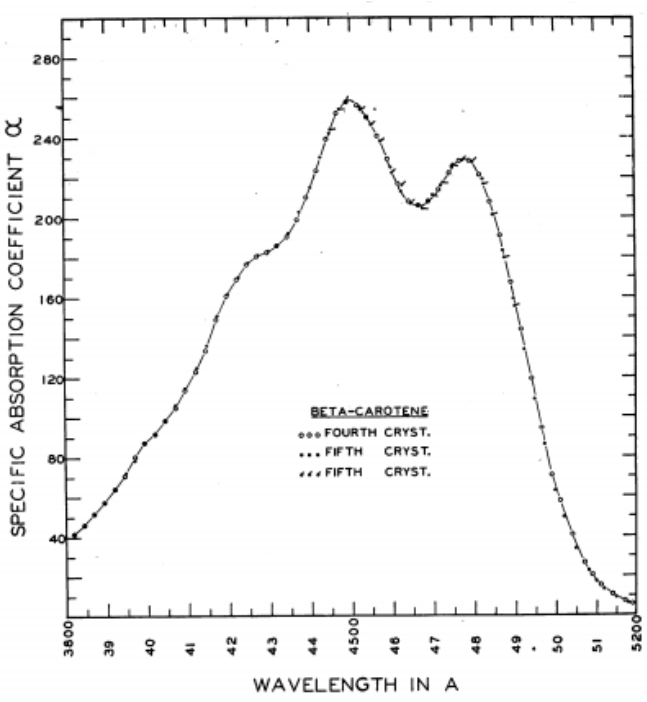

Figure 5. Beta-carotene absorption in hexane solution [19]

The absorption coefficient is measurable directly through transmission measurements. When light of intensity I_0 is incident on an absorbing media of path length L, the transmission fraction, T, is equal to I/I_0, where I is the measured transmitted intensity. The coeffiecient of absorption can be calculated with the following ratio [20]:

$$\frac{I}{I_0} = T = e^{-\mu_a L} \tag{2.1}$$

The transmission fraction can also be expressed in relation to chromophore concentration. An extinction coefficient, ε, is defined:

$$T = 10^{-\varepsilon CL} \tag{2.2}$$

where C is the molar concentration of the chromophore.

When tissue includes multiple chromophores (e.g. hemoglobin, melanin, bilirubin, beta-carotene), each chromophore additively contributes to the total absorption. For n distinct absorbing chromophores, the extinction coefficients, $\varepsilon_n(\lambda)$, and the concentration of absorbers, C_n, determine the total tissue absorption coefficient:

$$\mu_a(\lambda) = \ln(10) \sum_n \varepsilon_n(\lambda) c_n \tag{2.3}$$

The factor of ln(*10*) is introduced in the above equation from the traditional definition of the extinction coefficient in base 10 rather than base e.

Optical scattering occurs at the interface between media with a mismatch in index of refraction. Within biological tissue, scattering can originate from particles that have a different refractive index from surrounding material, or from a fluctuating background index [20]. The scattering coefficient is determined by the wavelength dependence and concentration of the scattering interaction centers. The scattering interactions are divided into Rayleigh and Mie scattering phenomena. Rayleigh scattering (or more precisely, Mie scattering at the Rayleigh limit) applies to particles much smaller than the wavelength of light, while Mie scattering is more appropriate for particles approximately the size of the wavelength of light. The effects of scattering from particles of differing sizes add linearly to the total scattering coefficient:

$$\mu_s = \sum_{i=1}^{M} \mu_s(d_i) \tag{2.4}$$

where $\mu_s(d_i) = \frac{\eta(d_i)}{v_i}\sigma(d_i)$, and $\eta(d_i)$ is the volume fraction of particles with diameter d_i, $\sigma(d_i)$ is the optical cross section of particles of diameter d_i, v_i is the volume of these particles, and M is the number of particle diameters [21].

Scattered light is deflected into a new direction with a scattering function $p(\psi,\theta)$, where ψ is the azimuthal angle and θ is the deflection angle. These scattering interactions are generally independent of the azimuthal angle. In bulk tissue, the total scattering interactions are averaged, which allows the azimuthal angle to be ignored. However, the deflection angle is highly dependent on the tissue properties and incident wavelength. The statistical average of the scattering is often given in terms of the *anisotropy factor*, g. For isotropic scattering, scattering is equally likely at all angles, and g can be ignored. In most tissue, scattering is anisotropic. The anisotropy factor g is defined as the average cosine of the scattering phase function [21]:

$$g_i = \int_{-1}^{1} \cos\theta \, P_i(\cos\theta) \, d(\cos\theta) = \langle \cos\theta \rangle \tag{2.5}$$

where g_i is the anisotropy factor of a particle of diameter d_i. The resulting total anisotropy, g, is the weighted sum of all g_i

$$g = \frac{\sum_{i=1}^{M} \mu_s(d_i) g_i(d_i)}{\sum_{i=1}^{M} \mu_s(d_i)} \tag{2.6}$$

In bulk tissue interactions, the *reduced scattering coefficient*, μ_s', is used to simplify photon propagation through many scattering events. The reduced scattering coefficient expresses the equivalent isotropic scattering from an anisotropic turbid media. It can be visualized as a random walk with uniformly distributed phase function with a mean free path of $1/\mu_s'$.

The relationship between scattering and reduced scattering coefficients is –

$$\mu_s' = (1 - g)\mu_s \tag{2.7}$$

The propagation of light in turbid media can be described by transport theory [22]: the radiance $L(\boldsymbol{r},\boldsymbol{s})$ (W-m^{-2}-sr) of light in at position $\boldsymbol{r}$, traveling in the direction $\boldsymbol{s}$, is attenuated by absorption and scattering events. These events occur with rates μ_a and μ_s, respectively. However, the radiance in the $\boldsymbol{s}$ direction is increased by light traveling in a different direction $\boldsymbol{s'}$ that scatters to $\boldsymbol{s}$. The scattered light is not immediately lost, as in the case of absorbed light. Scattering events have a probability to return the photons back to their original path through the turbid medium. These two separate events – loss of photons due to absorption or scattering away from the initial path, and the addition of photons scattered to the initial position and direction – together form the radiative transport equation. The radiative transport equation is –

$$\hat{s} \cdot \Delta L(\boldsymbol{r},\boldsymbol{s}) = -(\mu_a + \mu_s)L(\boldsymbol{r},\boldsymbol{s}) + \mu_s \int_{4\pi} p(\boldsymbol{s},\boldsymbol{s'})L(\boldsymbol{r},\boldsymbol{s'})\, d\omega' \tag{2.8}$$

Where $p(\boldsymbol{s},\boldsymbol{s'})$ is the phase function; the angular distribution of a scattering event. If $p(\boldsymbol{s},\boldsymbol{s'})$ is normalized to one, it is the probability that a scattering event originating in direction $\boldsymbol{s'}$ scatters to direction $\boldsymbol{s}$.

The radiative transfer theory fully describes the interaction of light radiance with absorption and scattering centers, but it is difficult to solve for biological tissue. In tissue, the interaction centers are randomly dispersed and inhomogeneous. In place of the analytical solution, numerical approximations are used to analyze the surface intensity as a function of tissue composition (μ_a and μ_s) and wavelength of incident light. A ray-tracing optical model simulates discrete scattering and absorption events for each ray launched into the tissue. The probability of ray destruction (absorption) or scattering events is determined by the absorption and scattering coefficients, which must be known before the simulation is performed. Additionally, the phase function in diffuse tissue cannot be solved analytically. It is instead calculated as a statistical distribution. For tissue optics, the Henyey-Greenstein phase function is commonly chosen [22]. The scattering angle is generated with the following function:

$$\cos(\theta) = \frac{1}{2g}\left\{1 + g^2 - \left[\frac{1 - g^2}{1 - g + 2g\zeta}\right]^2\right\} \tag{2.9}$$

where ζ is a uniformly distributed random variable. In isotropic scattering, the scattering angle is uniform over the range 0-2π.

Diffuse reflectance theory is effective at describing the transport of light in turbid media, and has a well-established history in analyzing optical interactions with tissue. The following sections of this chapter will discuss how DRS measurements can be made on biological samples, and how the examination of those measurements can provide tissue characterization that can inform medical diagnoses.

2.3 Tissue Diagnostics Through DRS

The DRS system design traditionally includes a broad-band white light source, illumination and collection probes, a spectrograph, and CCD detector. An example of this system design is depicted in Figure 6 [23].

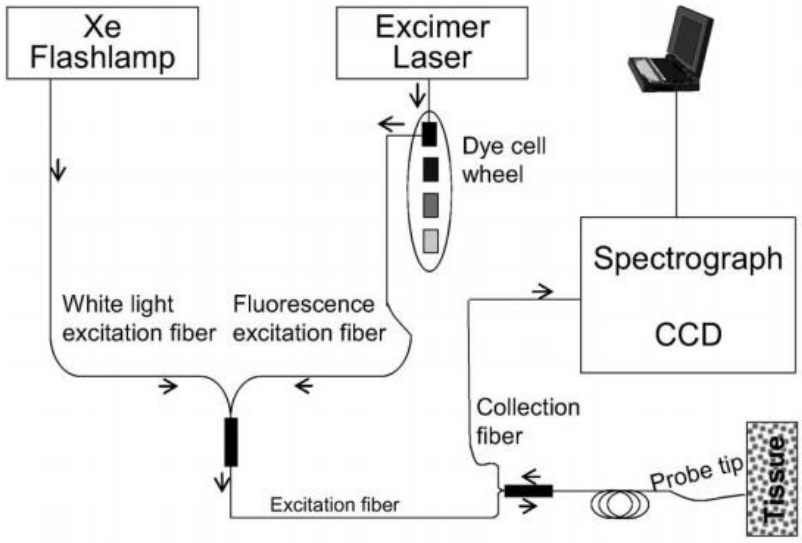

Figure 6. The design of a spectrophotometer for both DRS and fluorescence spectroscopy. A fiber probe is used to illuminated a tissue sample with a broadband light source, and collection fibers deliver the diffuse reflectance to a spectrograph, which is imaged onto a CCD detector [23]

The light source illuminates a tissue sample while optical fibers collect the reflected power at multiple wavelengths. The fiber output, incident upon the detectors, provides reflectance data that is analyzed to determine the tissue optical properties. Commonly reported DRS probe designs include fiber-based light sources and detectors, where the collection fibers are either concentrically located around the source fiber [23]–[31], or separated by varied distances [31]–[33]. These two probe designs are shown in Figure 7 [26], [33].

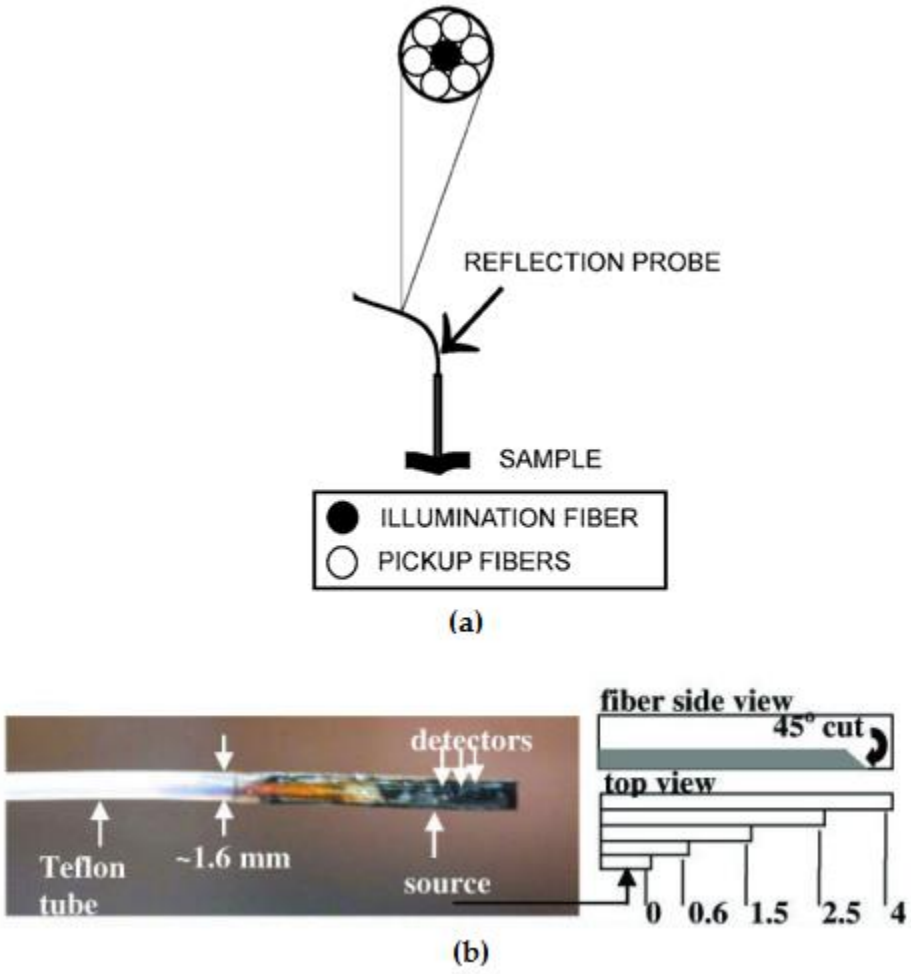

Figure 7. Fiber-based probe designs. (a) Single source fiber with concentrically located collection fibers [26], (b) single source with multiple, varied distance collection fibers [33]

However, fiber based probes limit the collection efficiency of the system. The fiber numerical aperture (NA), fiber cladding, and circular cross section reduce the total optical power that reaches the CCD detector, even in tightly packed fiber bundles. The

cross-section of a typical packed fiber probe is shown in Figure 8, [23] with areas that do not collect reflected optical power highlighted in red (highlighted by this thesis author).

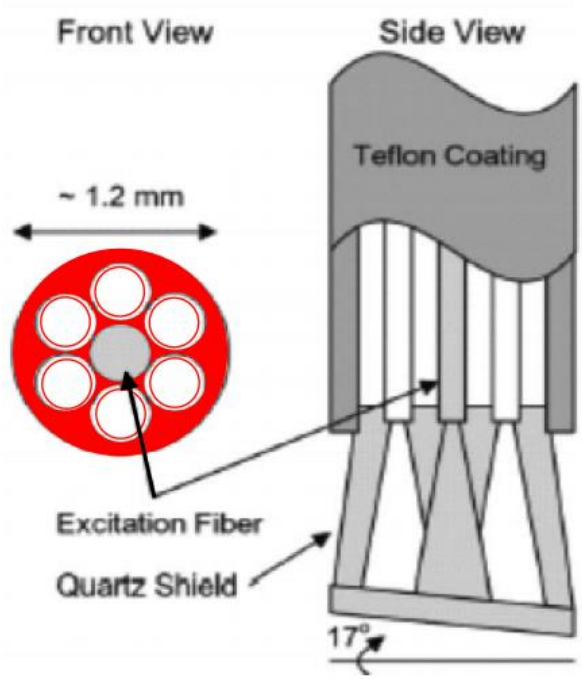

Figure 8. Tightly packed DRS fiber probe bundle [23]. Red highlighted areas (highlighted by this thesis author) illustrate the reduced collection area from fiber cladding and gaps between fibers.

To increase the collected optical power, photodetectors (PDs) may be placed directly on the tissue sample, as Yu *et al* demonstrated with modified commercial silicon (Si) PDs [14]. The collection efficiency of a Si PD-based probe is improved due to the higher NA of the Si PD (NA≈0.96), as compared to a traditional optical fiber (NA=0.22-0.39). The single PD probe can also be scaled to a larger Si PD array, enabling simultaneous measurement of multiple sites on a tissue sample. Fu *et al* demonstrated a

3x3 detector array created from commercial Si PDs (Hamamatsu S1337-BR) [34]. Tissue illumination was provided through central apertures mechanically drilled in the center of each PD. This array was limited in pixel density by the size and packaging of the commercial PDs, which limited the scalability and resolution of this probe design. The Jokerst group (Dhar *et al*) designed and fabricated a 4x4 array of custom, annular Si PDs with central illumination apertures [35]. Photolithographic techniques defined the PD size, shape, and pixel-to-pixel distance, enabling precise customization of the probe geometry. The image resolution for this DRS probe was limited only by crosstalk minimization, which sets a lower limit on the pixel-to-pixel separation. The crosstalk is the reflectance signal measured at a PD due to tissue illumination through the center apertures of surrounding PDs. Figure 9 is a schematic of this concept.

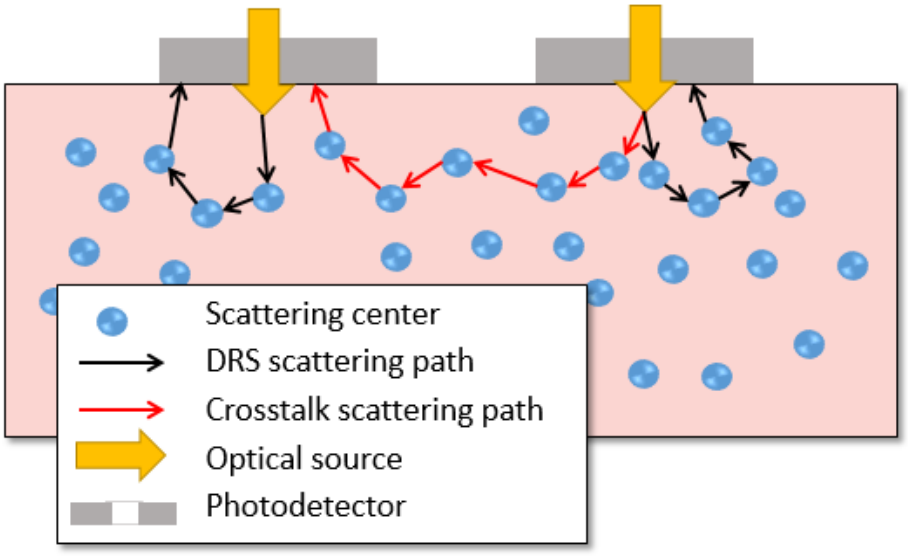

Figure 9. Schematic representation of crosstalk in DRS. The crosstalk signal is generated from illumination at surrounding PDs that is reflected to the PD of interest.

Increasing the pixel density by decreasing the pixel to pixel spacing decreases the signal-to-noise ratio due to an increase in crosstalk from neighboring pixels. Higher resolution imaging, reported by Nichols *et al*, can be achieved through multiple probe placements on a single sample [16]. Repeated samples are taken by moving the imaging array in the X-Y plane by a fraction of the pixel-to-pixel distance. This technique improves the resolution from the array pixel-to-pixel spacing (4.5 mm) to sub-millimeter (0.75 mm).

The spatial distribution of the DRS signal can reveal additional tissue characteristics as a function of photon path length. Longer photon paths typically travel deeper into the tissue. Separating the diffuse reflectance signal spatially, by distance to

the optical source, enables the recovery of depth information. In both the fiber and photodetector DRS probes discussed thus far, the reflectance signal consists of photons from all tissue depths that return to the surface. A large collection area increases the received reflection signal, but loses the photon path information. To collect spatial information in the DRS signal, Hillman *et al* developed a steered-mirror laser system that created a raster-scanned image of the tissue sample [36]. Another approach by Cen *et al* is comprised of a camera and imaging spectrograph for hyperspectral imaging, which captures spatial and spectral components of the tissue reflection simultaneously [37]. Previously, the Jokerst group (Senlik *et al*) have applied the advantages of the photodetector-based probes to spatially resolved DRS with a concentric multi-pixel array (CMPA) probe [38]. This probe consists of 24 individual photodiodes arranged concentrically around a single illumination aperture. Each detector collects the diffuse reflection from various photon path lengths, enabling the recovery of depth information and tissue layer analysis [39].

2.3.1 Margin Assessment

To determine tissue composition, the surface reflection intensity is measured, but the coefficients μ_a and μ_s are not typically known. Extracting these coefficients is essential for studying tissue. Forward tissue models calculate the reflection from known optical properties. Generating the absorption and scattering coefficients from the

reflection data is an inverse problem. The extraction of these values can be performed by comparing the reflectance data to a previously calculated table [40]–[42], or to a model based on the diffusion approximation [43], [44], or Monte Carlo simulations [24], [45]–[47]. These optical parameters provide quantitative information about the tissue sample, which research has shown can determine chromophore concentrations of skin [25], diagnosis of skin cancers [32], detect oral [26], [27], colon [28], [33], and breast cancer [23], [45], and perform intra-operative breast cancer margin assessment [29], [30].

Interpreting the diffuse reflectance measurements as absolute changes in optical properties is prone to error – for example, an increase in reflected intensity may be due to a decrease in absorption, an increase in scattering, or both. Separating the effects of absorption and scattering coefficients requires solving the inverse problem. With a high number of reference samples, a lookup table (LUT) approach can be used to extract tissue properties [41]. Tissue diagnoses are performed by comparing reflection data to a table of previously measured phantoms with known μ_a and μ_s'. The effect of probe geometry is built into the model, as the initial phantom measurements are carried out with the same probe used on tissue. However, the LUT technique is limited by the range of phantoms in the table, and by the initial accuracy of the phantom measurements. Additionally, any changes to the DRS probe would require a new set of phantom measurements with that probe.

With the goal of a more general analytical solution, Zonios *et al* demonstrated an extraction technique based on the diffusion approximation for identifying hemoglobin saturation, oxygenation, and scatterer properties of adenomatous colon polyps [28]. In this technique, only hemoglobin was assumed to be present as an absorber, and the scattering coefficient was assumed to decrease monotonically with increasing wavelength. The same diffusion model based approach was later extended to include melanin in addition to hemoglobin in recovering the concentration of both chromophores [25]. However, the diffusion approximation is valid for scattering-dominant tissues with low absorption, particularly in the NIR range where hemoglobin absorption is very low [46]. Additionally, the diffusion approximation is invalid for small source-detector separations – it assumes long photon transit paths, which do not occur for highly absorbing tissue or over small distances.

For a more general extraction method, an inverse Monte-Carlo technique can determine tissue optical properties over a wider range of absorption and scattering coefficients, and thereby model diffusion properties over the UV-VIS-NIR optical spectrum. In the process developed by Palmer *et al* [46], [47] a number of Monte-Carlo simulations of diffuse reflectance were performed. Inputs into the model included the concentrations of absorbing chromophores, the absorption spectra for each chromophore, and the size and density of scattering particles. Diffuse reflectance was

calculated for each set of inputs. To reduce the computational complexity, a scaling factor was introduced to allow a small set of simulations to cover a wider range of absorption and scattering concentrations. To calculate tissue properties from measured reflectance data, the inverse model was used to iteratively approach the solution. An initial assumption of tissue properties was made, and the simulation produced reflectance data. The simulated and measured reflectance was compared, and a Gauss-Newton least squares optimizer produced a new set of assumed tissue properties. The new properties were fed through the forward model, producing a new simulated reflectance, and the comparison with measured data was repeated.

In breast cancer, the differences between normal and malignant tissue can be classified through their optical properties. The extracted optical parameters, recovered through the inverse Monte Carlo method discussed previously, for a single patients' malignant and normal adipose tissue are shown in Figure 10 [45].

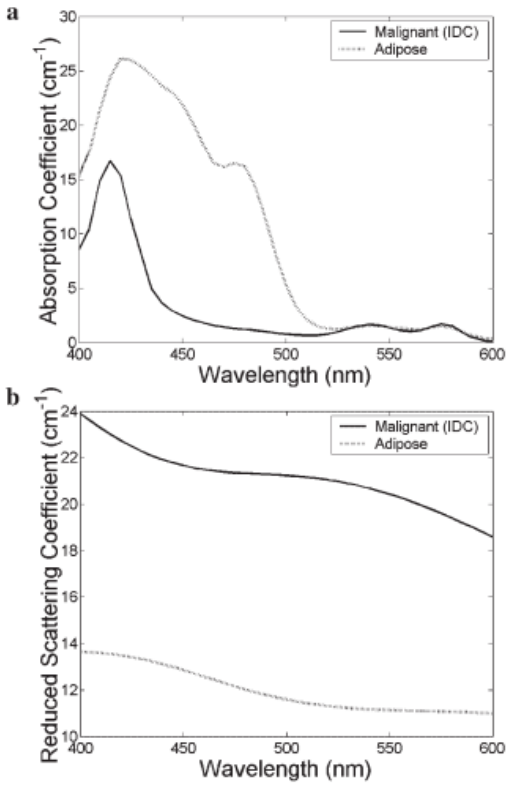

Figure 10. Extracted (a) absorption and (b) reduced scattering coefficients for malignant (invasive ductal carcinoma) and normal adipose tissue [45]

The concentrations of individual chromophores (beta-carotene, oxygenated Hb, and deoxygenated Hb) are obtained directly from the inverse Monte Carlo method. These concentrations for malignant, non-malignant fibrous, and non-malignant adipose breast tissue are shown in Figure 11. The concentrations of oxy- and deoxy-Hb are not displayed individually, rather as a ratio of blood saturation [45].

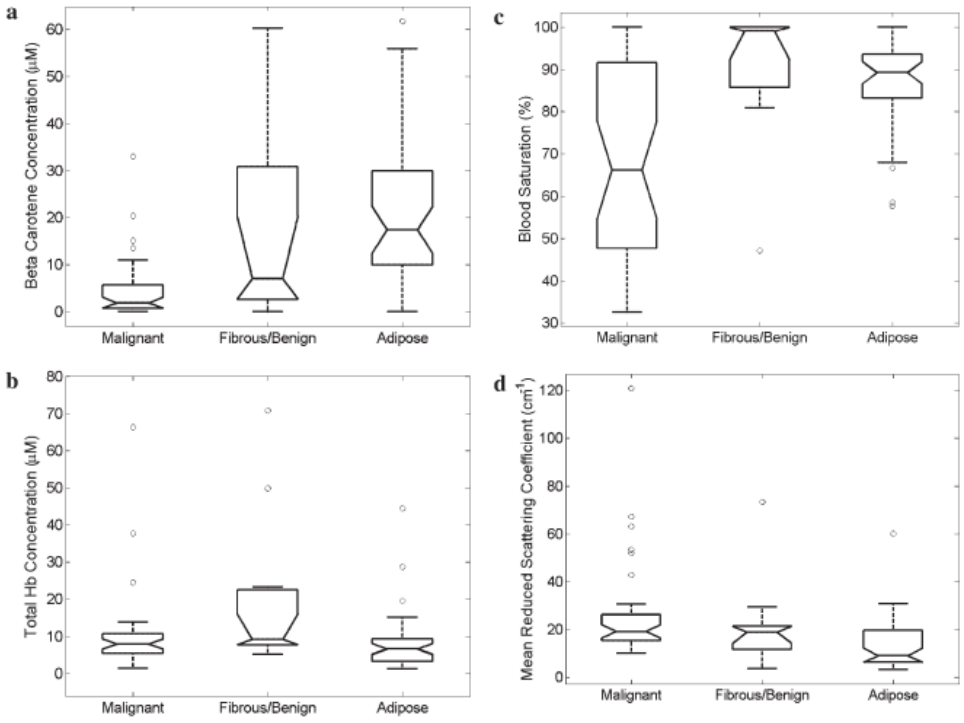

Figure 11. Concentrations of (a) beta-carotene, (b) total Hb, (c) Hb oxygen saturation, and (d) mean reduced scattering coefficient for malignant, non-malignant fibrous, and non-malignant adipose breast tissue [45]

A determination of malignancy in breast tissue can be made by examining the DRS data and extracted optical parameters. With only the concentration of beta-carotene and the mean reduced scattering coefficient, a diagnosis of malignant breast tissue can be made with sensitivity of 83% and specificity of 78% [45].

2.3.2 DRS Probe Pressure on Tissue

When imaging non-planar tissue samples, using a rigid probe (PDs or fiber) can lead to inaccurate DRS measurements. Many imaged tissue specimens are small or uneven, including excised breast tissue, with cancerous regions often varying from 1.4-

1.7 cm in diameter [48], [49]. When a rigid probe comes into contact with non-planar biological tissue, peaks and valleys in the tissue can create regions of varying pressure or non-contacting gaps between the tissue surface and detector plane. At high pressure regions, there can be a loss in DRS signal accuracy, as pressure affects the measured optical properties of local tissue regions [50]–[52]. An example of a change in reflectance and extracted optical properties of biological tissue due to applied probe pressure is shown in Figure 12 [51].

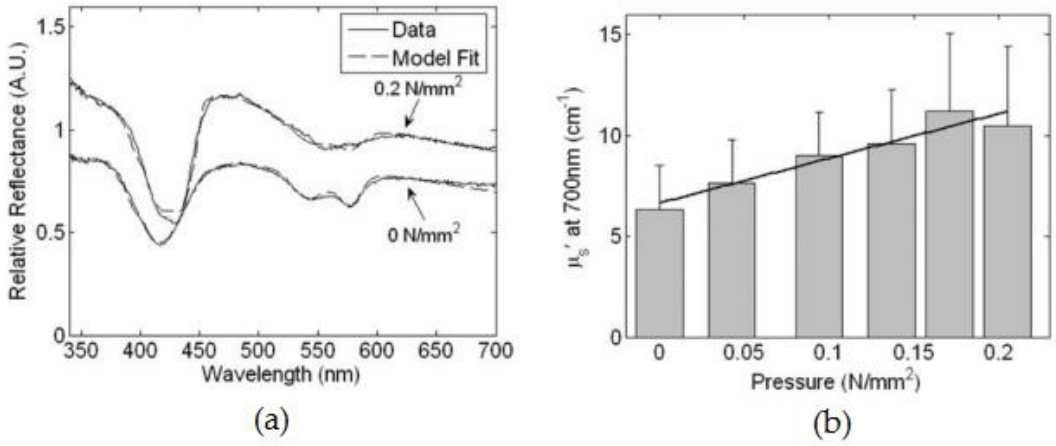

Figure 12. Example of (a) reflectance data and (b) extracted reduced scattering coefficient on mouse thigh tissue with increasing probe pressure [51].

2.4 Silicon Photodetectors

Photodetectors are used herein to measure the diffusely reflected light from an absorbing and scattering medium. Photodetectors convert incident absorbed optical power to electrical current. Photodetectors are used extensively in biomedical optics applications – the choice of detector is determined based upon the application

requirements, including size, wavelength range, light intensity range, and response speed.

In semiconductors, an absorbed photon is converted to electrical current by the promotion of an electron from the valence band to the conduction band, which generates free carriers. The free carriers are then separated and transported away from the point of absorption, and extracted to external contacts on the semiconductor device. This process of free carrier generation, separation and transport, and finally extraction, creates an electrical current from the PD that can be measured to determine the intensity of light on the surface of the PD.

A PN photodetector is built from a semiconducting material with a junction between a P-doped and an N-doped region. Under optical illumination, absorbed incident light generates free electrical carriers at the optical generation rate, G_0 –

$$G_0 = {\eta_i P_0}/{h\lambda} \tag{2.10}$$

Where η_i is the internal quantum efficiency, P_0 is the incident optical power on the surface, h is the Plank constant, and λ is the optical wavelength. The internal quantum efficiency is the fraction of absorbed photons that creates electron-hole pairs, and is usually close to unity in high quality semiconductor devices. However, photons are only absorbed by a PD if the optical energy of a photon $\left(E_{ph} = \frac{hc}{\lambda}\right)$ exceeds the electronic bandgap of the semiconductor, E_g.

As free carriers are generated in a PN photodetector, the distribution of free carriers causes diffusion currents for both the holes and electrons, and drift causes the carriers to separate across the junction. The total photocurrent density is given by [53]:

$$J_{ph} = -qG_0(L_p + L_n) \tag{2.11}$$

The diffusion lengths for electrons and holes, L_n and L_p, are defined as [53]:

$$L_n = \sqrt{D_n \tau_n}, L_p = \sqrt{D_p \tau_p} \tag{2.12}$$

where D_n and D_p are the electron and hole diffusion constants, and τ_n and τ_p are the electron and hole lifetimes.

The total current of a PN photodetector can be found by including the current-voltage relationship of a PN junction diode. In a diode, the diffusion of carriers across the junction is governed by drift and diffusion currents. At equilibrium, the diffusion current is balanced by the drift current, with a built-in potential of the depletion region. The built-in voltage, V_{bi}, is given by [53]:

$$V_{bi} = \frac{k_B T}{q} \ln\left(\frac{N_A N_D}{n_i^2}\right) \tag{2.13}$$

Where N_A and N_D are the acceptor and donor impurity concentrations, n_i is the intrinsic carrier concentration, k_B is the Boltzmann constant, and T is the temperature. The depletion region near the junction, or the space charge region, provides the only non-zero charge densities at equilibrium. Inside the depletion region, the charge density

is equal to either qN_D (N-side) or qN_A (P-side). The width of the depletion region is given by [53]:

$$W = \sqrt{\frac{2V_{bi}\epsilon}{q}\left(\frac{1}{N_A}+\frac{1}{N_D}\right)} \tag{2.14}$$

The total current in a diode can be solved by applying the continuity equations for charge density to the transport of minority carriers at the edge of the depletion region. The current density in a diode is a function of the applied voltage is as follows [53]:

$$J(V) = J_0\left(e^{qV/k_BT}-1\right) \tag{2.15}$$

Where J_0 is the diode reverse saturation current, $J_0 = -q\left(\frac{D_p p_{N0}}{L_p}+\frac{D_n n_{P0}}{L_n}\right)$ [53]. P_{N0} and N_{P0} are the hole and electron concentrations at the n-type and p-type edges of the depletion region, respectively.

The total current density in a PN photodetector is the sum of the diode current density and the photo-generated current density [53]:

$$J_{tot}(V) = J_0\left(e^{qV/k_BT}-1\right) - J_{ph} \tag{2.16}$$

The responsivity of a photodetector, $R(\lambda) = I_{ph}(\lambda)/P_0(\lambda)$, [53] relates the generated photocurrent to the incident optical power. The external quantum efficiency, η_e, is the fraction of photons that are converted into charge carriers outside the device.

The external quantum efficiency is related to the responsivity with the following relationship [53]:

$$R(\lambda) = \frac{\eta_e q \lambda}{hc} \tag{2.17}$$

The external quantum efficiency includes losses due to reflection at the surface, an internal quantum efficiency less than unity, and from photon absorption outside the depletion region. The external quantum efficiency is given as [53]:

$$\eta_e = \eta_i(1 - \Theta_R)(1 - e^{-\alpha W}) \tag{2.18}$$

Where Θ_R is the surface reflection, η_i is the internal quantum efficiency, and α is the absorption coefficient. The absorption coefficient is a wavelength dependent parameter in semiconductors. High external quantum efficiencies are possible with an appropriate anti-reflective coating to minimize Θ_R and sufficient absorbing thickness for the wavelength of incident light.

2.5 Thin Film Detectors

Thin film semiconductor photodetectors provide a miniature, highly integrated, and flexible alternative to bulk semiconductor technology. In particular, the flexibility of thin film devices is of importance to the research described herein. Thin film semiconductor photodetectors have been successfully integrated with waveguides [54], microfluidic systems [55], photonic ICs [56], and DNA sensing [57]. Thin film devices

can also provide high speeds and low dark current as compared to bulk semiconductor devices [58].

Moving from a bulk semiconductor to a thin film semiconductor presents a new challenge to the device performance: the surface to volume ratio is drastically increased. In semiconductors, recombination events can occur either in the bulk or on the surface. The surface provides additional trap states at the interface between the semiconductor and an external medium (e.g. air, passivation, protective coating). These unwanted trap states provide sites for non-radiative recombination. The Shockley-Read-Hall recombination theory characterizes this recombination as a Surface Recombination Velocity (SRV). The SRV is expressed as $s_r = \frac{R_s}{\Delta n_s}$, [53] where R_s is the surface recombination rate, and Δn_s is the excess minority carrier density. The SRV is strongly dependent on the material bulk and surface quality and surface cleanliness. The effective carrier lifetime, assuming a constant bulk recombination rate and a constant surface recombination rate, is dependent on numerous factors, including the device thickness. As demonstrated in Figure 13, when the device becomes thinner surface effects can dominate [59].

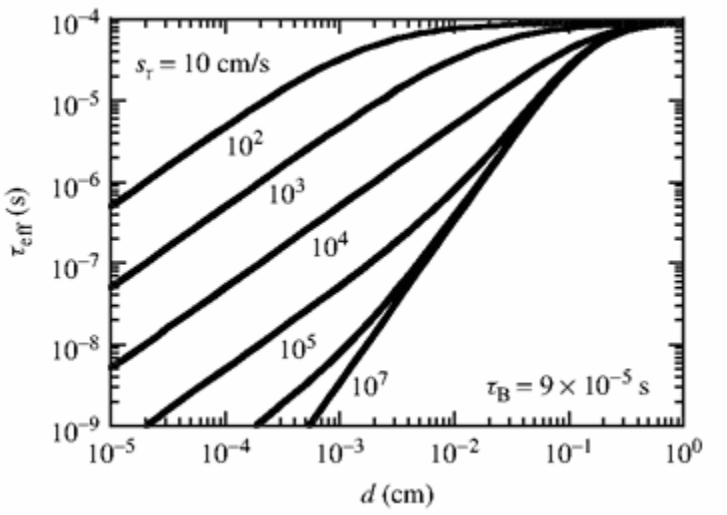

Figure 13. Effective carrier lifetime τ_{eff} vs. wafer thickness d as a function of SRV [59]

By using a surface passivation layer, such as SiO_2 or Si_3N_4, the SRV can be reduced. This termination layer suppresses trap states at the surface, lowering the surface recombination rate.

Numerous optoelectronic devices have been constructed using thin film semiconductors. A stamp-transfer method, which moves thin film membranes on a PDMS stamp from the source wafer to a heterogeneous substrate, has been used to create sparse arrays of bar-shaped solar cells. The thin film cells, etched into bulk <111> wafers, were transferred to a photocurable polymer. The thin film solar cells did not significantly degrade with repeated bending tests. A solar cell micro-bar is shown in Figure 14 [60].

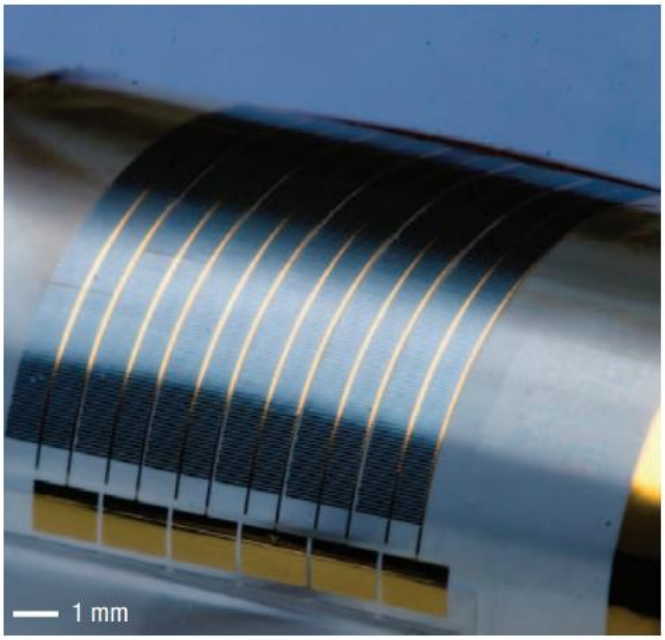

Figure 14. Flexible silicon solar cell micro-bar array [60]

Thin film photodetector arrays have also been transferred to alternative host substrate surfaces. The figure below shows a matrix-connected array of silicon photodetectors. This array was placed on a hemispherical glass surface, creating an "electronic eye". The photodetectors were constructed on SOI wafers, and the device layer was etched to create a planar array. A hemispherical PDMS stamp was stretched flat to pick up the array from the SOI wafer, then allowed to relax to deposit on the glass surface. The finished "hemispherical eye" camera is shown in Figure 15. In this device, the final array was not flexible – it was affixed to a rigid surface – but the same processing steps can be used with a flexible material to create flexible arrays [61].

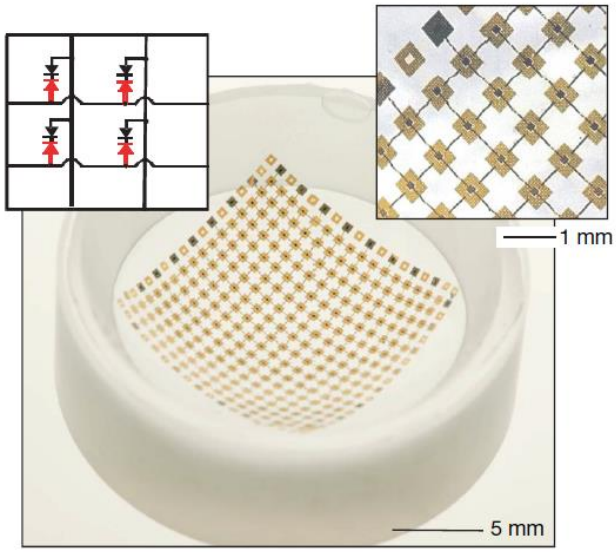

Figure 15. Hemispherical thin film photodetector array [61]

Previous research in the Jokerst group has demonstrated thin film photodetectors bonded to rigid Pyrex substrates. The detectors were designed for use in biophotonics imaging, specifically diffuse reflectance spectroscopy. Vertical PN junctions were doped into a SOI wafer, which was etched to create mesas. These mesas were separated from the handle and bonded via thermocompression to a gold-clad Pyrex carrier, shown. The high responsivity (0.19 to 0.34 A/W for 470-600nm) and low dark current density (0.63nA/cm^2) allowed these detectors to achieve high signal-to-noise ratio in a DRS application [62]. A photomicrograph of two bonded photodetectors is presented in Figure 16.

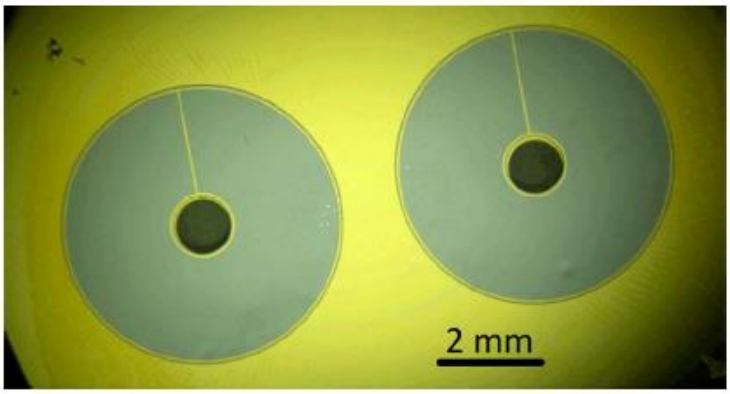

Figure 16. Thin film Silicon PDs bonded to Pyrex substrate [62]

The performance of these thin film detectors showed no significant degradation when compared to a similar thick silicon device. The thick silicon devices achieved responsivity of 0.28 A/W – 0.37 A/W for λ= 470 nm – 600 nm, and dark current densities of 1.456 nA/cm^2 – 4.48 nA/cm^2. The Jokerst group has demonstrated a 4x4 array of these thin film photodetector arrays bonded to Pyrex, as shown in Figure 17.

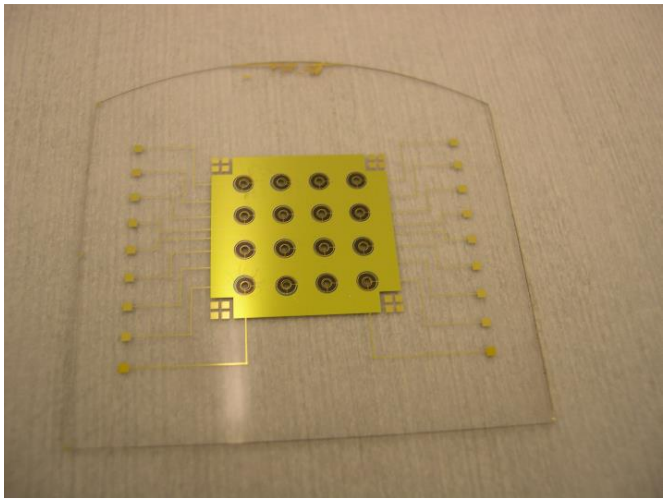

Figure 17. Thin film detector array on Pyrex

These thin film Si PD arrays have the highest uncooled responsivity to dark current ratios for thin film silicon photodiodes to date. [62].

2.6 Flexible Semiconductors

Flexible semiconductors must be constructed from flexible materials. Unfortunately, standard thickness (approx. 300 μm – 600 μm) crystalline semiconductors, like silicon, tend to be inflexible and brittle. These materials exhibit a high elastic (or Young's) modulus, the relationship between force and deformation. In silicon, the Young's modulus ranges between 130-188 Gpa, depending on the crystalline plane [63]. Additionally, crystalline semiconductors such as silicon have a low fracture strength, again depending on the crystalline plane. Silicon's fracture strength has been measured at 140-900 Mpa [64]. Using the relationship $\sigma = \varepsilon E$, where σ is stress (Pa), ε is mechanical strain (unitless), and E is the Young's modulus (Pa), the fracture strain for silicon is as low as 0.07-0.6%. In contrast, a naturally flexible material has a much lower elastic modulus. In comparison, poly(dimethylsiloxane) (PDMS), a widely-used elastomer in the microelectronics industry, has an elastic modulus of 360-870kPa [65] and yield stress between 0.9-1.75Mpa, which allows for a strain of 125% to 210% before fracture occurs [66].

When silicon is produced or fabricated in thin film form, the material is flexible. The strain applied to a bending beam can be expressed as $\varepsilon = \frac{d}{2r}$ [67], where d is the

material thickness and *r* is the radius of curvature. With a traditional bulk silicon wafer at 600 μm thickness, the radius of curvature at 0.1% strain is 300 mm. When a thin film device of only 10 μm thickness is used, that same 0.1% strain is reached at a 5 mm radius of curvature. Thinning the silicon allows it to bend to tighter radii without fracture from excessive stress.

Thin film silicon can be produced from bulk silicon wafers by mechanically or chemically removing the bulk silicon material. After completing fabrication on a thick substrate, the wafer is bonded to a carrier with tape or wax. The exposed wafer backside is thinned by mechanically grinding, wet chemical etching, dry plasma etching, or a combination of those methods. The resulting silicon dies can then be released from the temporary carrier. This method can produce device thicknesses in the tens of microns [68].

Thin film semiconductor materials can also be produced through selective etching. In this process, the substrate material is grown or fabricated (often through bonding) with multiple layers of materials with different etch rates, such as $Al_xGa_{1-x}As$ with varying concentrations of Al, built into the epitaxial growth structure on a GaAs substrate. The etch rate in HF is much higher in AlAs than $Al_xGa_{1-x}As$ ($x<0.4$) [69], and the AlAs layer can be selectively etched, releasing the epilayers located above the AlAs layer. Similarly, thin film semiconductors can be produced from Silicon-on-Insulator

(SOI) wafers. The SOI wafer includes a thick handler layer (usually silicon), a thin film silicon dioxide layer, and finally a thin film silicon device layer. For traditional rigid microelectronics, the thin film device layer is never removed from the buried oxide (BOX) and handle layers. For flexible thin film electronics, the device layer is structured and patterned and a chemical etchant is used to undercut and remove the BOX layer. The now-freed silicon devices are placed on and adhered to a flexible final substrate material, including polyimide [70] or polyethylene terephthalate (PET) [71].

Alternatively, thin film semiconductors can be produced directly on a flexible substrate through growth or wet processing. Crystalline silicon requires high growth temperatures, well above the thermal range of most heat resistant polymers (400-450°C), and it is not solution-processable. Other semiconductor materials, including organics and amorphous or micro-crystalline silicon, however, can be fabricated in this manner. Micro-crystalline silicon, grown through plasma-enhanced chemical vapor deposition (PECVD) at 250°C has been successfully deposited directly on polyimide film to produce flexible strain sensors [72]. PECVD has also been used to deposit Indium-Gallium-Zinc-Oxide (IGZO) Thin Film Transistors (TFTs) arrays for flat screen displays directly on a thin polyimide substrate, which was then transferred to a transparent PET film [73]. In the solar cell industry, soluble organic semiconductors can be produced in roll-to-roll processing through knife blade application or slot-die casting [74]. The organic polymer

semiconductors are dissolved in organic solvents (methanol, toluene) or water, applied to the flexible substrate surface, and dried at low temperatures (70-140°C) [75].

2.7 Flexible Substrates

Flexible electronics can allow devices to fit a desired shape or conform to a surface, as well as shrink to fit smaller device package sizes. Normally, electronic devices are confined to thick, rigid bulk silicon substrates or to SOI with a rigid handle layer. To attain flexibility, the handle layer must be replaced with a physically flexible membrane. The material chosen for this membrane must be physically and chemically compatible with fabrication processes chosen to bond the semiconductor and provide electrical traces to external components. The metals used in a completed devices should bond permanently to the membrane surface, resist corrosion and degradation, and be robust enough to remain electrically connected after bending stress is applied.

Polyimides are frequently used in modern CMOS processes as interlayer dielectrics. Polyimides are chosen for their resistance to commonly used chemicals and their high operating temperatures (often up to 400°C). Film substrates may be spun cast or obtained as a roll of pre-cast film. After applying conductive metal to a polyimide film, it can be used as a flexible circuit or as a flexible host substrate for optoelectronic devices.

For light transmission, polyimide is a poor choice. Although it offers superior chemical and temperature resistance, polyimide is highly absorbent in the UV-blue wavelength regime. The absorption of 5mil thick Kapton polyimide over the optical spectrum is shown in Figure 18 [76].

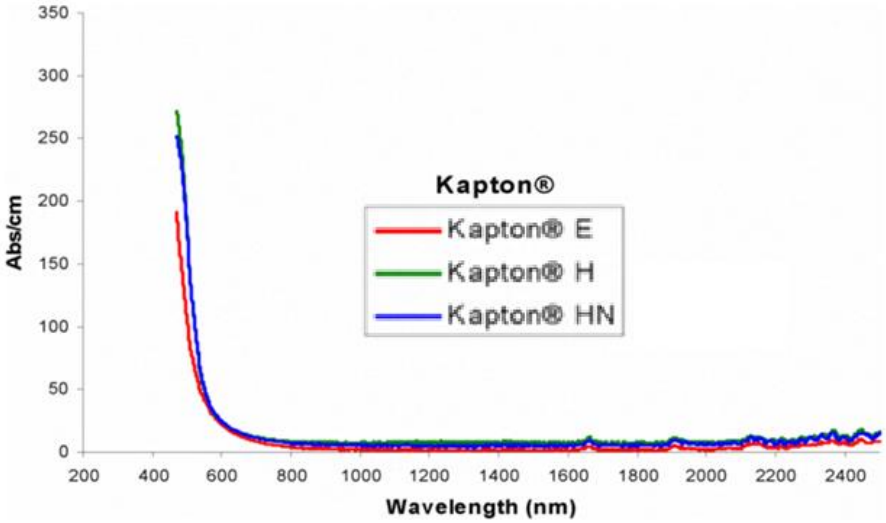

Figure 18. Kapton absorption spectra[76]

Fluoropolymers are also chemically and thermally resistant plastics. Certain formulations (PFA, FEP) are optically transparent in the visible wavelengths. The absorption spectra of selected fluoropolymers is shown in Figure 19 [76].

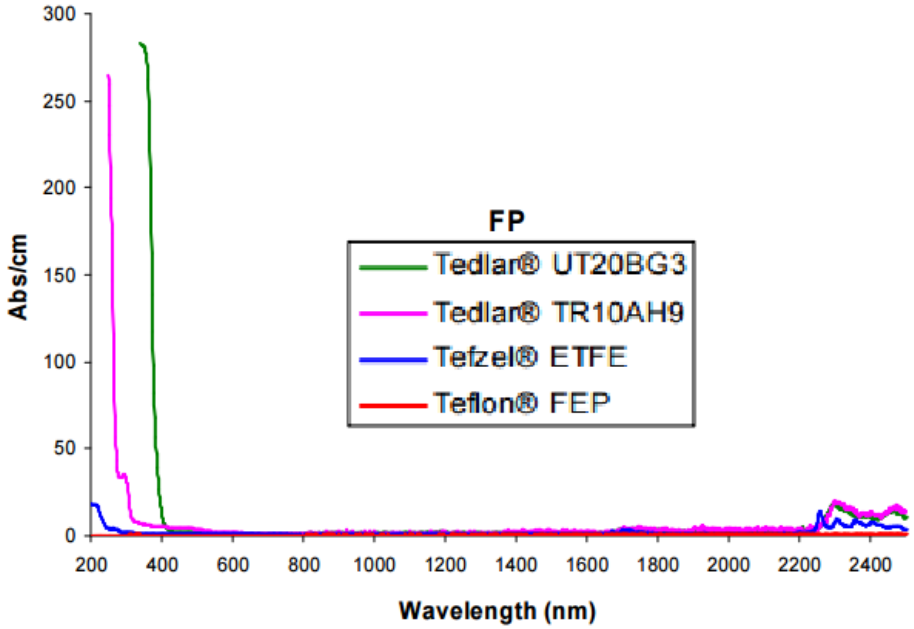

Figure 19. Fluoropolymer absorption spectra [76]

Fluoropolymers, such as DuPont's Teflon PTFE, exhibit high chemical and thermal resistance, but provide low bonding strength for attaching metals [77]. In general, additional effort is required to achieve a strong bond. Ion plating [78] or pre-sputtering with Argon [79] can improve the bond strength.

For transparent, flexible electronics, polyethylene terephthalate (PET) and polyethylene naphthalate (PEN) are widely used in research [80], [81] and commercial applications. PET and PEN are valued for their high optical transparency and high tensile strength. However, the glass transition temperature for PET (90°C) and PEN (130°C) [82] is much lower than that of Kapton polyimide (360°C-410°C) [83]. PET and PEN demonstrate lower optical absorption than polyimide, especially in the 400-600nm

wavelength range. The transmission spectra for multiple Mylar products, a PET film, is shown in Figure 20 [84].

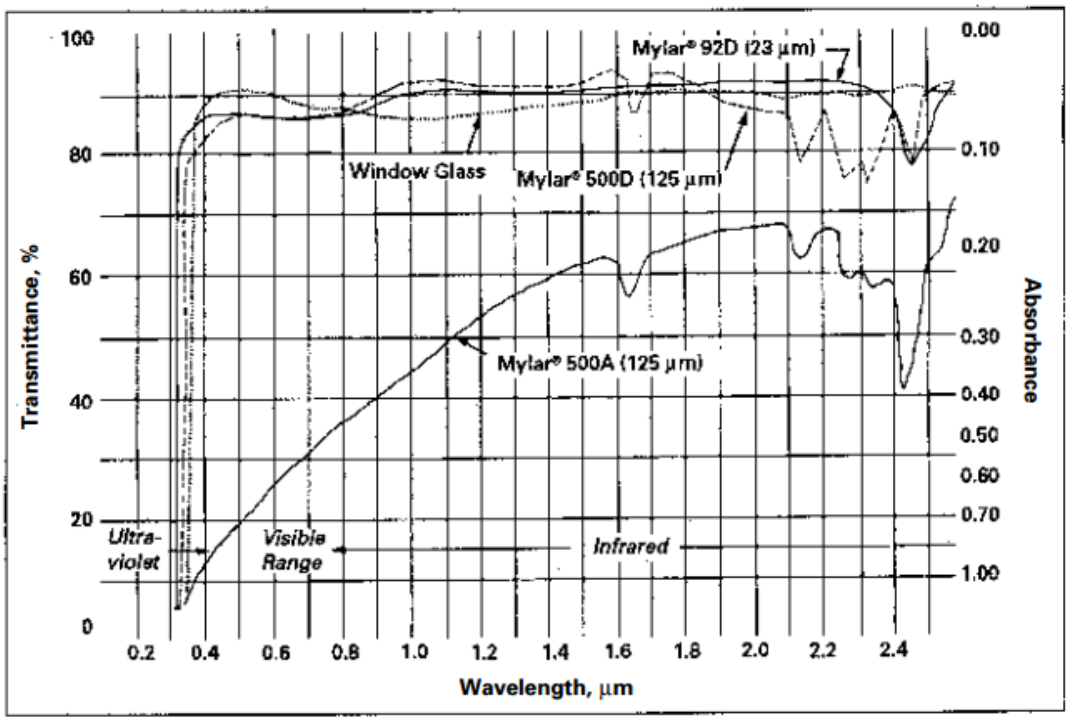

Figure 20. Mylar absorption spectra [84]

2.8 Flexible Metallization

Flexible substrates and flexible semiconductors alone are not sufficient in the production of flexible electronics. The conductive interconnections between semiconductor to semiconductor and semiconductor to an external circuit must also be flexible. Additionally, the action of flexure must not cause the electrical interconnections to fail. At high stress regions, particularly at material boundaries, stress-induced fracture can occur, causing breakage and open-circuit failure of the interconnects. In bonding

chromium-gold to polyimide film, 1μm thick metal bonds well to the flexible substrate, but the bonding is more likely to fail at high stress regions – such as the transition boundary between polyimide and silicon and near trapped air bubbles [85]. Adhesion of copper-polyimide can be accomplished by vacuum sputtering, but the copper layer can delaminate from the surface at elevated temperatures (~360°C) [86]. Titanium can similarly be sputtered, but will frequently mix with oxygen to form titanium oxides, preventing a strong bond and increasing electrical resistance. Sputtered or evaporated chromium has been found to be highly reactive with the polyimide surface, forming a strong bond. In addition to vacuum deposition techniques, electroplating copper on polyimide films creates a thicker, strongly bound metal-flex interface [87], [88]. Electroplated copper on top of sputtered chromium peel strength has been measured on Dupont Kapton polyimide up to 1kN/m. The interfacial strength can be improved by pretreating the polyimide with RF plasma before the chromium sputter [89] or increasing the metal thickness of a metallized flex system [90].

The patterning of the metal interconnects can improved to accommodate strain during flexure. A serpentine path allows for an overall reduction in the strain applied to the interconnect – strain is accommodated through rotation in the meandering path. As the meander height to spacing ratio increases, the stretchability (maximum strain before

failure) increases [91]. The relationship between meander height/spacing ratio and maximum strain is displayed in Figure 21.

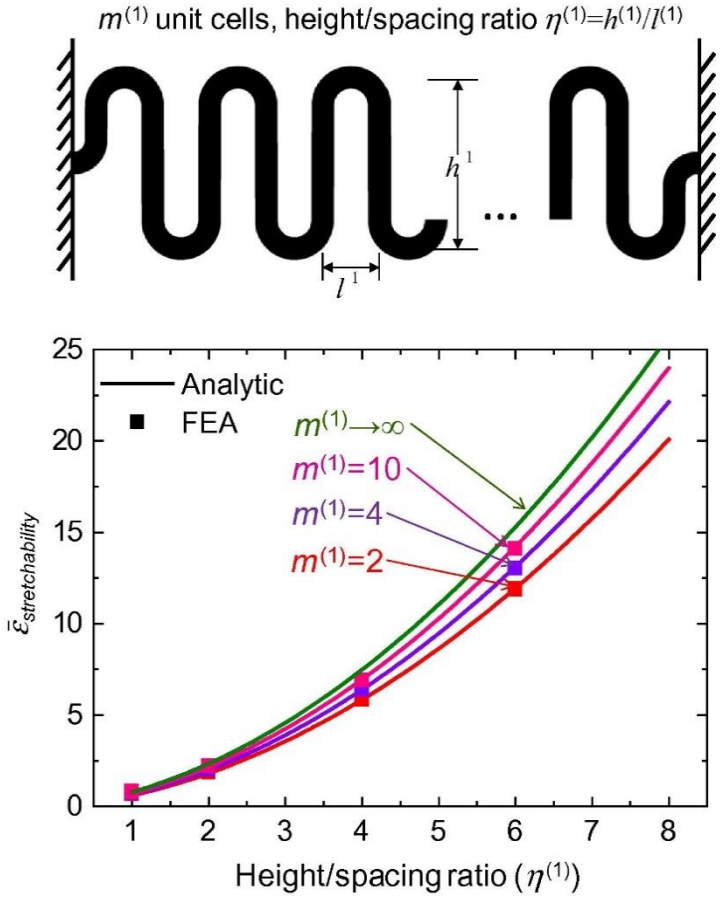

Figure 21. The increasing height/spacing ratio (η) accommodates a larger maximum strain (ε), for few to many unit cells (*m*) in a serpentine metal interconnect pattern [91].

2.9 Heterogeneous bonding

There are a variety of methods to integrate thin film semiconductors onto heterogeneous substrates. The integration method must result in a mechanically strong, reliable bond between the dissimilar materials.

Adhesive bonding employs an additional material between the semiconductor and substrate to create a permanent bond. Curable polymers are frequently used for the adhesive material, including benzocyclobutene (BCB) [92] or photocurable polymer (Norland NOA61) [60]. The polymer is first applied to the substrate by spin-coating. The semiconductor devices are softly imprinted into the polymer, and then the polymer is cured – resulting in a bonded substrate-adhesive-semiconductor system. Adhesive bonding can suffer from thermal expansion and strain mismatches, but the adhesive polymer alleviates the mismatch by distributing the strain over the material, instead of concentrating strain at single points. However, adhesive bonding does not provide a conductive electrical connection, unless conductive polymers, including poly(3,4-ethylenedioxythiophene) polystyrene sulfonate (PEDOT:PSS) [93], or conductive fill materials, such as metal particles [94], are used.

Thermocompression bonding occurs between metal surfaces when high pressure and temperature is applied. The bond is a weld between two separate surfaces when sufficient pressure is provided to create bonds at the atomic level, overcoming surface irregularities. As many thermocompression materials soften with temperature, elevated bonding temperatures reduce the required pressure to achieve a bond. Complete bonds were obtained in Au-Au lines on a 4" wafer with pressures of 7MPa at 300°C for 10 minutes [95]. Similarly, thermocompression bonding has also been demonstrated in

copper and aluminum. These metals require elevated temperatures as compared to gold, with copper bonding at temperatures up to 300-400°C [96] and aluminum at 400-500°C [97]. Increasing the temperature of the bonding process can lead to a more robust bond. Post-bond annealing can cause grain growth between the bonded surfaces, eliminating the visible bond interface and creating a stronger bond. TEM micrographs of grain-fused and interface bonds are depicted in Figure 22 [96].

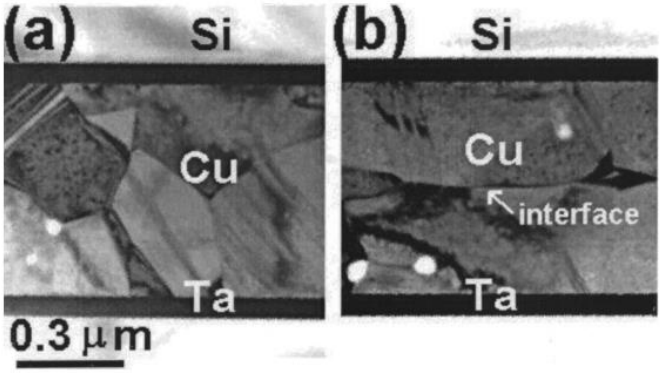

Figure 22 – TEM micrographs of (a) grain bond and (b) interface bond in Cu-Cu thermocompression bonding. Both bonds were performed at 350°C for 30mins, but the grain bond was subjected to additional N_2 annealing at 350°C for 60mins [96].

Failure analysis shows a marked decrease in bond failure in Cu-Cu bonding as bonding temperature is increased from 150-450°C. The failure rates are plotted against bonding temperature and annealing time in Figure 23 [96].

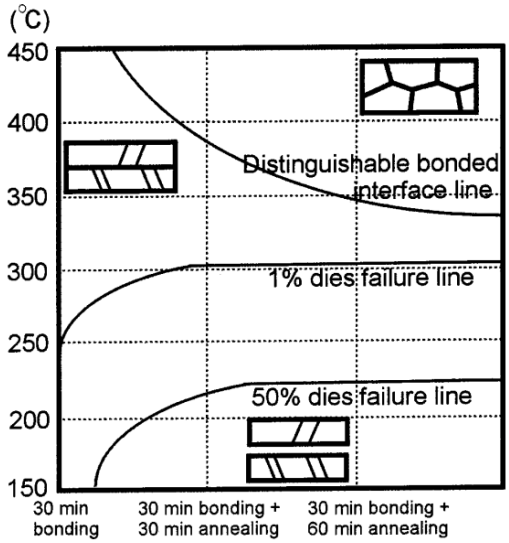

Figure 23 – Morphology and strength graph of Cu thermocompression bonding at a fixed pressure of 4000 mbar (400kPa) with variable temperature and annealing [96]

Copper bonding has also been demonstrated at lower temperatures (20-140°C), but with accordingly higher pressure (3.28Gpa compared to 400kPa at 300-400°C) to achieve a complete bond [98].

3. Design and fabrication of thin film flexible photodiode probe

This chapter discusses the design and fabrication process of the flexible photodiode probe. The design of the probe and the process used to realize this design are motivated by semiconductor device physics as well as the intended application of diffuse reflectance spectroscopy of breast tissue.

3.1 System Design

3.1.1 Photodiode Shape and Size

DRS probe detectors are typically circular in shape to maximize light collection since diffuse reflectance is radially symmetric, assuming that the media exhibits homogeneity in its optical properties. Thus, a circular photodiode surrounding the optical input beam collects the maximum reflected optical power. The detector probe demonstrated in this thesis consists of annular Si PN junction photodiodes. Each photodiode includes a center aperture, devoid of semiconductor material, for light transmission into the diffusely reflecting material under examination. The photodiode material surrounding that aperture absorbs the reflected light and outputs a photocurrent that is proportional to the absorbed light. The size of the detector is a design variable, since arbitrarily increasing the photodiode collection area does not

result in improved signal to noise ratio. In DRS, reflectance power decays exponentially with increasing distance from the optical source, as demonstrated in Figure 24 [99].

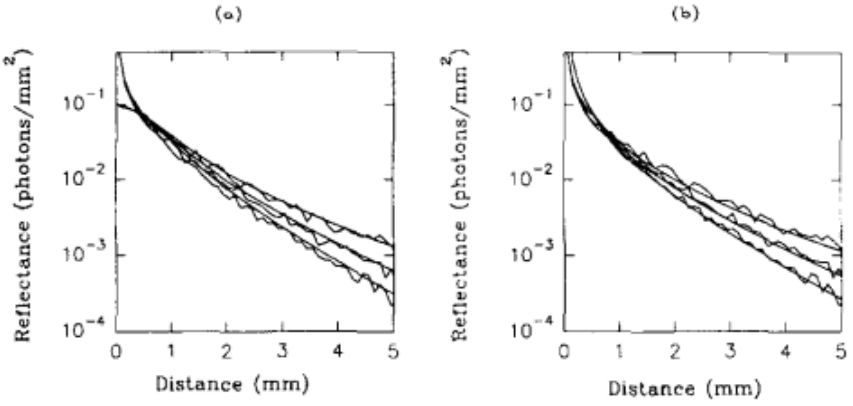

Figure 24. Reflectance power vs distance for (a) simplified single scattering event and (b) multiple scattering events, showing both diffusion approximation (smooth) and Monte-Carlo simulation (noisy) [99]

The collection gain achieved by increasing photodiode area is limited by this decay characteristic. The dark current also increases with increasing detector area, which limits the low level light collection and the signal to noise ratio (SNR). Additionally, an arbitrarily large area photodiode precludes high resolution imagery – as the detector size increases, the pixel-to-pixel spacing must increase accordingly. Therefore, there is an optimization compromise between high collection (large area), low light level detection, signal to noise ratio, and high resolution (high pixel density).

The crosstalk signal increases with increasing pixel density, as discussed in the previous chapter. As pixel-to-pixel spacing decreases, increasing diffusely reflected optical power from surrounding pixel apertures will illuminate neighboring pixels,

contributing to crosstalk noise in the DRS measurement. In optimizing the measurement SNR, it is essential to minimize the crosstalk signal.

For the research described herein, the photodiode diameter is 2.5 mm, and the pixel-to-pixel spacing is 4.5 mm. This size was chosen so that a comparison could be made between the research on reported DRS Si traditional (standard thickness Si) arrays of the same dimension that are in clinical testing at Duke to the flexible probe reported herein.

The photodetector outer diameter and pixel-to-pixel spacing were optimized using two major criteria: selecting a tissue interrogation depth and minimizing the crosstalk. The reflection and crosstalk is dependent on the tissue scattering and absorption properties, therefore the optimization is dependent on the expected tissue optical properties. For breast tissue, the expected sensing depth of a 2.5 mm outer diameter pixel is 1-2 mm [35], which agrees with recommended negative margin widths [5]. The 4.5 mm pixel-to-pixel spacing, when illuminated through an optimized light delivery system to minimize the angular distribution of incident light, results in crosstalk below 13% for simulated breast tissue [100].

The traditional Si detectors with these dimensions achieve a typical SNR of 40-50 dB when tested on breast tissue [101]. There is also a compromise in sizing the center aperture; a larger opening enables higher optical power to illuminate the tissue, but also

increases the crosstalk signal that reaches surrounding pixels. The selection of a 0.75 mm diameter center aperture was shown to limit worst-case crosstalk to 7-13% of the DRS signal in typical breast tissue [100].

The flexible Si probe was designed with two pixels, which is the minimum necessary pixel count for crosstalk analysis. A two pixel probe also enables rapid fabrication process development, as a lower pixel count achieves higher yield in the thermocompression bonding process described herein. The thermocompression process requires uniform pressure across all pixels; a smaller pixel count simplifies the challenge of uniformly distributing bonding pressure. The dimensions of the flexible two pixel probe are shown in Figure 25.

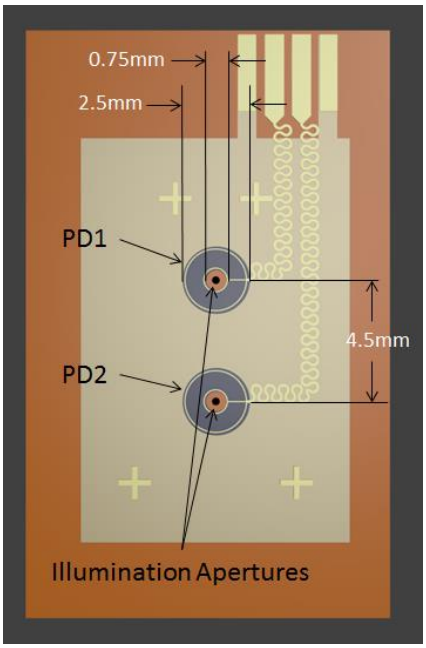

Figure 25. Dimensions of flexible photodiode probe used for this thesis work. The pixel-to-pixel spacing is 4.5mm, the photodiode outer diameter is 2.5 mm, and the photodiode inner diameter is 0.75 mm.

In DRS analysis of breast tissue, determination of the tissue type (e.g. adipose, fibro-glandular, or malignant carcinoma) is contingent on achieving high sensitivity to sources of optical contrast in the tissue. In breast tissue, the major absorbers are oxygenated hemoglobin, deoxygenated hemoglobin, and beta-carotene [102]. The absorption profiles of these chromophores are shown in Figure 26.

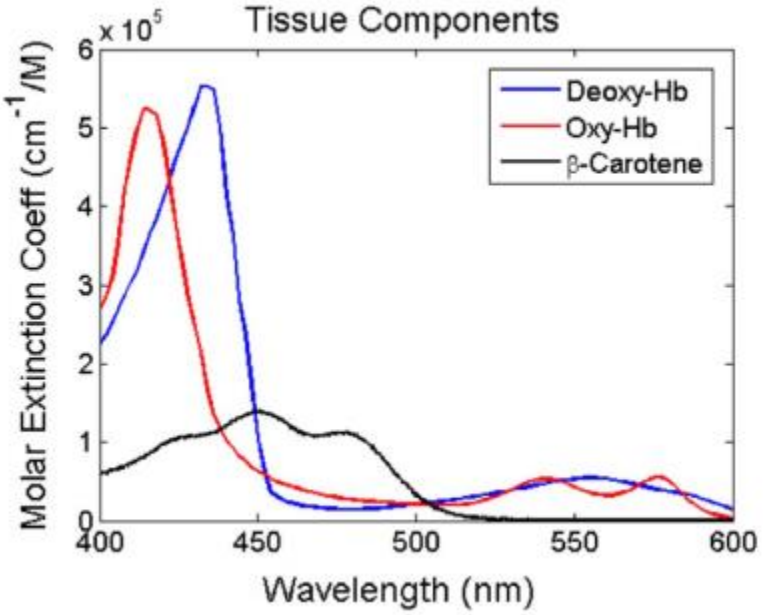

Figure 26. Absorption spectra of Deoxy-Hb, Oxy-Hb, and β-carotene in the wavelength range 400-600nm [102]

Attaining high optical contrast while reducing the DRS wavelength range enables a low-cost detection system – a few optical wavelengths can be generated from a set of LEDs or laser diodes, instead of requiring a wide-band light source and spectrophotometer as found in previous DRS systems [34]. Applying a genetic algorithm and inverse Monte Carlo feature extraction, Lo *et al* identified a group of eight distinct wavelengths – 470, 480, 490, 500, 510, 560, 580, and 600nm – that produced low extraction error of 12.6% for breast tissue [102]. Therefore, the photodetectors in the flexible DRS probe presented herein were optimized to produce the highest responsivity to optical power in the wavelength range 470-600nm.

3.1.2 Material Selection and Thickness

Silicon photodetectors have high responsivity in the visible optical spectrum, with previous silicon-based DRS probes by the Jokerst group achieving 0.18-0.38 A/W in the 470-600nm wavelength range in bulk silicon devices [35] and 0.19-0.34 A/W in thin film silicon bonded to Pyrex [62]. The responsivity is due to the high absorption of silicon in the visible optical regime, extremely low defect density in currently available single crystalline silicon wafers, and optimization of the PN junction depth for the wavelength range of interest.

The absorption coefficient of silicon is strongly dependent on the incident optical wavelength. High energy, short wavelength photons have a higher absorption coefficient in silicon than low energy, longer wavelength photons. The region of highest photon absorption is therefore closer to the surface for shorter wavelengths.

The junction depth in the flexible photodetectors is approximately 700-800nm, which maintains a high rate of photon absorption nearest the junction even for the shortest wavelengths in the 470-600nm range. Silvaco Atlas device simulation software was used to estimate responsivity for various junction depths, shown in Figure 27. Shallow junction depths improve the short wavelength responsivity, but result in decreasing responsivity at longer wavelengths. Deep junctions result in degraded short-wavelength responsivity.

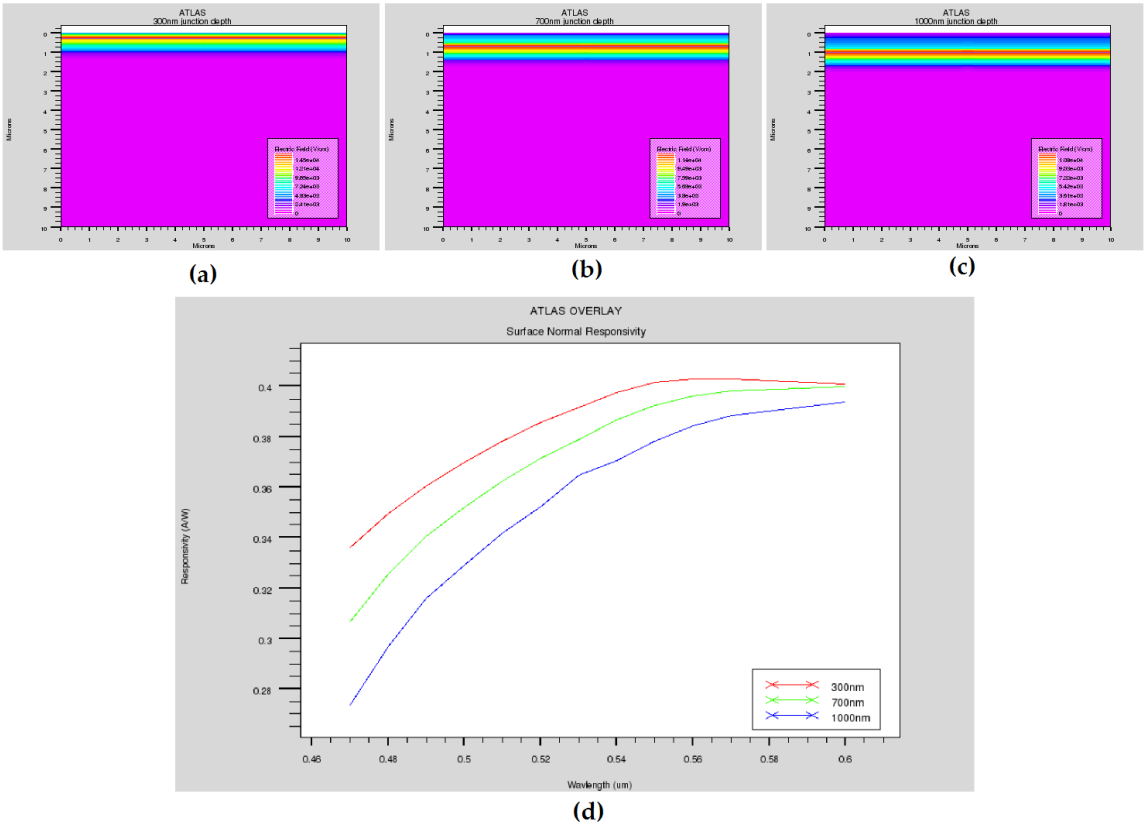

Figure 27. Silvaco Atlas 2D simulation displaying the electric field gradient of the photodiode for (a) 300nm; (b) 700nm; (c) 1000nm junction depths. (d) Simulated photo responsivity for 300nm, 700nm, and 1000nm junction depths.

Low optical absorption is detrimental to the photoresponse, especially in thin film detectors. It is crucial that the total thickness of the detector exceeds the depth for sufficient optical absorption into the semiconductor material. The total thickness of the thin film silicon PD is 10μm. Optical absorption in silicon follows the Beer-Lambert law:

$$I = I_0 e^{-\alpha l} \tag{3.1}$$

For the wavelength range 470-600nm, the optical intensity at a depth of 10 μm is calculated in Table 1. For the least absorptive wavelength for this research, 600 nm, over 98% of the incident light is absorbed in 10 μm of silicon. Additionally, the broad-area back contact serves as a back reflector. The contact metal stack of 100 nm Al / 50 nm Ti / 50 nm Ni / 200 nm Au is at minimum 91% reflective across the 470-600nm spectral range. The reflection from thin metal layers was simulated using OpenFilters software [103]. This metal layer aids in optical absorption by doubling the path length through silicon of reflected photons.

Table 1. Optical Absorption in 10μm Thick Silicon from 470-600nm

Wavelength (nm)	Absorption Coefficient, α (cm^{-1})	I/I_0 at 10μm
470	1.72×10^{4}	3.39×10^{-8}
500	1.11×10^{4}	1.51×10^{-5}
550	6.93×10^{3}	9.78×10^{-4}
600	4.14×10^{3}	0.0159

3.1.3 Anti-Reflection Coating

An anti-reflection coating (ARC) serves two purposes in the silicon photodetectors – reducing photon loss due to reflections and reducing the surface recombination velocity. SRV, discussed in the previous chapter, can reduce responsivity and increase dark current. A silicon nitride ARC also acts as a termination layer for the photodiode, reducing SRV. The nitride (n≈2.05) ARC is 60 nm thick, which results in a

minimum reflection at approximately 490 nm. The ARC thickness was chosen to optimize the shortest wavelengths in the desired range, since they exhibit the lowest spectral responsivity. A quarter-wavelength optical coating, or generally any odd number of quarter wavelengths, results in a 180° phase shift of reflected light from the substrate. Ideally, a quarter-wave ARC causes complete cancellation of reflected light [104]. A comparison of photogenerated current in a single-crystalline silicon PN junction photodiode (700nm junction depth, 10μm total thickness) with and without a 60 nm ARC was simulated in Silvaco Atlas, shown in Figure 28.

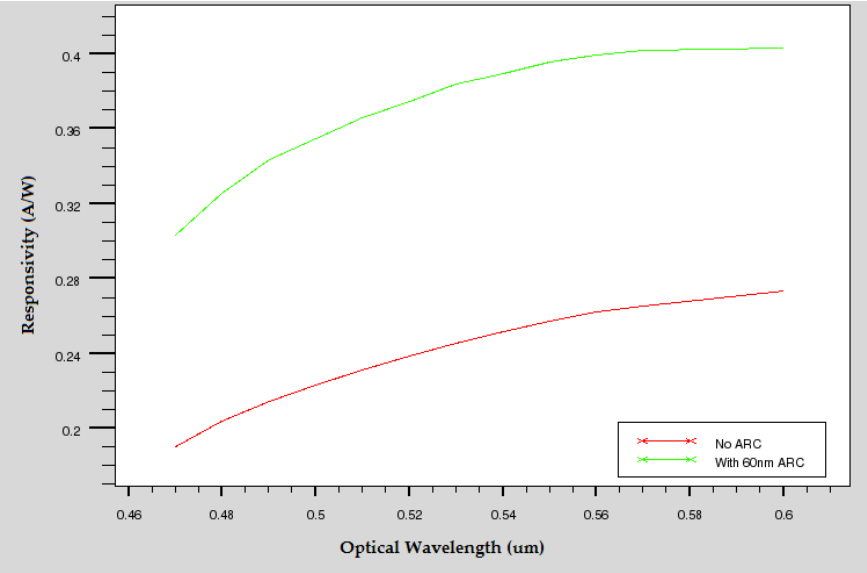

Figure 28. Simulated responsivity of a PN junction silicon photodiode with 700nm junction depth, with and without 60nm silicon nitride ARC.

3.1.4 Top Contacts and Leads

Metal top contacts on a photodetector provide an electrical path for photogenerated current to reach external leads and ultimately a current measuring device, such as a transimpedance amplifier. However, metal contacts are optically opaque, and increasing the contact width to decrease contact resistance comes with the price of reducing the optical absorption area of the detector. A double-ring contact design was chosen for the flexible photodiode probe, with the metal rings approaching the edges of the silicon active area. The contacts are located at the innermost and outermost radii of the photodetector to improve photocurrent extraction. The worst-case extraction, where the distance between the point of photogeneration and extraction at the metal contacts is the highest, occurs at the mid-point between the two contacts. While a single ring contact placed at the mid-point radius results in the same worst-case generation-to-extraction distance (assuming uniform illumination), the double-ring design was chosen to improve photocurrent extraction closest to the inner radius. In diffuse reflectance spectroscopy, the optical intensity decreases as a function of radial distance from the optical source (the central aperture), especially for highly absorbing tissue and at shorter wavelengths. The inner radius contact is located nearest the region of highest optical intensity. The outer radius contact was included to decrease the generation-to-extraction distance for diffuse reflection of lower absorbing tissue and at

longer optical wavelengths, which result in higher reflected optical power further from the central aperture. The contact width is 40 μm. The contact thickness is a compromise between decreasing the contact resistance and increasing the non-shadowed detector area. The contact width as designed results in a low resistance per unit length of approximately 2.0 Ω/mm. The inner ring has a radius 40 μm larger than the 375 μm radius central aperture. The 40 μm gap between the silicon edge and top lead allows for increased absorption of diffusely reflected light closest to the optical aperture, and provides misalignment tolerance for photolithography. The outer ring radius is 90 μm less than the silicon 1250 μm radius. The 90 μm gap permits a region to overlap the interlayer dielectric onto the silicon surface. These dimensions are shown in Figure 29.

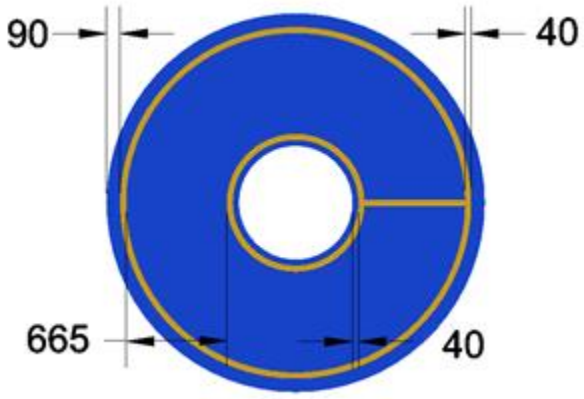

Figure 29. Top contact design for the flexible photodiode. All dimensions are microns.

The total area covered by this double ring design is 0.422 mm^2, which optically occludes approximately 9.5% of the 4.47 mm^2 annular photodiode.

As shown previously in Figure 25, the external electrical leads for the flexible photodetector probe follow a serpentine path from the silicon detector area to the electrical contact pads. The previous chapter discussed the advantages of serpentine leads, including their resistance to damage from strain. The shape chosen for the leads is a horseshoe pattern, created through a repeated pattern of circular arcs. An example of this serpentine pattern is shown in Figure 30.

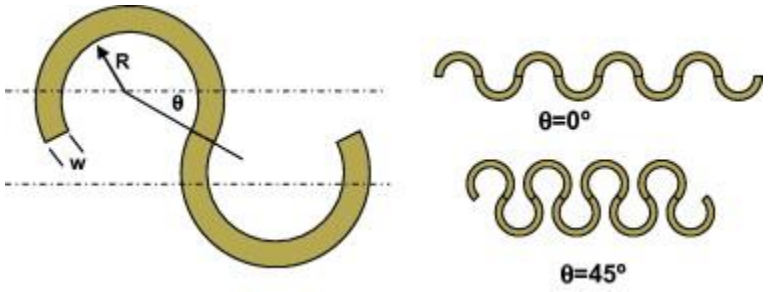

Figure 30. Horseshoe lead pattern. Design parameters are: R = arc radius, W = lead width, and θ = joining angle [105]

Increasing the ratio of arc width to radius leads to a reduction of induced strain during elongation [105]. However, the resistance of the horseshoe interconnect increases as this ratio is increased, since the length-to-area ratio would also increase. The horseshoe design employed in the flexible photodiodes has θ=45°, W=100 μm, and R=126.8 μm. The external leads are located nearest PD1, which ensures that the leads remain flat when the photodiode probe is flexed cylindrically. Since the external contacts are located closest to PD1, the longer leads for PD2 result in a higher resistance. The 100 μm width was used in this design to lower the resistance between the photodiode and

the external contacts. The resistance per unit length for these leads, including the increased length due to the serpentine meander, is approximately 1.34 Ω/mm. The 126.8 μm horseshoe radius was selected so that the unit cell length (two horseshoe "hoops," tip to tip) would be 500 μm. This radius selection simplifies the CAD process of designing the photolithography mask, since each "hoop" can be offset by multiples of 500 μm while maintaining an electrical connection.

3.1.5 Inter-Layer Dielectric

An interlayer dielectric layer must be used to isolate the bottom contact from the top contact on the PD. The interlayer dielectric (ILD) material chosen for the flexible photodiode probe was a spin-coatable polyimide (DuPont PI-2525). This polymer dielectric layer was chosen because it is flexible, and can be spin-coated onto the sample. Typical ILD materials for rigid devices often utilize inorganic materials, such as silicon dioxide, however, these are rigid materials, and would crack in a flexible application. Polyimide also has good strength during flexure. The tensile strength and Young's modulus of PI-2525 are 128.5 MPa and 2.402 Gpa, respectively [106]. The ultimate strain is therefore .053, or 5.3%. In contrast, silicon dioxide has a higher modulus of 60 Gpa, but only a moderately higher tensile strength of 364 Mpa [107], resulting in an ultimate strain of 1.2-2.4%. With a higher ultimate strain, polyimide is less likely to crack during flexure than SiO_2.

3.1.6 Flexible Substrate Selection

The flexible substrate chosen for the photodiode probe was Kapton HN polyimide. Although polyimides are not transparent throughout the 470-600nm optical range, this material exhibits very high heat resistance and chemical resistance, which is important for the post-processing that is required to integrate the thin film Si PD onto the flexible host substrate. The Kapton HN operating temperature ranges from -269°C to 400°C [83]. In the experiments for this thesis, Kapton HN film was not adversely affected by common clean room chemicals, including acetone, isopropanol, hydrofluoric acid, and trichloroethylene.

Since Kapton is partially opaque in the visible spectrum (see Chapter 2), a computer-controlled CO_2 laser was used in this thesis research to ablate a circular opening in the center of each photodiode. Polyimide is a thermosetting polymer, meaning that it does not return to a soft or viscous state after curing. The laser ablation process removes polymer material without the surrounding material deforming through heating. However, it was important not to laser ablate the metal or the Si in the PD. Due to this risk of damage to the photodiodes or the metal, the laser ablated aperture diameter was design to be approximately 200 μm, which is smaller than the 750 μm inner diameter of the photodiode.

3.1.7 Bonding Method

The thin film silicon photodidoes were integrated with the flexible polymer substrate using thermocompression bonding. The vertical PN junction design includes a broad-area metal contact on the bottom of the thin film silicon photodetector. This necessitates an electrical connection at the bonding interface in order to access the anode. Thermocompression bonding provides an electrical connection at the metal-metal bond interface. Since the bond interface covers a wide area in thermocompression bonding, there is a lower likelihood of bond failure after repeated flexures.

3.1.8 Flexible Substrate Planarization

Flat, clean surfaces are essential for strong, conductive thermocompression metal to metal bonds. Previous work in thermocompression bonding by the Jokerst group was on rigid, polished Pyrex wafer substrates [62], or on Kapton polyimide with no further processing (e.g. top contact) after bonding [108]. The Kapton film surface was measured in a profilometer, and the root-mean-square surface roughness was approximately 63 nm. In contrast, the surface roughness of polished Pyrex is less than 1nm [109]. Thus, the surface roughness of the as-procured Kapton may impede a complete thermocompression bond. Rough surface conditions can lead to bond failure. Using the same spin-coatable polyimide as for the inter-layer dielectric (PI-2525), a pre-bonding planarization layer was applied. This polyimide layer decreased the root-mean-square

surface roughness of the Kapton by a factor of three, to approximately 22 nm. A profilometer (Bruker Dektak 150) comparison of the untreated and polyimide-planarized Kapton is shown in Figure 31.

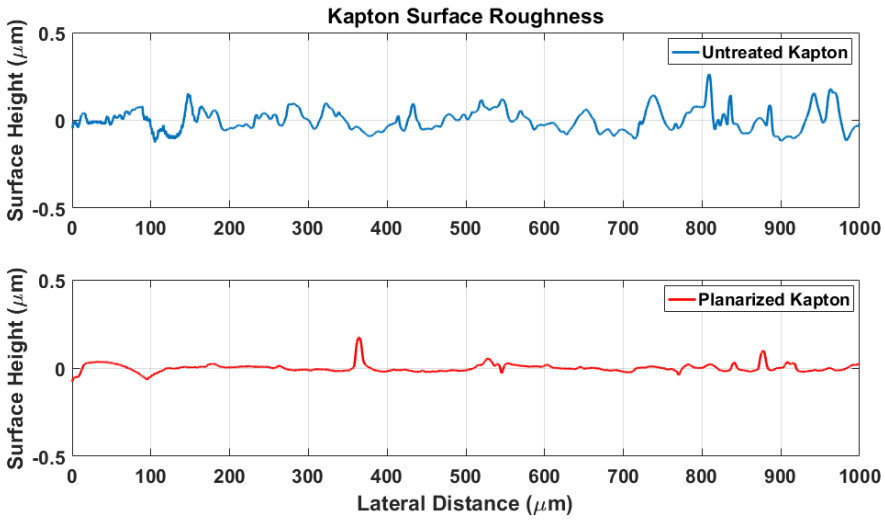

Figure 31. Surface profilometer measurements of untreated (top) and planarized (bottom) Kapton film.

3.2 Fabrication

The thin film photodetector probes fabricated by the Jokerst group have previously been mostly bonded to rigid Pyrex substrates [62], with one published exception [108]. The fabrication process is similar for both rigid and flexible probes. The following section discusses the flexible fabrication process, which has been utilized in this thesis research toward functional, flexible DRS detector probes. The process flow is illustrated in Figure 32.

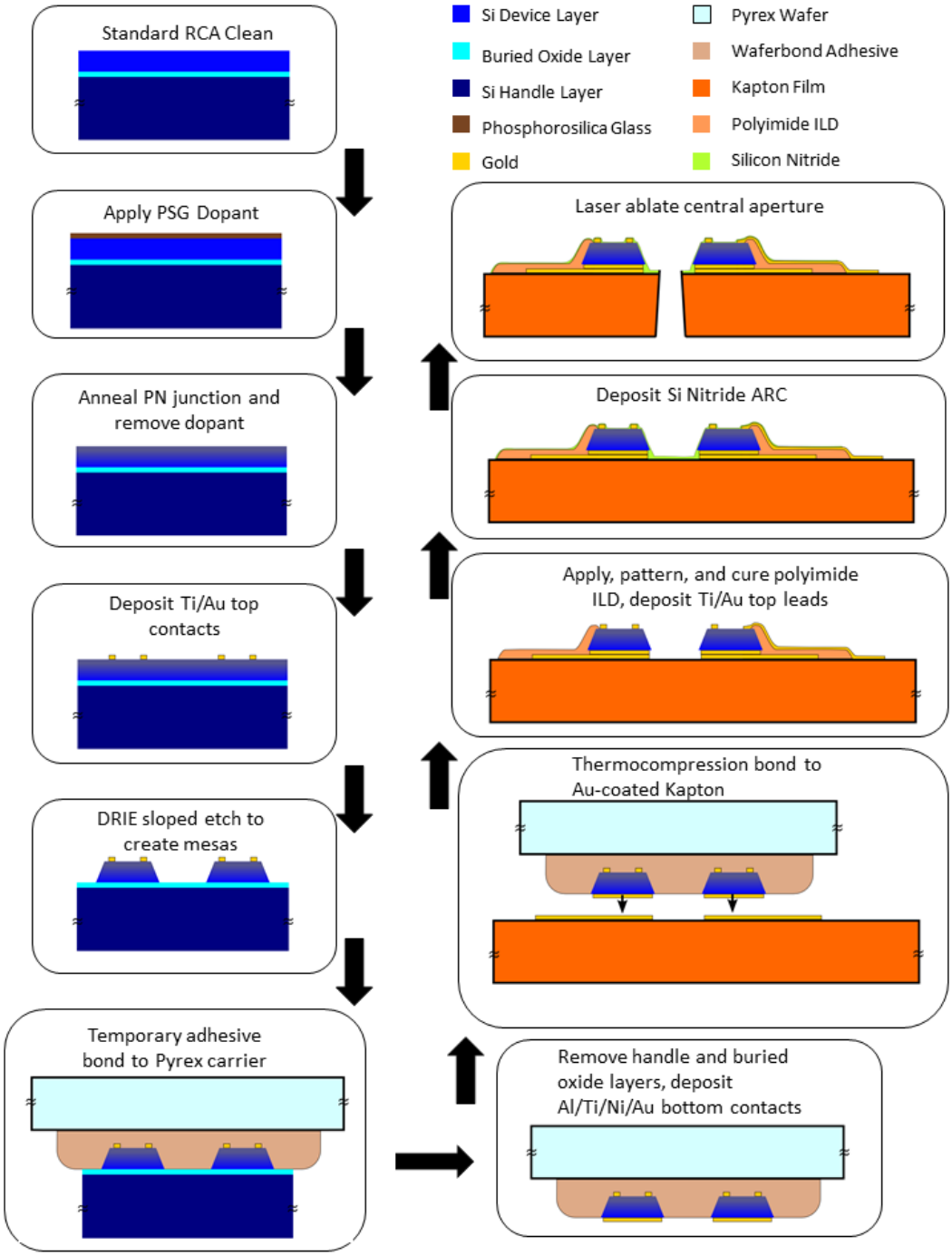

Figure 32. Fabrication process flow of thin film 2x1 annular Silicon PN-junction PDs on a flexible polymer substrate

Thin film single crystal Si photodetectors were fabricated from commercial purchased SOI silicon wafers (Addison Engineering), which had 10 μm thick p-Si (device layer, Boron, 30-60 Ohm-cm) / 1μm thick silicion dioxide / 400 μm thick p-Si (handle layer, Boron, 30-60 Ohm-cm). After cleaning with the RCA process, the top of the device layer was coated with spin on n-dopant (Phosphorofilm, Emulsitone Chemicals) and annealed in a diffusion furnace at 1000°C for 15 minutes. The spin-on dopant was etched with diluted HF and Piranha solution (H_2SO_4:H_2O_2, 3:1), and top contacts were defined using negative photoresist (NFR 016-D2, JSR Micro), followed by e-beam evaporation of a titanium (1000 Å)/ gold (2000 Å) metal stack with subsequent liftoff by immersion in acetone. Then, the photodetector active areas were defined by mesa etching, leaving behind isolated silicon device mesas on the oxide layer. The mesa etch was performed using a deep reactive ion etch (DRIE) system (SPTS Pegasus). The electrical leads that connect the mesa top contacts to the wirebond pads need to traverse this etched sidewall, therefore a vertical sidewall is not desired for these mesas. By designing an angled sidewall, the electrical connection can be enabled. The etch process recipe is customized to achieve 45-55° sidewalls. An scanning electron microscope (SEM) micrograph of a cleaved sample etched with the sloped sidewall DRIE recipe, demonstrating a 46° sidewall, is shown in Figure 33 [100]. A photograph of etched mesas on SOI with top contacts are shown in Figure 34.

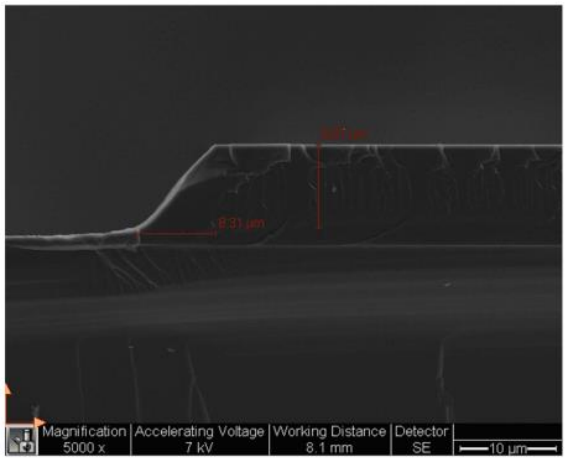

Figure 33. Cleaved SOI sample demonstrating 46° sidewall after DRIE sloped etch process [100].

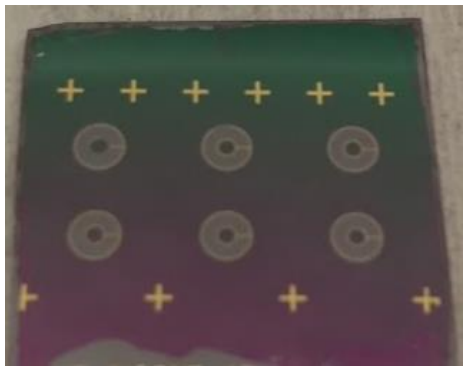

Figure 34. Thin film silicon mesas on SOI with double-ring gold top contacts.

After the mesa etch, the SOI wafer was bonded to a 500µm thick Pyrex carrier wafer using a temporary wafer adhesive (Waferbond HT10.10, Brewer Science). The device layer side of the SOI wafer was placed in contact with the Pyrex, leaving the bulk silicon side exposed. The bonding process was performed in a vacuum oven at 180°C to release trapped air from the Waferbond. A custom machined steel bonding jig was used to apply pressure directly to the silicon and Pyrex. Once the bonding process was

complete, the exposed 400 μm silicon handle layer was removed using DRIE, with a process recipe customized for bulk silicon removal. The 1 μm thick buried oxide served as an etch stop layer. The buried oxide layer was then removed with a hydrofluoric-based wet etch, which exposed the silicon back side of the thin film detectors. Next, back contacts of aluminum (2000 Å)/titanium (500 Å)/nickel (500 Å)/gold (2000 Å) were deposited and patterned onto the exposed silicon by negative lithography, electron-beam evaporation, and liftoff in acetone. The back contact pattern was broad area, covering the entire back of the mesa.

The final carrier substrate for the thin film PDs was a polyimide film of Kapton® (HN 5 mil, McMaster-Carr). The Kapton film was cleaned under sonication in acetone, then rinsed in isopropanol. Next, the Kapton film was planarized by spin-coating a 5 μm thick layer of polyimide PI-2525. The polyimide-coated Kapton substrate was then cured in a nitrogen environment at 300°C for three hours. A negative photoresist pattern for the substrate metallization was then spin-coated, exposed, and developed. Next, a metal stack of Cr (50 Å) / Au (2000 Å) was deposited by electron-beam evaporation, followed by liftoff in acetone. A flexible substrate prepared following the process outlined above is shown in Figure 35.

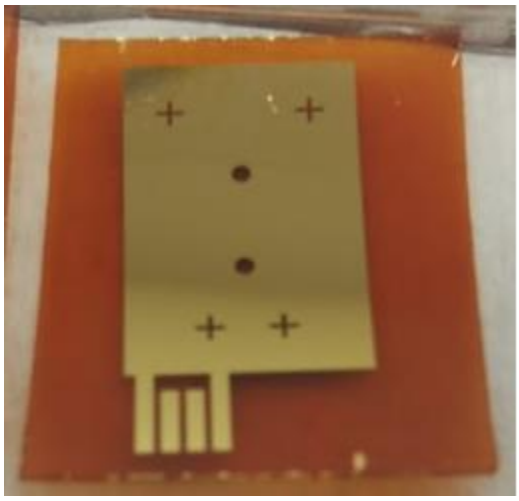

Figure 35. Planarized and metallized Kapton polyimide substrate.

The two thin film photodetectors were bonded to the Kapton substrate simultaneously using a gold-gold thermocompression bond. The exposed gold on the back of the photodetectors and on the top of the Kapton was cleaned with acetone and isopropanol, followed by an oxygen plasma ashing (Emitech K-1050X). The detectors and Kapton substrate were placed in contact under a microscope, and transferred to a hot plate set to 210°C. Force was applied using the same bonding jig as in the temporary wafer bonding step. This heated pre-bonding was conducted with no additional weight for 10 minutes, followed by 20 minutes with a 1 kg weight. After the pre-bond on the hot plate, the bonding jig with the photodetector probe was transferred to a vacuum oven. Two 1 kg weights were added to the top of the bonding jig to apply additional bonding pressure. The oven temperature was ramped to 275°C at 2°C/minute, and held at that

temperature for 15 minutes. The temperature was ramped back to 100°C at 1°C/minute before the probe was removed from the oven and bonding jig.

The temporary Pyrex wafer was removed from the bonded Kapton-silicon assembly by heating it on a hotplate at 250°C to melt the Waferbond. The Pyrex wafer was then removed by gently sliding it off with tweezers. The remaining Waferbond was removed by immersion in trichloroethylene followed by oxygen plasma ashing. A bonded pair of photodetectors is shown in Figure 36.

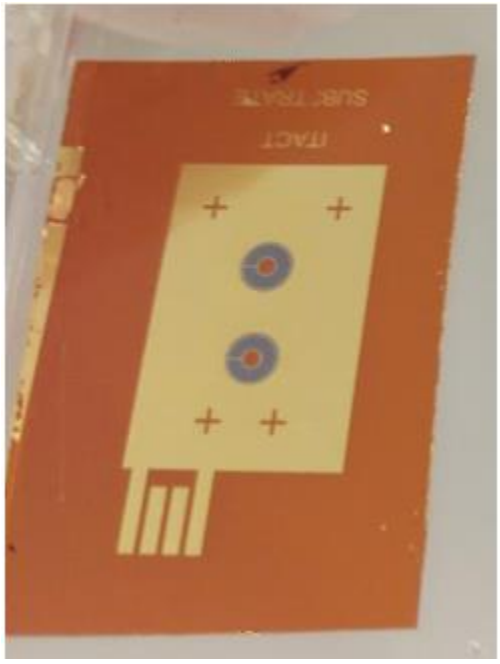

Figure 36. Thermocompressively bonded Thin film silicon mesas on a flexible Gold-coated Kapton substrate.

Following bonding, a 5μm thick layer of PI-2525 polyimide was spin-coated on to the sample for the ILD. The polyimide was then soft-baked in an oven at 120°C for 2

minutes, which evaporates the solvent (*n*-methyl-2-pyrrolidone) but does not cause the polyamic acid precursor to fully imidize [110]. The ILD was patterned using positive photoresist (Microposit S1813) followed by UV-exposure. Immersion in a TMAH-based developer caused the pattern to develop in both the photoresist and the uncured polyimide film. The photoresist was then removed with acetone and isopropanol. The polyimide ILD was cured in a nitrogen environment at 250°C for four hours.

Serpentine electrical leads connecting the top metal contact (cathode) on the silicon to the contact pads on the Kapton substrate were fabricated using negative lithography, electron-beam evaporation, and liftoff in acetone. The silicon nitride ARC was deposited by plasma-enhanced chemical vapor deposition (PECVD, Advanced Vacuum Vision 310). A glass coverslip was positioned on top of the electrical pads on the structure to prevent them from being covered with the electrically-insulating nitride film. A false-color image (for visibility) of the photodiode after ARC is shown in Figure 37.

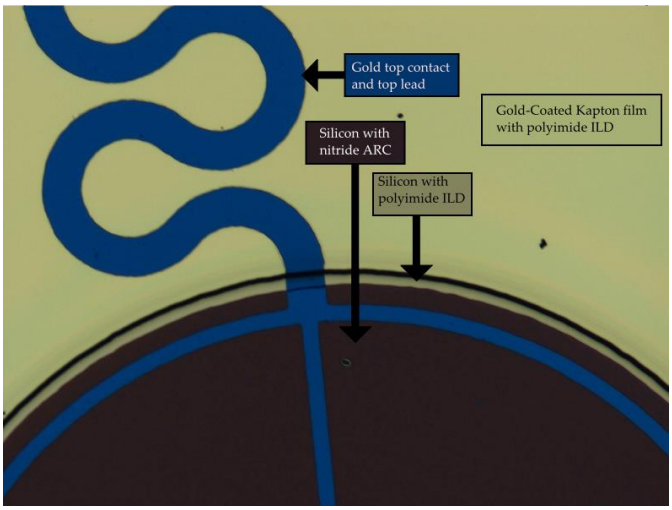

Figure 37. False color image of thin film photodiode on Kapton, showing metal contacts (blue), silicon (dark gray), and gold-coated Kapton under polyimide ILD (olive).

The Kapton material in the center of both photodiodes was ablated using a computer controlled CO_2 laser (Full Spectrum Laser H-Series). The photodetector-side of the Kapton film was protected with a thick application of photoresist to protect the silicon. After ablation, the photoresist was removed in acetone and isopropanol, and any remaining ablation residue was cleaned with light oxygen plasma etching. A laser-ablated aperture in Kapton with a bonded, undamaged silicon detector is shown in Figure 38. Unremoved residue is visible on the silicon near the ablated aperture.

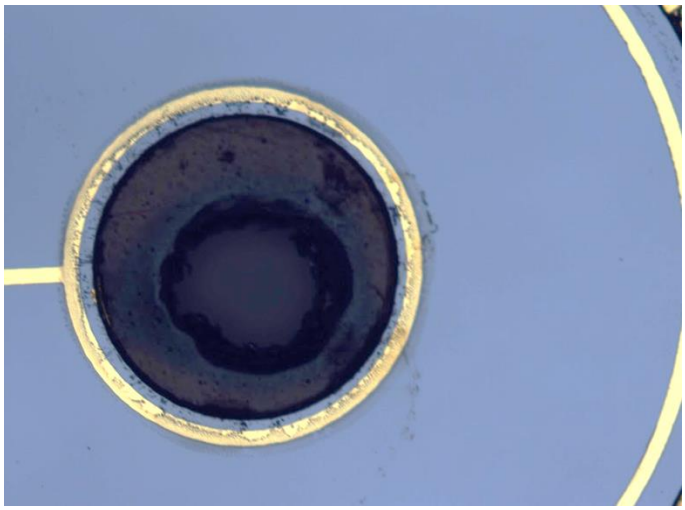

Figure 38. Laser-ablated aperture in Kapton with thermocompressively bonded thin film silicon photodiode.

The finished photodiode probe is shown in Figure 39. The device is shown affixed to a glass slide in Figure 39(a), which provides a flat, rigid surface. This technique of taping the flexible probe to a flat surface was used for all spin-coating and lithographic processing on the flexible Kapton substrate.

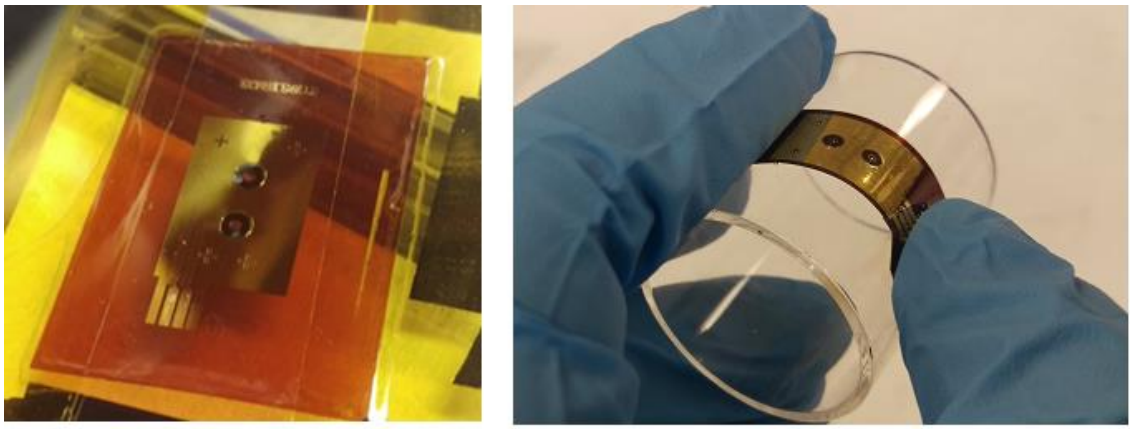

Figure 39. (a) Image of flexible thin film silicon photodiode probe shown taped to a glass slide; (b) Image of flexible probe bent cylindrically with a radius of 15 mm.

This chapter has presented the design and fabrication process of the thin film silicon photodetector DRS probe. The design of the probe, including the material selection, photodiode size and pixel-to-pixel spacing, and electrical contact and lead design were influenced by the constraints of semiconductor physics and diffuse reflectance optics.

4. Photodiode Testing and Diffuse Reflectance Phantom Measurements

This chapter discusses characterization tests for the flexible photodetectors and diffuse reflectance measurements on tissue mimicking phantoms. All dark current and responsivity tests and phantom tests are reported for both flat and flexed conditions.

4.1 Characterization Testing

To characterize the thin film PDs bonded to the Kapton flexible substrate, dark current and responsivity measurements were performed using a Keithley 4200 source measurement unit (SMU) and a Newport 300W Xenon lamp with a Newport CS130 monochromator. The light source was coupled to a 1 mm diameter optical fiber with NA of 0.39, and the output of the fiber was focused through a microscope objective lens to provide surface normal illumination on the photodiode. The optical wavelengths measured were in the range of 470 nm to 600 nm, in increments of 10 nm. The optical power was measured separately using a Thorlabs PM-100 power meter. The typical illumination power at the output of the microscope objective was 140-180 nW for the spectral range 470-600 nm. For the photodiode probe tested, PD1 had higher responsivity and lower dark current than PD2. The responsivity for both PDs is shown in Fig. 4. The measured responsivity for PD1 at zero bias was 0.20-0.34 A/W for λ = 470-600nm. For PD2, the measured responsivity was 0.10 to 0.17 A/W for the same

wavelength range. The responsivity as a function of wavelength is shown in Figure 40. The zero bias dark current averaged 9 pA for PD1, and 370 pA for PD2. With a total photodiode surface area of 0.0447 cm^2, the dark current density for PD1 was 0.201 nA/cm^2 and 8.28 nA/cm^2 for PD2.

The responsivity of PD1 is comparable to previous bulk Si PDs (0.22 – 0.30 A/W), while its dark current density is lower (1.456 – 4.48 nA/cm^2) [15]. PD1 is also comparable in performance to previous thin film Si PDs on rigid Pyrex (0.19 – 0.34 A/W and 0.63 nA/cm^2) [108].

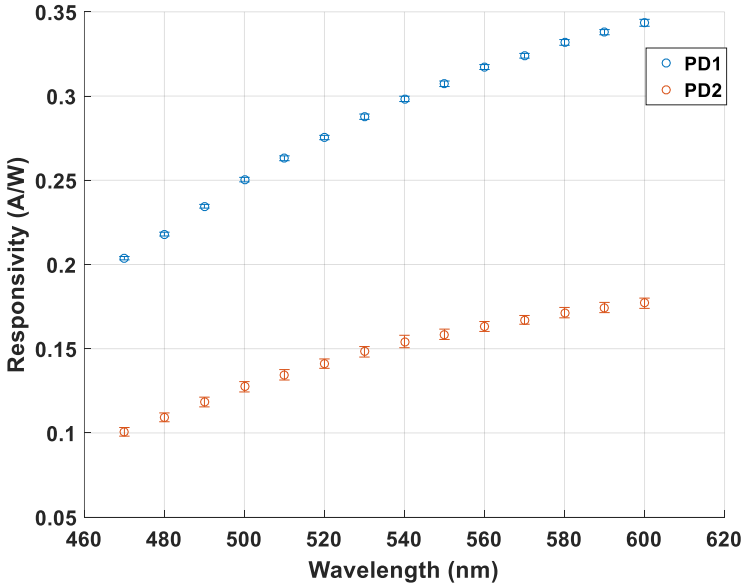

Figure 40. Surface normal responsivity for the photodiode probe as a function of incident wavelength for the range 470 nm-600 nm.

The IV characteristics for PD1 and PD2 are shown in Figure 41. The dark IV curve for the two PDs shows weak diode behavior for PD2. This could be the result of

the contact metal spiking through the junction in small areas of the contact, resulting in a mixture of photoconductor and PN junction behavior.

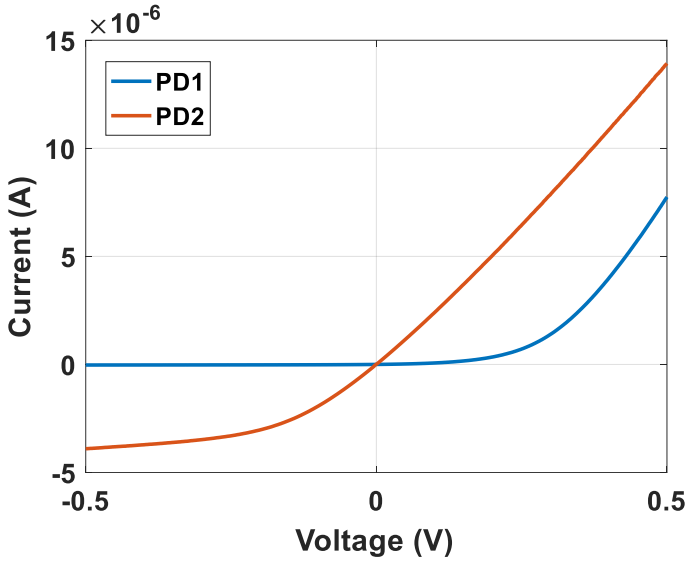

Figure 41. Dark IV for PD1 and PD2, demonstrating a weak diode behavior for PD2.

4.1.1 Characterization of the PDs during flexure

Surface normal responsivity measurements were conducted on PD1 during flexure. Due to the lower responsivity and higher dark current of PD2, PD1 was the focus of subsequent testing, since the performance of PD1 was comparable to that of reported rigid PDs [62]. The responsivity was measured using the electrical and optical test setups described in the previous section. The flexible assembly was held by a series of 3D printed plastic clamps that flexed PD1 to five distinct radii of curvature. Illumination was again provided through a microscope objective focused on the PD surface. The focal spot was positioned at the bottom of the cylindrical bend to ensure

surface normal illumination. At each wavelength and curvature, 50 measurements of photocurrent were averaged. The SNR for these measurements, calculated using $20 \times log(I_{photo}/\sigma_{Iphoto})$, was 45.8 dB. The average variation of responsivity due to curvature for bends measured up to a 10 mm radius of curvature was 0.61%. The results of this testing are shown in Figure 42.

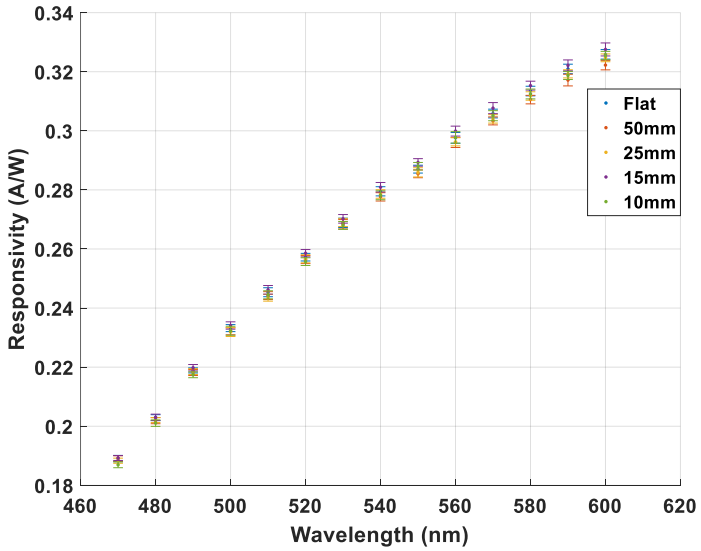

Figure 42. Responsivity during flexure for PD1 for five radii of curvature.

Dark current I-V characteristics were also taken for each of the five curvatures, flat (infinite radius), 50 mm, 25 mm, 15 mm, and 10 mm, for the voltage range -0.5V to +0.5V. The I-V measurements are shown in Figure 43. Additionally, the zero-bias dark current was characterized at each curvature with 100 consecutive current measurements. The zero bias dark current varied from 9-12 pA for all five curvatures.

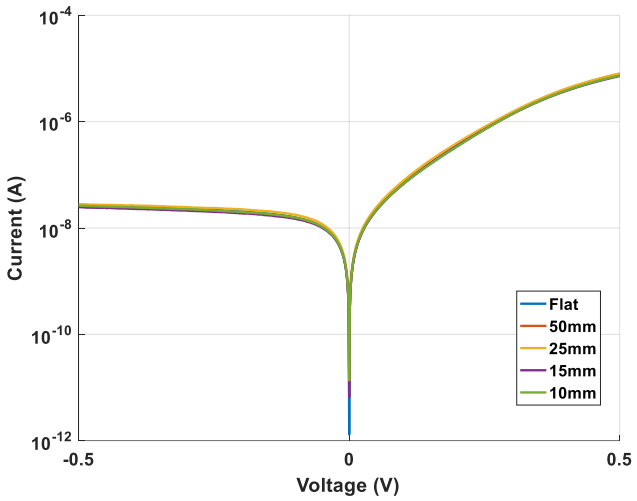

Figure 43. Dark current characterization of PD1 at multiple bend radii.

The flexible thin film Si photodiode PD1 demonstrates comparable dark current and responsivity characteristics to previously reported bulk Si PD arrays. Additionally, the dark current and responsivity demonstrate little change due to flexing up to a radius of 10 mm, with approximately 0.61% change in responsivity and a 3 pA variation in dark current.

4.2 Liquid Phantom Test Design

To perform diffuse reflectance measurement while flexing at various curvatures, pairs of plastic clamps were 3D printed with five discrete radii of curvature: flat (infinite radius), 50 mm, 25 mm, 15 mm, and 10 mm. The upper section of each pair of 3D printed parts included a hollow volume for containing a liquid phantom during testing. The inner walls of this hollow volume were painted black to minimize sidewall reflections.

The open bottom end of the phantom container was capped with a 50 μm thick PET film (McMaster-Carr). The PD/Kapton probe was placed below the PET with the detectors facing upwards, towards the phantom. The two detectors were aligned equidistant from the center of the bottom face of the phantom. This experimental setup is illustrated in Figure 44.

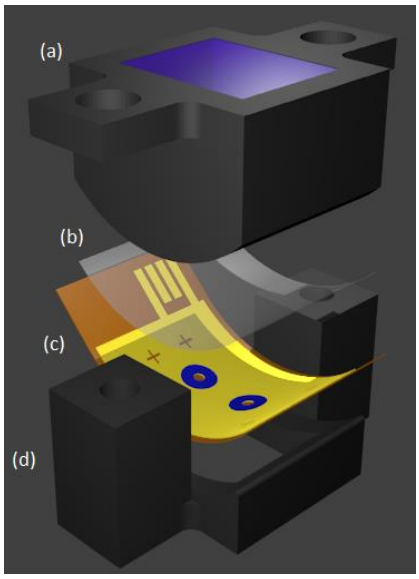

Figure 44. Illustration of liquid phantom testing at 10 mm radius of curvature: (a) Upper plastic 3D printed clamp, with curved bottom edges and hollow region to contain liquid phantom; (b) Transparent PET film; (c) Flexible PDs on Kapton; (d) Bottom clamp, with curvature matching the top clamp.

The optical source was a 300W Xenon lamp (Newport TLS-300XU) and monochromator (Newport CS130 1/8m) for all phantom measurements. Illumination was provided through a 1 mm diameter optical fiber (NA=0.39) aligned to the center aperture of one of the two photodiodes. Since PD1 was a more sensitive PD,

measurements focused on PD1. To perform DRS measurements, the light source fiber was aligned to the PD1 aperture and diffuse reflectance was measured at PD1. For crosstalk measurements, the test was repeated with the source fiber aligned to the PD2 aperture while crosstalk signal was measured at PD1. The optical power incident on the phantom through these apertures ranged between 0.9-2.0 μW for the spectral range 470-600 nm.

Photocurrent was measured on a Keithley 4200 Source Measurement Unit (SMU). Custom control software written in LabVIEW controlled the monochromator wavelength setting, output shutter, and SMU current readings. For each phantom and curvature, three reflectance spectra readings were sampled, with 25 photocurrent measurements per reading at each wavelength, followed by 25 measurements of dark current. Between each reading, the liquid phantom was agitated with a pipette to prevent settling of the polystyrene microspheres on the transparent PET bottom surface. All measurements presented throughout this chapter represent an average of the 75 total photocurrent measurements.

Before recording a phantom measurement at each curvature, the photodetector probe was assembled into the appropriate 3D printed clamp and the optical source fiber was manually aligned to the photodiode aperture. Alignment was performed by maximizing the measured optical throughput through the PD aperture with an empty

phantom container. Optical throughput measurements were taken during each manual alignment with a calibrated silicon power meter (Thorlabs PM-100). After alignment was completed, a final optical throughput measurement was recorded and the fiber-to-PD alignment remained unchanged for the remainder of the phantom tests for that curvature. The diffuse reflectance was then measured by placing each phantom into the container separately and illuminating the PD aperture with the fiber.

After each reflectance measurement, the liquid phantom was replaced with a highly absorbing nigrosin solution ($\mu_a > 50cm^{-1}$), and a back illumination current measurement was taken. Back illumination refers to the background photocurrent generated from light incident upon the back of the PD, and illumination through the via that was absorbed by the PD but did not interact with the liquid phantom. For the thick silicon photodiode arrays, back illumination current results from light incident on the aperture sidewalls. In the thin film probe presented herein, sidewall absorption is negligible. However, background photocurrent was still present due to optical scattering from the PET film in the test assembly. For each curvature, the measured back illumination current was subtracted from the corresponding reflectance measurement to assess only the photocurrent due to diffuse reflectance. Using a highly absorbing water-based solution to measure back illumination ensures that the reflection and transmission from each optical index boundary remains the same as in the previous phantom

measurement. The back illumination current was measured to be 0.579-1.28 nA for 470-600 nm over all five curvatures. The average measurement to measurement variation in back illumination current at each curvature was 0.38%. The average variation of back illumination current across all curvatures was 28.7%, largely due to the difference in illumination geometry as a function of curvature.

The reflectance in DRS measurements is traditionally calculated by dividing the photocurrent recorded during a phantom measurement by the photocurrent recorded from a reflectance standard (a.k.a. "puck"). To correctly normalize for light source fluctuations and fiber-to-aperture alignment mismatch, a puck reflectance photocurrent value should be recorded before each phantom and curvature measurement. For the testing apparatus presented herein, it was not possible to bring a reflectance standard within a few millimeters of the photodetector after each alignment of the test setup. The 3D printed phantom chamber physically prevents bringing a puck close to the detector. Instead, as described above, the throughput power was recorded on a separate power meter. The puck reflectance photocurrent was measured separately with the photodetector probe held in an alternative, shorter 3D printed clamp that enabled close proximity between photodetector and puck. The flat phantom container clamp and the shorter puck measurement clamp are compared in Figure 45.

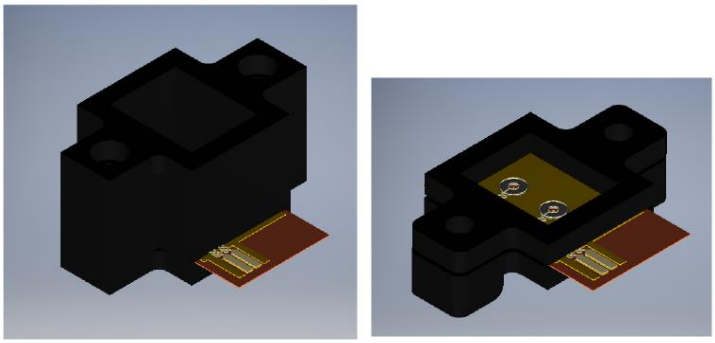

Figure 45. (a) Phantom measurement testing clamp for flat curvature; (b) shorter puck measurement testing clamp, enabling close proximity of puck to photodetector.

The puck photocurrent was recorded by placing a 99% diffuse reflectance standard (Labsphere, Inc. SRS-99-010) on top of the shorter 3D printed clamp and photodetector probe. The distance from the PD surface to the puck surface in this configuration is approximately 2.1 mm. The light source fiber, illuminated by the Xenon lamp and monochromator, was aligned to the aperture of PD1. The photocurrent from PD1 generated by the reflected light was recorded from 470nm to 600nm in 10nm steps on the Keithley 4200 SMU. The puck was then removed, and back illumination photocurrents were measured at the same wavelengths. Finally, throughput power was measured separately with an optical power meter (Thorlabs PM-100) without the puck present. The ratio of puck photocurrent (with back illumination subtracted) to throughput power was calculated for the wavelength range 470 to 600nm. The test was repeated three times with varying throughput power, showing an average variation of

1.4% in puck-to-throughput ratio. The average ratio from the three measurements was calculated and used in all subsequent puck scaling calculations.

The phantom reflectance at each test point was calculated by dividing the diffuse reflectance photocurrent by the puck reflectance photocurrent. The puck reflectance was estimated using the ratio of puck reflectance to optical throughput, where the optical throughput had been measured directly at each test point. The expression for phantom reflectance is:

$$R(\lambda,\rho,P) = \frac{\left(i_{phantom}(\lambda,\rho,P) - i_{backillum}(\lambda,\rho)\right)}{I_0(\lambda,\rho) \times \kappa(\lambda)} \qquad (4.1)$$

where $R(\lambda,\rho,P)$ is the reflectance at wavelength λ, for curvature ρ, for liquid phantom P; $i_{phantom}$ and $i_{backillum}$ are the photocurrent measurements of the phantom and back illumination, respectively; $I_0(\lambda,\rho)$ is the recorded optical throughput at each wavelength and curvature; and $\kappa(\lambda)$ is the ratio of puck photocurrent to optical throughput.

4.3 Liquid Phantoms

Liquid phantoms were prepared to represent human breast tissue (adipose and malignant) with scattering and absorbing coefficients within the range of reported values for wavelengths 470-600 nm [13]. The reduced scattering coefficient of biological tissue is described by Mie theory, since scattering occurs from small tissue particles with an optical index mismatch from the background material. For many tissue types (e.g.

skin, brain, breast, bone), the reduced scattering coefficient can be estimated with the following expression [20]:

$$\mu_s' = a\left(\frac{\lambda}{500nm}\right)^{-b} \tag{4.2}$$

where a is the normalized reduced scattering coefficient at 500 nm, and b is the "scattering power" that determines the wavelength dependence of μ_s'. A wide range of values for a and b have been reported for breast tissue [20]. The value of a varies from 8-30 cm^{-1}, with carcinoma tissue values trending higher than adipose. The b term is less dependent on tissue type, and typically ranges between 0.5 and 2.0 for breast tissue.

The absorption of breast tissue is determined by the concentration of chromophores, primarily hemoglobin and beta-carotene [13]. The absorption spectra of breast tissue can be expressed as a weighted sum of these chromophores [20]:

$$\mu_a = BS\mu_{a.oxy} + B(1-S)\mu_{a.deoxy} + W\mu_{a.water} + 2.3C_{\beta C}\varepsilon_{\beta C} \tag{4.3}$$

where B is the blood (hemoglobin) fraction, S is the blood oxygen saturation, W is the water content, $C_{\beta C}$ is the beta-carotene concentration, $\varepsilon_{\beta C}$ is the extinction coefficient of beta-carotene, and $\mu_{a.x}$ is the absorption coefficient of absorber x. In carcinoma breast tissue, the hemoglobin concentration averages 41.0 μM, as compared to 16-30 μM in normal tissue. Angiogenesis, the creation of new blood vessels in tissue, is increased in carcinoma where tumor tissue is in a stage of rapid growth [111]. The increase in hemoglobin content is a result of the increased angiogenesis.

Two phantoms were prepared, representing a benign (adipose) and a malignant breast tissue sample. Nigrosin absorber (Sigma-Aldrich) was mixed in deionized water with a concentration of 5.54×10^{-5} weight/volume (benign) and 1.10×10^{-4} w/v (malignant). In breast tissue, especially carcinoma tissue, hemoglobin is the primary absorber. The absorption spectra of hemoglobin and nigrosin are not identical. Therefore, the concentration of nigrosin was chosen such that a similar range of absorption values would result for the examined wavelengths of 470-600 nm. Optically scattering polystyrene spheres of 0.99 μm diameter (Polysciences, Inc.) were then added at a concentration of 2.24×10^{-3} w/v (benign) and 3.54×10^{-3} w/v (malignant). Scattering from these polystyrene spheres can be described using Mie theory. The absorption coefficient was calculated from spectrophotometer transmission measurements (Shimadzu UV-3600) of the phantom before adding the scattering polystyrene spheres. The scattering coefficient and anisotropy were estimated using Mie theory calculations [112]. The measured absorption and calculated scattering properties for both phantoms is shown in Figure 46.

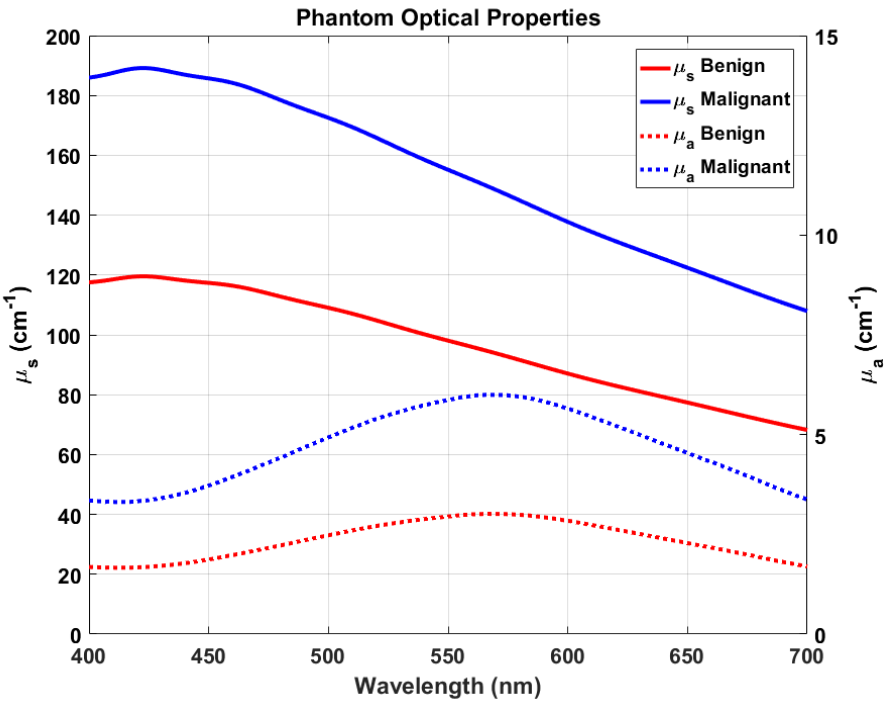

Figure 46. Absorption and scattering coefficients (μ_a and μ_s) of the liquid phantoms representing adipose and malignant breast tissue.

For the wavelength range 470-600 nm, the absorption coefficient ranged from 2.1 cm^{-1} to 6.0 cm^{-1}, and the scattering coefficient ranged from 87 cm^{-1} to 182 cm^{-1}. The anisotropy (g) ranged from 0.921 to 0.927. The reduced scattering coefficient, μ_s' [where $\mu_s' = \mu_s(1-g)$], ranged from 6.9 to 13.3 cm^{-1}.

4.4 Liquid Phantom Test Results and Analysis

This subsection presents the results of the diffuse reflectance measurements on the benign and malignant tissue mimicking liquid phantoms. Crosstalk results are also

shown for the benign phantom. The malignant phantom crosstalk optical power was below the noise floor of the photodetector and could not be measured.

4.4.1 DRS Signal Measurements

Reflectance data for both phantoms at each of the fourteen measured wavelengths, and at three of the five measured curvatures is shown in Figure 47. The 50mm and 25mm curvature are excluded from this plot for clarity.

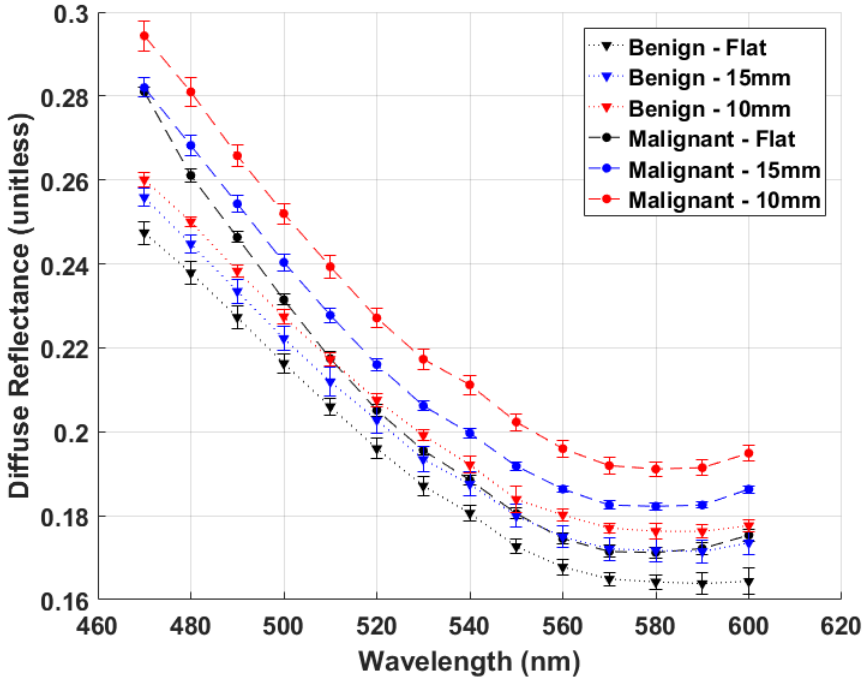

Figure 47. DRS versus curvature (inverse of radius) for both benign and malignant phantoms at fourteen wavelengths and three radii of curvature.

The measured phantom data shows an increasing reflectance signal with increasing curvature (decreasing radius) for both phantoms. The increase in DRS signal

due to curvature ranged from 5-8% for the benign phantom and 5-12% for the malignant phantom.

The increase in reflectance can be explained by the decrease in average source-detector distance while flexing. In the diffusion approximation [43], reflected intensity decreases as the source-detector distance increases. While in an inwardly curved state, the total path length within the bulk liquid phantom from optical source (PD aperture) to detector (PD surface) decreases. An illustration of a bending photodetector is shown in Figure 48.

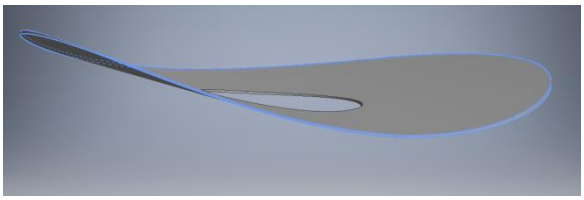

Figure 48. Photodetector surface shown at an exaggerated cylindrical bending radius (3mm). Outermost edges are highlighted in blue.

The decrease in path length as a result of bending can be described as an integral of the linear distance of the detector surface from the center of the optical aperture. The linear distance x from the center of the optical aperture to a point on the detector surface at radius r, with cylindrical bending radius ρ, and azimuthal angle (i.e., the rotational angle around the optical aperture), φ, is:

$$x = \frac{\rho}{\sin\varphi}\sqrt{2\left(1-\cos\left({}^{r\sin\varphi}/_{\rho}\right)\right)} \tag{4.4}$$

Taking advantage of the four-fold symmetry in this geometry, the average distance from aperture center to the radial edge can be found with an integral over one-quarter of the azimuthal rotation, φ = 0-90°. The average path length from the center of the aperture to the outermost edge of the photodetector (r = 1.25mm) slightly decreases with increasing curvature.

As a result of the decreasing path length, the optical reflectance incident at the photodetector surface increases with increasing curvature. The reflectance data from the benign phantom at all measured wavelengths is shown in Figure 49 as a function of curvature, with linear regression lines demonstrating the increase in reflection due to flexing. Curvature is defined as $1/\rho$, where ρ is the radius of curvature in millimeters.

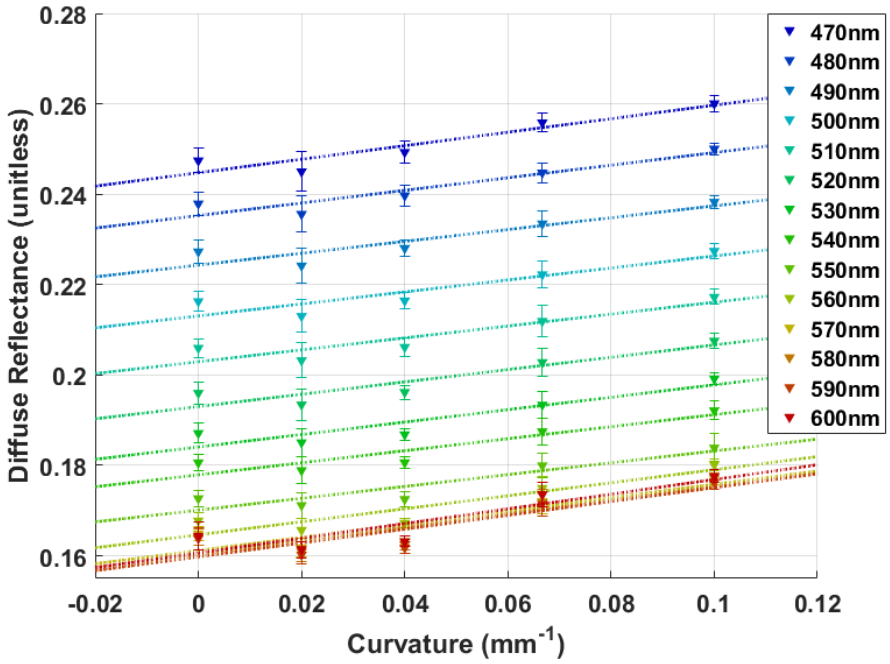

Figure 49. Reflectance as a function of curvature for the benign phantom. Linear regression lines are shown at each wavelength.

4.4.2 Crosstalk Measurements

The crosstalk between the two PDs was assessed by back illuminating the aperture of PD2 and measuring the PD1 photocurrent. The measured crosstalk is shown in Figure 50. The crosstalk reflectance is scaled similarly to the DRS reflectance; crosstalk photocurrent is divided by the puck reflectance for the measured optical throughput. For this experimental setup, the malignant phantom produced a significantly lower crosstalk signal, which is expected due to the high absorption of the malignant phantom.

Due to this high absorption, the crosstalk photocurrents for the malignant phantom were below the noise floor of the photodiode and could not be measured.

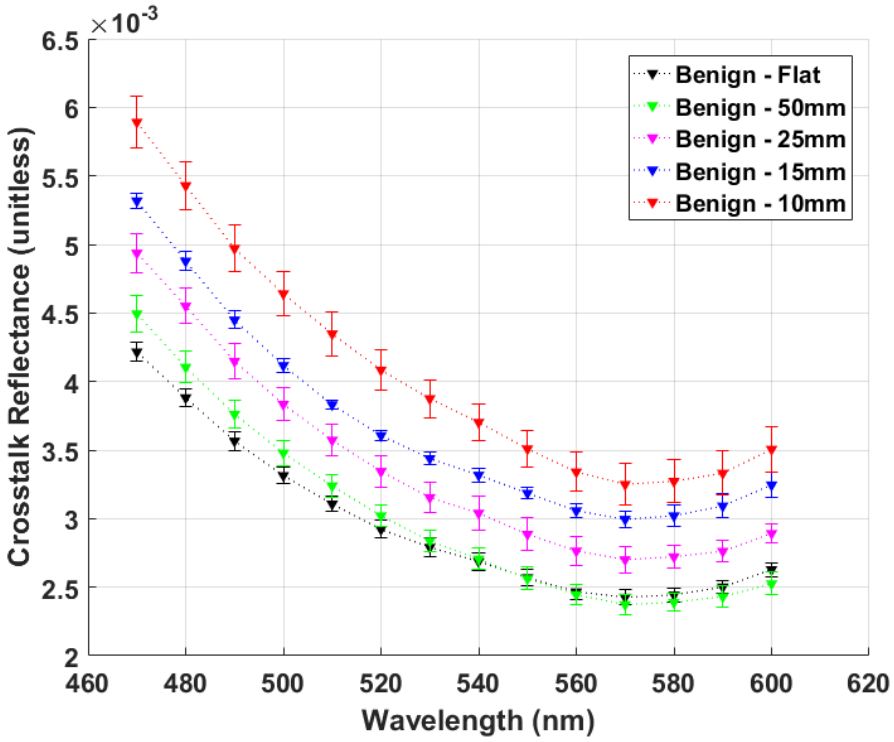

Figure 50. Crosstalk reflectance for the benign phantom at fourteen wavelengths and five radii of curvature.

As a percentage of the DRS signal, the maximum crosstalk of the benign phantom was 2.3% (λ = 470 nm, 10 mm radius of curvature). The percent crosstalk is shown in Figure 51.

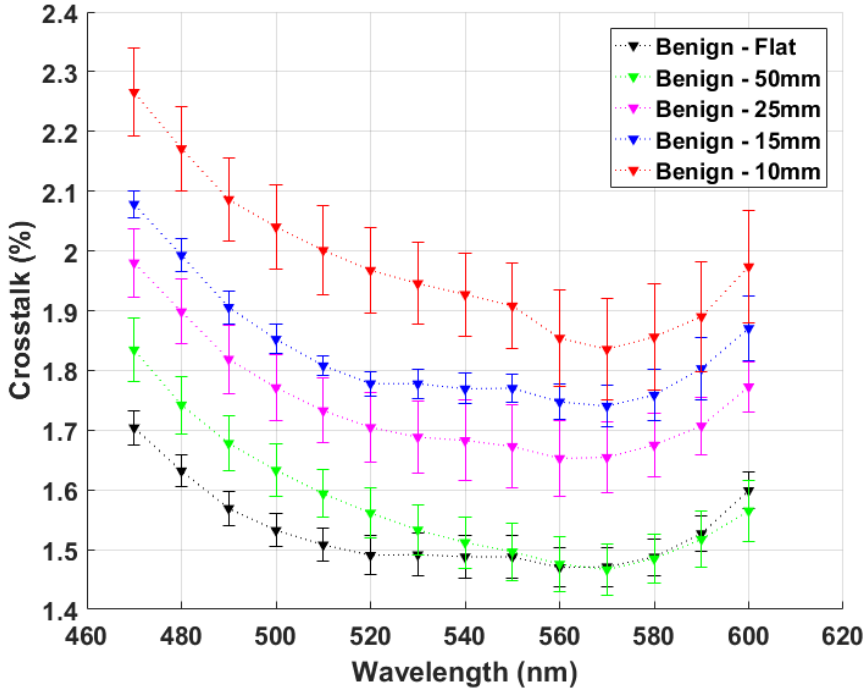

Figure 51. Crosstalk as a percent of DRS signal for the benign phantom at fourteen wavelengths and five radii of curvature.

This crosstalk value agrees with previously reported simulated values of crosstalk for a DRS system with similar, but rigid and flat, probe geometry [15]. The crosstalk signal increases by 40% from a flat surface to a 10 mm radius of curvature for the benign phantom. The decrease in path length due to increasing curvature is more pronounced in the case of the crosstalk detector than the flexed DRS case. We can estimate the reduction in path length to the crosstalk detector by examining the center-to-center distance during bending. This distance, x, can be described as:

$$x = 2\rho \sin \frac{D}{2\rho} \tag{4.5}$$

where ρ is the bending radius and D is the flat center-to-center pixel spacing. For D=4.5 mm, the distance x decreases from 4.5 mm when flat to 4.46 mm at a 10 mm radius of curvature.

Due to the higher reduction in path length, the signal is correspondingly higher under curvature. The crosstalk reflection of the benign phantom at all wavelengths is shown in Figure 52 as a function of curvature, with linear regression lines demonstrating the increase in reflection due to flexing.

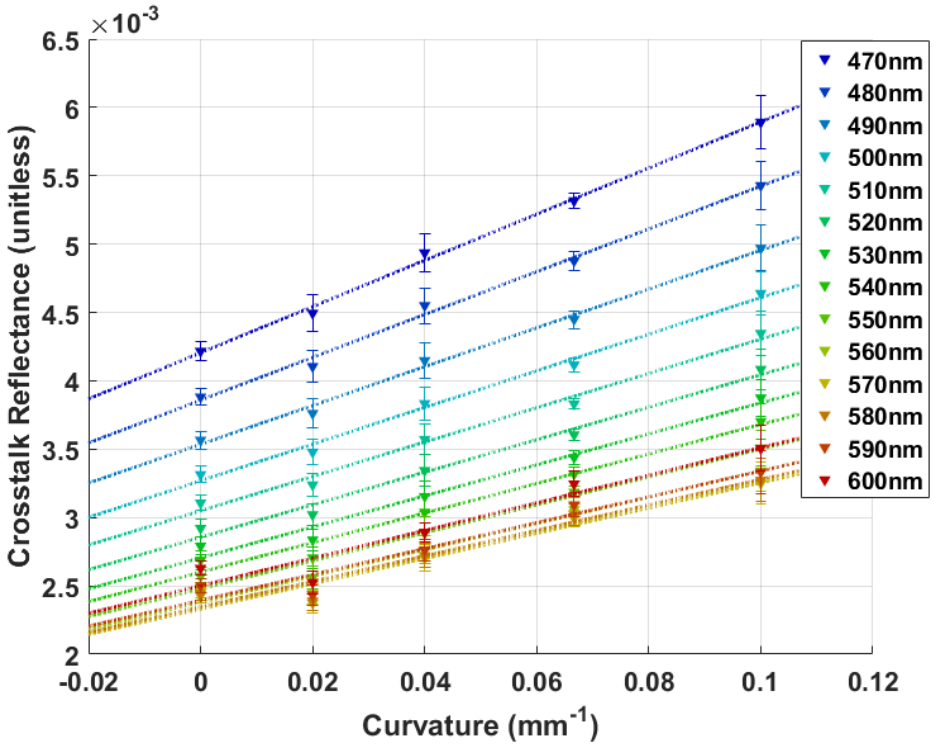

Figure 52. Crosstalk reflectance vs curvature for the benign phantom. Best fit lines are shown at each wavelength.

4.4.3 Signal Contrast

The ability to differentiate between benign and malignant tissue in a DRS system can be evaluated by the signal contrast, the relative difference in reflectance from the examined tissue or phantom. The signal contrast, $S_{i,\lambda}$, can be evaluated with the following expression:

$$S_\lambda = 100\frac{M_\lambda - B_\lambda}{B_\lambda} \tag{4.6}$$

where $M_{i,\lambda}$ and $B_{i,\lambda}$ are the malignant and benign diffuse reflectance measurements, respectively. For this definition, a "positive contrast" is when the malignant signal

exceeds the benign signal, and a "negative contrast" describes when the benign signal exceeds the malignant. Note that "positive" and "negative" in this context do not explicitly refer to differentiating between tissue types. In biological tissue, the sum of absorption from multiple chromophores may result in both positive and negative contrast across a full spectral measurement. However, since the phantoms used in the experiments in this thesis have only one chromophore and one scattering agent, the contrast is expected to be positive at all wavelengths.

For the flat phantom measurements in this report, the signal contrast ranged from 4.0% at 570 nm to 13.6% at 470 nm. At all flat wavelengths, the reflectance from the malignant phantom was higher than that of the benign phantom. Additionally, when comparing only the benign and malignant phantom reflectance at the same radius of curvature, contrast remains positive. The signal contrast at each curvature is shown in Figure 53.

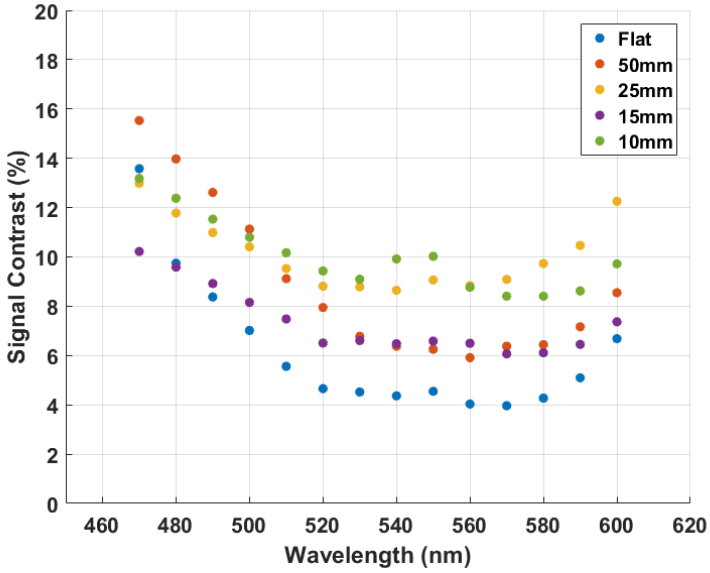

Figure 53. Signal contrast between benign and malignant phantoms at flat and flexed conditions. Contrast remains positive when comparing phantom measurements both at the same curvature.

The diffuse reflection from the benign and malignant liquid phantoms show a decrease in reflected optical power at longer wavelengths, coincident with the peak absorption of nigrosin at approximately 570 nm. Since both phantoms use the same chromophore for the absorbing agent, the percent change in the coefficient of absorption as a function of wavelength is identical for the benign and malignant phantoms. However, the percent change of albedo from 470 to 570 nm is higher for the malignant phantom (14.5%) than the benign (12%). The decrease in reflection for longer wavelengths is higher in the malignant phantom than in the benign. The contrast

decreases with increasing wavelength due to the differences in the change in reflection from the benign and malignant phantoms.

The malignant phantom shows a larger increase in reflectance due to curvature than the benign. However, due to the decreased contrast at longer wavelengths, at $\lambda >$ 520 nm the 10 mm flexed benign phantom reflectance exceeded that of the flat malignant phantom. The flexed benign phantom also exceeds the un-flexed malignant at 15 mm radius of curvature for 560nm $< \lambda <$ 580nm. If during an examination tissue curvature is unknown (i.e. all tissue is assumed to be the same curvature), this result shows negative contrast.

It has been shown that the radius of curvature of the turbid media under DRS examination has an effect on the diffuse reflectance signal. With prior knowledge of the curvature for recorded DRS signals, an estimate can be made for the reflectance of a flat sample of the same tissue optical properties. However, the effect of curvature on reflectance is dependent on the scattering and absorption properties of the tissue. The malignant phantom demonstrated a larger increase in reflectance due to curvature than the benign phantom. A correct estimation of the flat DRS signal from a measurement under curvature requires first an estimation of the optical properties. Since the estimation of tissue optical properties is frequently the goal of a DRS examination, the requirement of their prior knowledge in this task would appear to impede optical

property extraction. However, feature extraction through an inverse Monte-Carlo method requires an initial estimate of scattering and absorption coefficients as inputs into the forward model [46]. Through repeated iterations, the inverse Monte-Carlo method converges on the correct optical properties. If the surface curvature during measurement is known, its effect on diffuse reflectance may be included in the forward model.

In summary, the flexible photodiode PD1 exhibits measured responsivity and dark current characteristics comparable to previously reported traditional thick silicon arrays. The diffuse reflectance spectroscopy measurements on tissue mimicking phantoms under flat and flexed conditions demonstrate an increase in responsivity due to flexing, which can be expected as a result of the reduction in effective path length from optical source to detector. The signal contrast between benign and malignant phantoms can be adversely affected by an unknown tissue curvature, but remains positive for comparisons of benign and malignant phantoms at the same curvature.

5. Monte Carlo Simulations

This chapter describes simulations of diffuse reflectance and crosstalk from the fabricated PDs on tissue-mimicking phantoms, modeled with commercial ZEMAX ray-tracing software. The bulk scattering mode, a Monte Carlo modeling algorithm, was used to model the tissue reflectance and crosstalk over a spectral range of 470-600 nm and over flat and curved PD conditions.

5.1 Optical Modeling of Biological Tissue

Monte Carlo (MC) modeling is a highly accurate method in simulating optical transport phenomena in biological tissue [113]. Analytical solutions, such as the diffusion approximation, are valid either only for a few simple geometries (e.g. a flat slab) or for a limited range of absorption coefficients [114]. For instance, highly absorbing tissue or highly anisotropic scattering greatly reduces the accuracy of the diffusion approximation [115]. In contrast, the accuracy of MC modeling is tunable, limited by the required computational load of the simulation.

MC modeling of optical interactions in tissue simulates a random walk for individual photons, generated by sampling from a probability distribution. The aggregate sum of the photon paths represents the numerical approximation of the true physical system: the optical interaction of light with biological tissue. The accuracy of

such a method depends on a large number of simulated photons, typically 10^5 or more [116].

The MC model of light transport in tissue requires three parametric inputs: mean free path, albedo, and the scattering phase function. The mean free path and albedo are directly related to the absorption and scattering coefficients, μ_a and μ_s. The mean free path, $\bar{l}$, is the average path length a photon travels before an interaction with a scattering or absorbing center [22]:

$$\bar{l} = \frac{1}{\mu_a + \mu_s} \tag{5.1}$$

The albedo, *a*, is the fraction of light transmitted at every photon interaction. This fraction is equal to the ratio of scattering coefficient to the total extinction coefficient (sum of scattering and absorbing coefficients) [22]:

$$a = \frac{\mu_s}{\mu_a + \mu_s} \tag{5.2}$$

The scattering phase function is a probabilistic distribution of the deflection angle of a scattered photon. In biological tissue, photon scattering follows the Henyey-Greenstein distribution discussed in Chapter 2. The phase function, $p(\cos\theta)$, describes the probability that a photon will be scattered with angle θ. To use this phase function in a simulation, a modified function can be derived that generates a scattering angle, θ, when given a random variable uniformly distributed between 0 and 1. For the Henyey-

Greenstein phase function $p(\cos\theta, g) = (1-g^2)/(1+g^2-2g\cos\theta)^{3/2}$, the scattering generator function is [117]:

$$y(\zeta, g) = \frac{1}{2g}\left[1 + g^2 - \left(\frac{1-g^2}{1+g-2g\zeta}\right)^2\right] \tag{5.3}$$

Where g is the anisotropy ($g = \langle\cos\theta\rangle$), ζ is a random variable between 0 and 1, and the function output, y, is the cosine of the scattering angle, θ. These two functions, $p(\theta, g)$ and $\theta(\zeta, g)$ are shown in Figure 54 for multiple values of g.

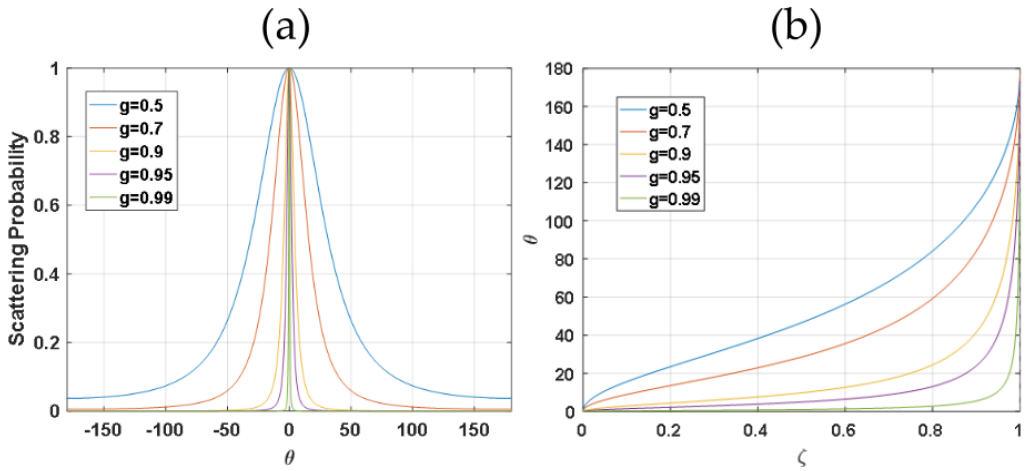

Figure 54. Henyey-Greenstein (a) scattering probability function; and (b) Monte-Carlo generator function for scattering angle at multiple values of anisotropy.

The MC model propagates each photon in discrete steps. The mean free path determines the step length between optical interactions. The step length, Δs, is probabilistically generated following Beer's law, where the probability of a short path is higher than a long path, and the probability is proportional to $e^{-\bar{l}\Delta s}$ [22]. The step size

can be generated with a random variable, ζ, between 0 and 1 with the following relationship [22]:

$$\Delta s = -\bar{l}\ln(\zeta) \tag{5.4}$$

In the MC model, propagation involves the following steps: (1) a photon is moved along its current trajectory a distance of Δs, then (2) unless the photon exits the media, it is scattered to a new angle θ and ϕ (the azimuthal angle, ϕ, is uniformly distributed between 0-2π), and (3) the optical power of the photon, or "weight", is decreased by 1-*a*. If the photon weight is below a minimum threshold, it is terminated. Otherwise, program flow returns to (1) and the random walk continues. Once the photon is terminated, a new photon will be simulated until the total number of simulated photons is reached. The step size Δs and scattering angle θ are randomly generated for each iteration of the photon random walk.

The Monte Carlo simulations of the flat and curved phantom measurements were conducted in Radiant Zemax, a commercial ray-tracing optics simulator. The geometry in the simulation matched that of the experimental system. The liquid phantom volume was 10x10x12 mm, with absorbing side and back walls. The index of refraction of the phantom was the same as water, with bulk scattering turned on, and the phase function determined by Henyey-Greenstein statistics. A 50 μm thick PET film was placed on the front surface of the phantom. The thin film silicon photodetectors

were a 10 μm thick annulus, with a 1.25 mm outer diameter and a 0.375 mm inner radius, with a cylindrical bend ranging from flat to 10 mm radius of curvature. Five versions of this photodetector, one for each curvature, were modeled in Autodesk Inventor and imported into Zemax as STL files. A separate simulation was conducted for each μ_a and μ_s pair for both liquid phantoms at fourteen discrete wavelengths: 470 nm to 600nm in steps of 10 nm. For each of these μ_a and μ_s pairs, five simulations of 10^7 photons were conducted at each of the five radii of curvature: flat, 50mm, 25mm, 15mm, and 10mm. The simulated geometry is shown in Figure 55.

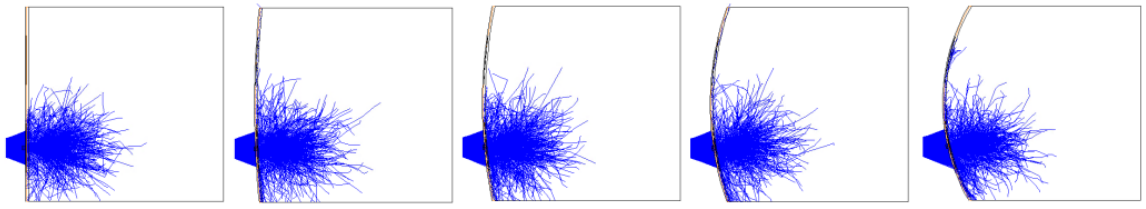

Figure 55. Zemax simulation geometries for (a) flat; (b) 50mm; (c) 25mm; (d) 15mm; and (e) 10mm radius of curvature. Blue lines are photons paths, including photons bulk scattered within the phantom after entering through the 200 μm radius photodiode aperture. For clarity, a reduced number of photon paths (10,000) are shown.

The simulated light source in the Zemax model is based on the "Source Fiber" object. This source object emits a circular beam of light with varying radial intensity and an option for fixed or varying numerical aperture (NA) in the radial direction. The optical fiber used in the experimental setup is a 1 mm diameter, multimode fiber with NA=0.39 (Thorlabs FT1000UMT). The divergence of the fiber was verified using a

Hitachi KP-D20BU CCD camera, with spot size images taken at three positions from the fiber tip: 0 mm, 1 mm, and 2 mm. The light source was the same Xenon lamp and monochromator discussed in Chapter 4, with the grating output centered at 600nm. The beam images and beam width measurements are shown in Figure 56. The beam width was analyzed in MATLAB for each image, where the width was defined as the distance between the points where the CCD intensity (the output of an 8-bit ADC, maximum value = 255) is half of the maximum. The beam width was calculated to be 4.26 mm, 4.48 mm, and 5.09 mm for the 0 mm, 1 mm, and 2 mm displacements, respectively. These measurements correspond to a divergence angle of approximately 22.6°, equivalent to an NA of 0.38.

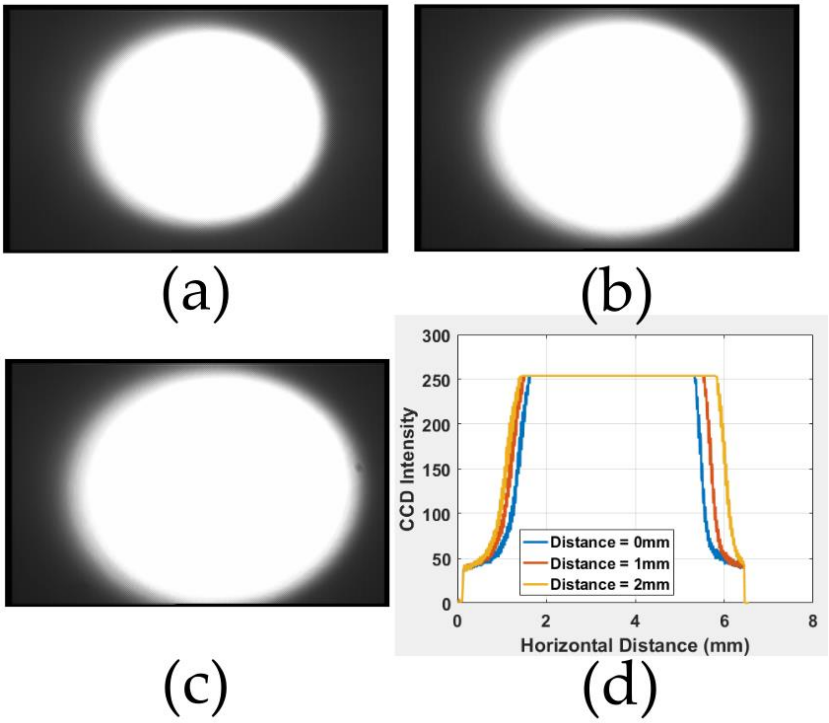

Figure 56. Beam images of the 1mm core fiber taken at vertical distances of (a) 0mm; (b) 1mm; and (c) 2mm; and (d) the horizontal intensity for the three images taken at the widest point in each beam.

The front surface of the PET film was modeled as a Lambertian scatterer in Zemax. The total reflected power from a surface in Zemax is calculated by the index of refraction mismatch. However, the fraction of scattered light versus specular reflection is increased by adjusting the "scatter fraction". The scatter fraction was informed experimentally by illuminating the flat phantom measurement system, just as in a phantom experiment, but the phantom chamber was empty. In the absence of phantom diffuse reflectance, the backscattered light from the PET film was measured by the fabricated thin film silicon photodetector. Optical throughput was measured on an

optical power meter (Thorlabs PM-100). The backscatter power averaged over 50 measurements was 7.6nW and the throughput was 1.85μW. The Zemax scatter fraction that most closely reproduced these experimental results of backscatter and throughput power was 0.45. This value was then used for the PET scatter fraction for all subsequent simulations.

The Henyey-Greenstein phase function is a good model for biological tissue, but the tissue phantoms mixed and evaluated in this thesis only contain polystyrene sphere scatterers of a single known size, which have scattering phase functions that can be fully described by Mie theory. The integral of the Henyey-Greenstein phase function is invertible [117], which enables the derivation of the generation function discussed earlier. However, this is not true for the Mie phase function, and it is therefore more computationally difficult to simulate [117]. However, the difference in phase function between Mie and Henyey-Greenstein theory for the same anisotropy differs mainly in the backscattering probabilities, as shown in Figure 57. The Mie probability distribution was calculated for 0.99 μm polystyrene spheres in water at 470 nm as described in [112] and [118]. The anisotropy calculated by Mie theory for this scattering probability density was g=0.927.

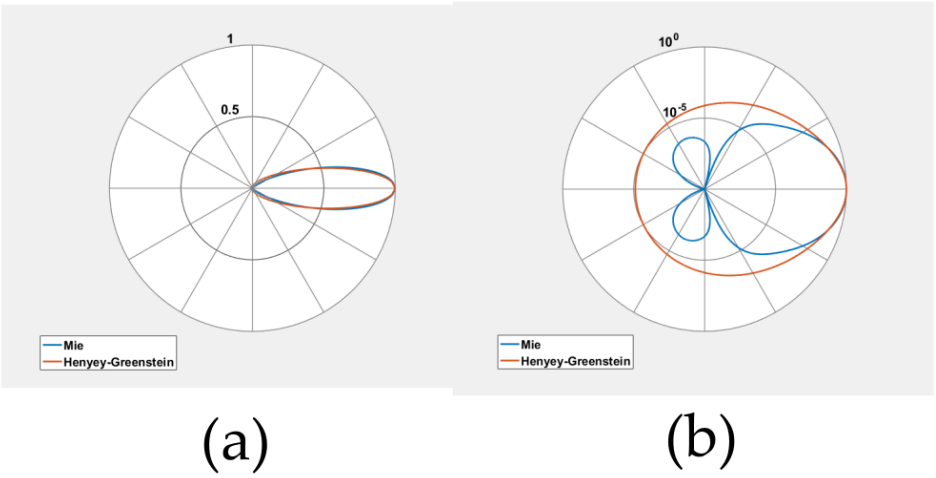

Figure 57. Mie (blue) and Henyey-Greenstein (red) phase functions shown on (a) linear scale and (b) logarithmic scale for g = 0.927. Forward scattering (0°) is to the right.

The effect of backscattering is more prominent at close source-detector distances, when a photon experiences very few scattering interactions before being collected by a detector. This is known as the "non-diffuse regime." In this regime, the Henyey-Greenstein phase function inaccurately predicts the relatively large contribution from backscattered light [119]. The Mie phase function or a modified Henyey-Greenstein function (which includes a Rayleigh scattering term) is more appropriate for the non-diffuse regime. A "diffuse regime parameter", $\rho \times \mu_s'$, is defined where ρ is the source-detector distance. For larger values $\rho \times \mu_s'$, Mie and Henyey-Greenstein match well [120]. As illustrated in Figure 58, simulations based on the two phase functions diverge at $\rho \times \mu_s' < 0.6$ [120]. For the experimental and simulated geometry in this thesis, the average source-detector distance is approximately 0.99 mm (the radial center of mass of the

annulus), and simulated and experimental phantom μ_s' ranges from 0.7 to 1.3 mm. The fixed source-detector distance and phantom reduced scattering range remains in mostly in the diffuse regime. For this regime, the Henyey-Greenstein phase function is an appropriate model for MC simulations. For the benign phantom, the lower reduced scattering coefficient at longer wavelengths approaches the non-diffuse regime, which may reduce the accuracy of a Henyey-Greenstein based MC simulation.

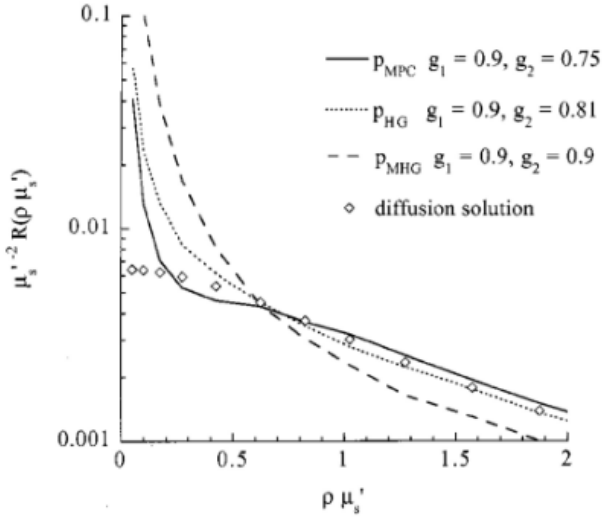

Figure 58. Scaled reflection as a function of diffusion regime parameter, $\rho \times \mu_s'$, for Mie (solid line), Henyey-Greenstein (dotted line), Modified Henyey-Greenstein (dashed line), and diffusion approximation. Mie and Henyey-Greenstein are well matched for larger values of $\rho \times \mu_s'$ [120].

5.2 Monte Carlo Simulations of Diffuse Reflectance and Crosstalk

MC simulations in Zemax were conducted for the two phantoms representing benign and malignant breast tissue discussed in Chapter 4. The inputs to the bulk scattering model for each wavelength and phantom are shown in Table 2.

Table 2. Phantom properties applied to Monte Carlo simulations.

Wavelength (nm)	Benign Phantom			Malignant Phantom		
	μ_s' (cm^{-1})	μ_a (cm^{-1})	g	μ_s' (cm^{-1})	μ_a (cm^{-1})	g
470	8.382	2.099	0.9270	13.26	4.177	0.9270
480	8.244	2.224	0.9269	13.04	4.425	0.9269
490	8.136	2.353	0.9266	12.87	4.683	0.9266
500	8.021	2.477	0.9264	12.69	4.930	0.9264
510	7.887	2.599	0.9263	12.48	5.172	0.9263
520	7.738	2.709	0.9262	12.24	5.391	0.9262
530	7.584	2.800	0.9260	12.00	5.572	0.9260
540	7.435	2.881	0.9258	11.76	5.733	0.9258
550	7.296	2.947	0.9256	11.54	5.865	0.9256
560	7.175	3.003	0.9252	11.35	5.975	0.9252
570	7.078	3.013	0.9246	11.20	5.996	0.9246

Wavelength (nm)	Benign Phantom			Malignant Phantom		
	μ_s' (cm^{-1})	μ_a (cm^{-1})	g	μ_s' (cm^{-1})	μ_a (cm^{-1})	g
580	7.010	2.990	0.9235	11.09	5.949	0.9235
590	6.961	2.927	0.9220	11.01	5.825	0.9220
600	6.917	2.840	0.9206	10.94	5.652	0.9206

For each phantom, wavelength, and curvature, MC simulations with 10^7 launched photons were conducted. The sum of the optical power of all photons that were detected by the DRS photodiode annulus was recorded for each simulation.

Zemax simulations were also performed on a 99% reflective Lambertian scattering surface to provide a normalization basis for the diffuse reflectance. This simulation is similar to the method used in calculating reflectance as a ratio of the "puck" reflectance standard in the experimental data presented in Chapter 4. First, throughput simulations were performed on a simulation mimicking the phantom measurement system with an empty phantom chamber (air filled volume, no bulk scattering). Five simulations of 10^7 photons were performed for each wavelength and curvature. As the curvature in the simulation increased, the distance from light source to optical aperture increased. The optical power entering the phantom decreased as a function of curvature due to the divergence of the light source. The average throughput

(from the 35μW fiber source) decreased from 1.27 μW while flat to 1.06 μW at a 10 mm radius of curvature. The variation in throughput as a function of wavelength was approximately ±0.25%.

In addition to the throughput simulations, reflectance standard "puck" simulations were performed. The Lambertian scattering surface was placed 2.1 mm away from the photodetector, which was non-flexed. The simulated reflected power collected on the photodetector was scaled to the throughput for that simulation, and used in subsequent calculations as the reflectance standard measurement.

The reflected optical power was then divided by the puck power, resulting in the simulated reflectance for the benign and malignant phantoms at each curvature and wavelength. The simulated reflectance is shown in Figure 59.

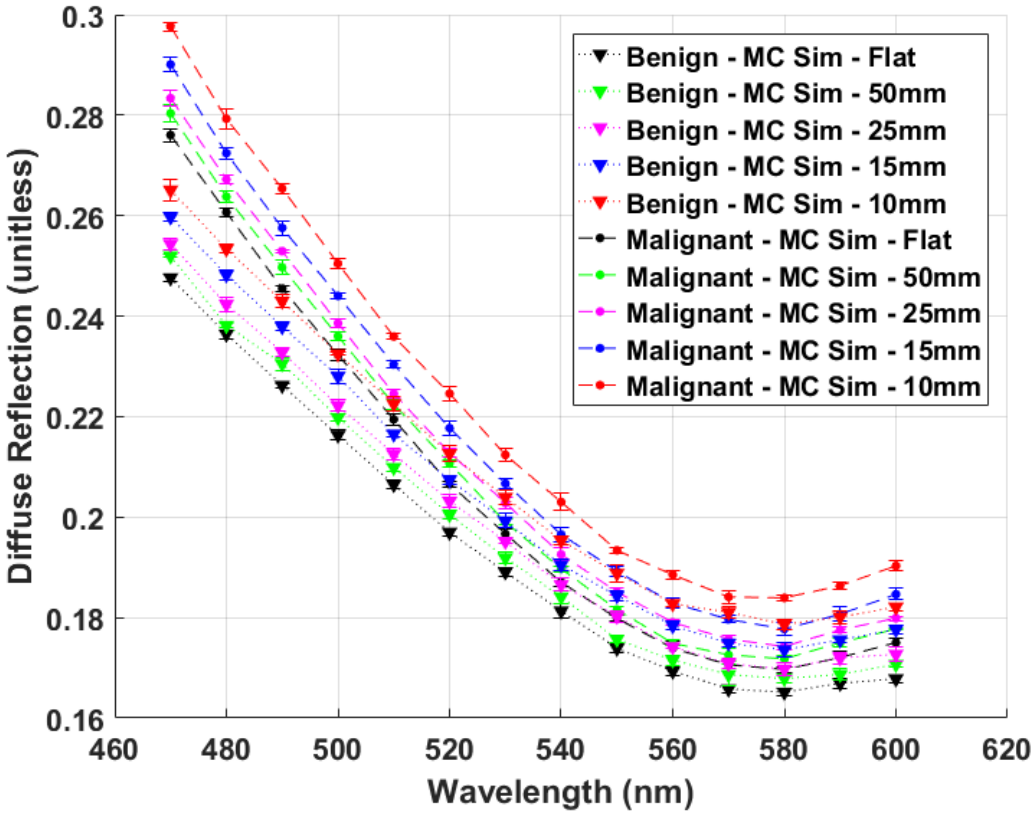

Figure 59. Simulated reflectance of malignant (circles) and benign (triangles) scaled by throughput power as a function of curvature for 14 wavelengths.

Crosstalk simulations were also performed. During each simulation, an additional detector located 4.5 mm away on the phantom surface collected the crosstalk reflectance power. The simulated crosstalk values were scaled to the puck simulation in order to calculate the crosstalk reflectance. The simulated crosstalk reflectance is shown in Figure 60.

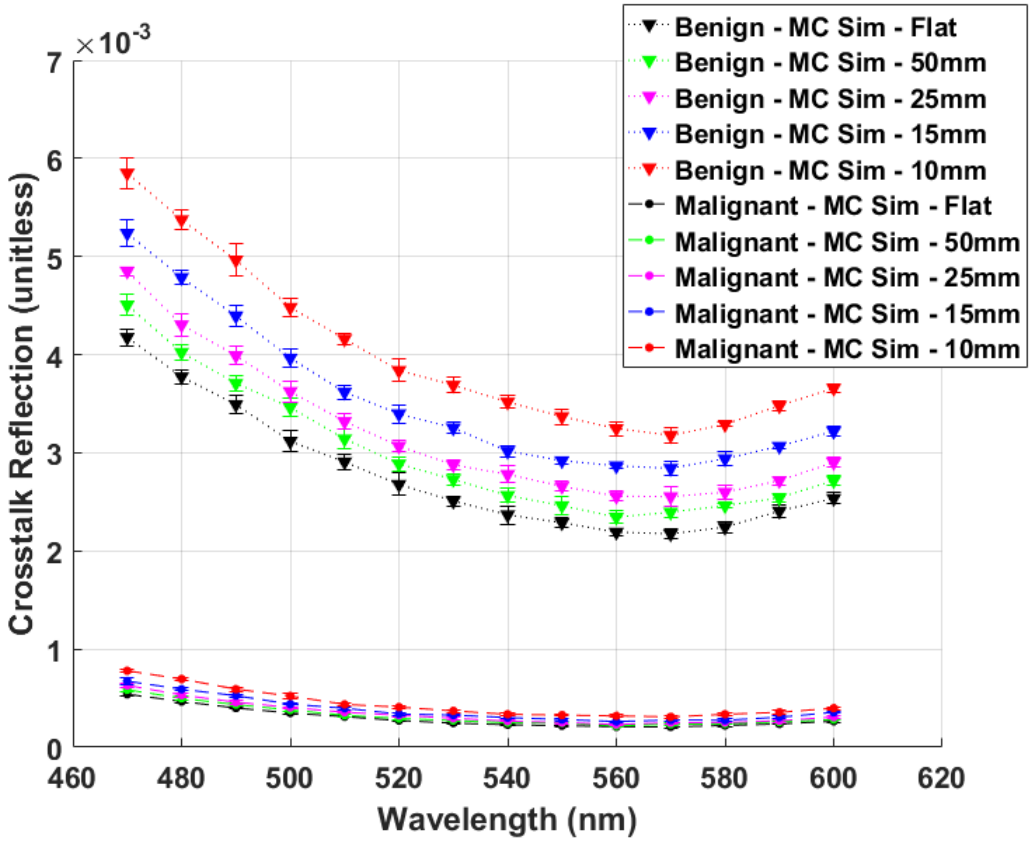

Figure 60. Simulated cross talk reflectance of malignant (circles) and benign (triangles) scaled by throughput power as a function of curvature for four wavelengths.

5.3 Analysis

The simulations of diffuse reflectance on flat and curved tissue phantoms show a correlation between curvature (reciprocal of radius) and reflection. This correlation is similar to that seen in the experimental data in Chapter 4; the diffuse reflection signal increases with increasing curvature. The simulation data points fit to a linear regression line with R-squared goodness-of-fit parameter averaging 0.991 for all simulations (0.992

for DRS data, 0.989 for crosstalk). DRS and crosstalk simulations with linear fits are shown for five wavelengths in Figure 61.

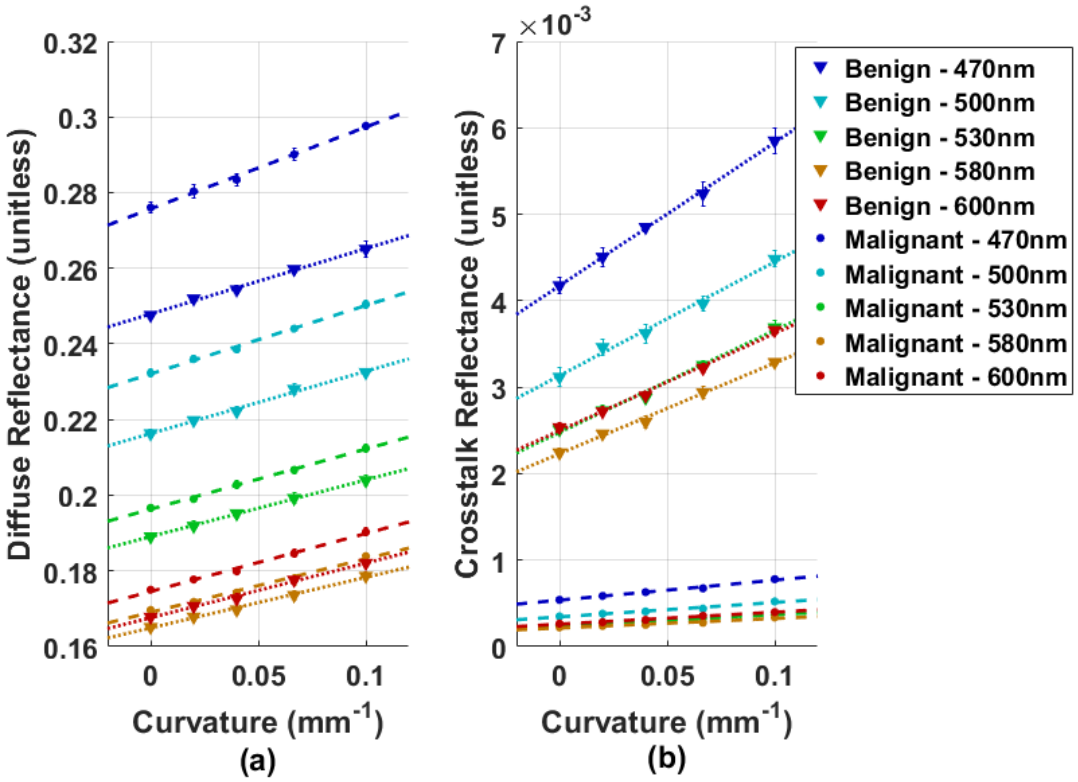

Figure 61. Simulated reflectance vs curvature of the malignant phantom (circles) and benign phantom (triangles), with linear regression (malignant: dashed lines, benign: dotted lines). (a) Diffuse Reflectance simulations; (b) Cross Talk simulations

The MC simulations at each wavelength, phantom, and curvature were each performed five times with 10^7 photons. Since all five simulations were averaged, the results are equivalent to performing a single simulation with $5x10^7$ photons. However, by splitting the simulation into multiple, smaller simulations, one can determine the precision of the modeled data by examining the variation between simulation runs. For

geometries with a high number of photons collected at the detector, the variance between simulations was relatively low. The diffuse reflectance experiments, where photons were measured at the detector closest to the light source, ranged from 165,000 to 220,000 detected photons for the benign phantom and to 260,000 to 350,000 for the malignant phantom. The simulated detected optical power varied 0.38% for the malignant phantom and 0.46% for the benign phantom. For the crosstalk experiments, where photons were collected at a detector positioned 4.5mm away from the optical source, the number of detected photons was far lower for the same number of total simulated photons. There were 30,000 to 36,000 simulated photons incident on the benign crosstalk detector, and 18,000 to 21,000 on the malignant cross talk detector. However, the number of detected photons was still high enough to generate repeatable data: the simulated crosstalk power varied 1.66% for the benign phantom and 3.10% for the malignant phantom.

While more data points would be required to fully characterize the relationship between reflection and curvature, it appears that the increase in reflection is monotonic. Additionally, the increase occurs for all examined μ_a and μ_s' pairs, i.e. for both phantoms at all wavelengths, as well as for both the DRS signals and crosstalk signals. This increase in reflection can be explained by the decrease in effective path length between source and detector, as discussed in Chapter 4. As curvature increases, so too does the

crosstalk as a percentage of the DRS signal; the increase due to curvature is higher in the crosstalk signal than in the DRS signal. The percentage crosstalk is shown in Figure 62 and Figure 63 for benign and malignant phantoms, respectively.

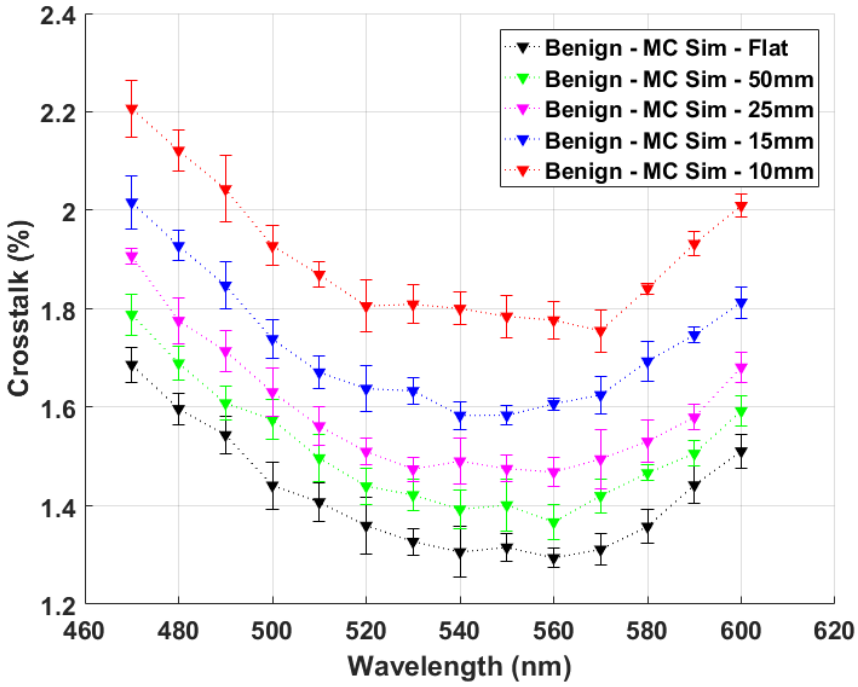

Figure 62. Crosstalk, as a percentage of the DRS signal, for the benign phantom over five curvatures.

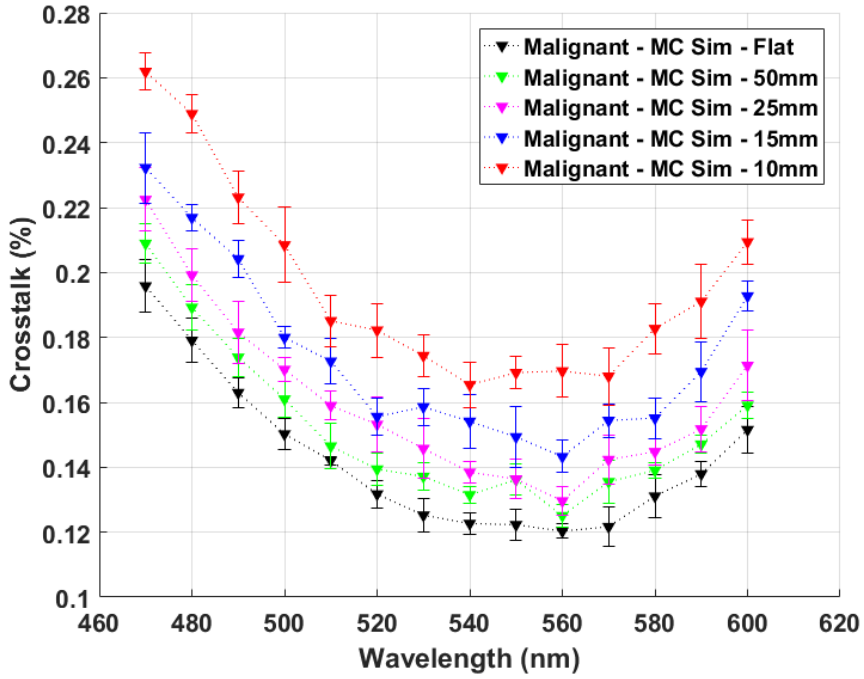

Figure 63. Crosstalk, as a percentage of the DRS signal, for the malignant phantom over five curvatures.

The increase in percent crosstalk, averaged across all wavelengths, from the flat test case to a 10 mm radius of curvature is 34.2% for the benign phantom (increasing from 1.4% to 1.9%) and 37.5% for the malignant phantom (0.14% to 0.20%). The increase in percent crosstalk due to curvature was higher for the malignant phantom, which had higher coefficients of scattering and absorption than the benign phantom. However, the percent crosstalk was lower in the malignant phantom than in the benign for all curvatures and wavelengths. Although the effect of curvature caused a higher increase in percent crosstalk in the malignant phantom, the starting value of crosstalk at the flat

condition was much lower than for the benign phantom. The maximum percent crosstalk of 2.2% occurs for the benign phantom at 470 nm for the 10 mm radius of curvature. This percent crosstalk remains below the 6-9% maximum percent crosstalk reported for previous DRS systems with similar pixel-to-pixel spacing [13], [34].

6. Comparison of Theory and Experiment

This chapter presents the comparison of Monte Carlo diffuse reflectance simulations with the measured experimental results of diffuse reflectance on tissue-mimicking phantoms. There is good agreement between theory and experiment, with a mean percent error of 2.33% for the benign and 1.23% for the malignant diffuse reflectance signals, and 4.85% error for the benign phantom crosstalk signal.

6.1 Comparison of Diffuse Reflectance

The diffuse reflectance, plotted as a function of wavelength, for both benign and malignant phantoms shows good agreement between simulation and experiment. Both the experimental data and simulations of reflected optical power are presented as a ratio to the reflectance of a 99% reflectance standard to provide equivalent scaling of the results. The overplots of simulation and experiment are shown in Figures 64-68.

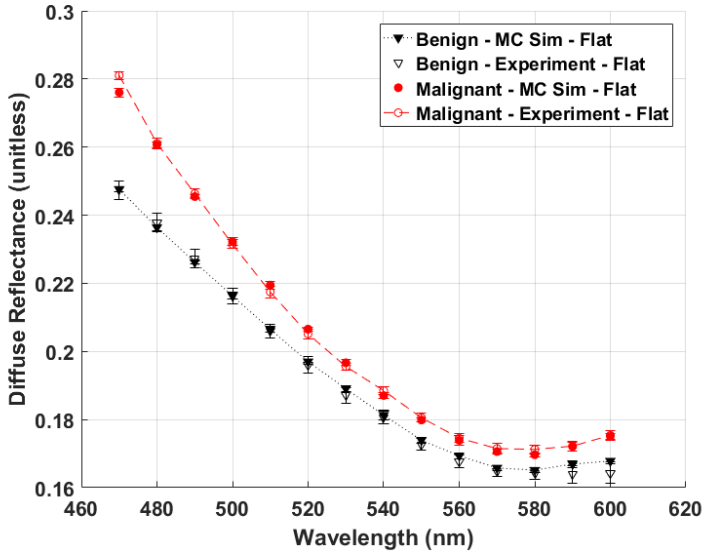

Figure 64. Diffuse reflectance of malignant (circles) and benign (triangles) phantoms, overlaying experimental (open symbols) and simulated (filled symbols) data for the flat test case.

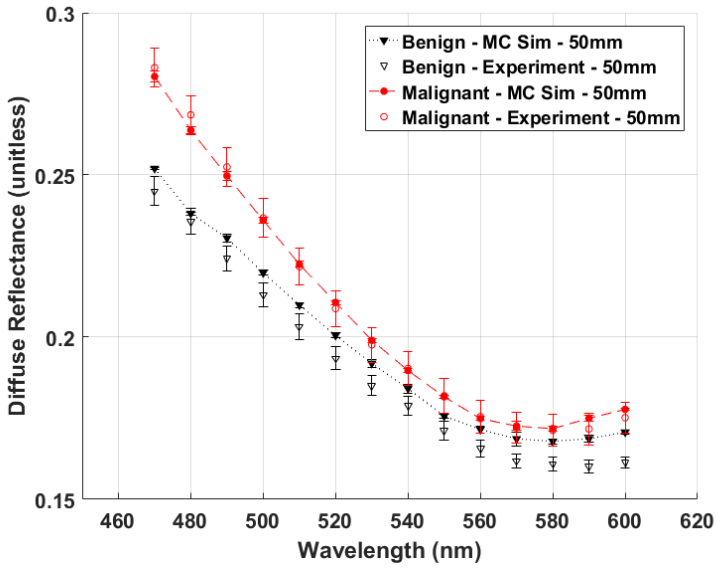

Figure 65. Diffuse reflectance of malignant and benign phantoms for the 50 mm radius test case.

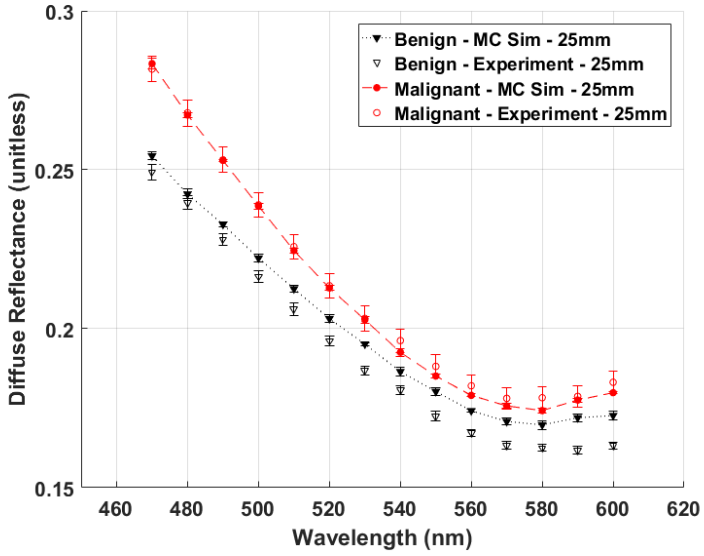

Figure 66. Diffuse reflectance of malignant and benign phantoms for the 25 mm radius test case.

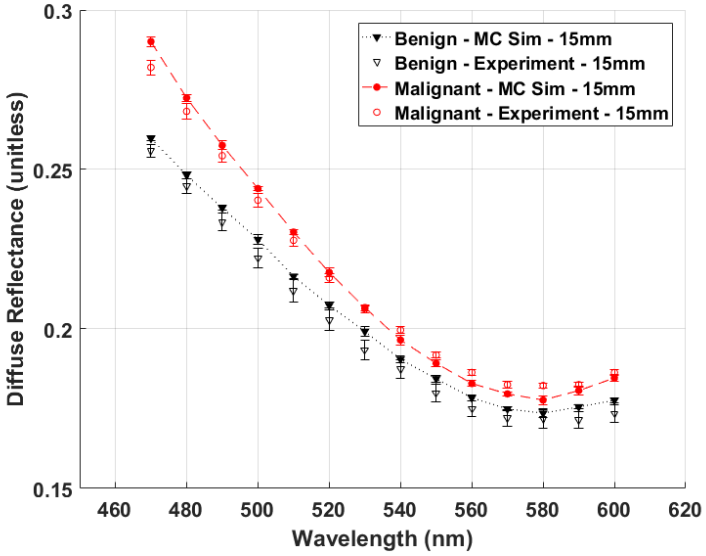

Figure 67. Diffuse reflectance of malignant and benign phantoms for the 15 mm radius test case.

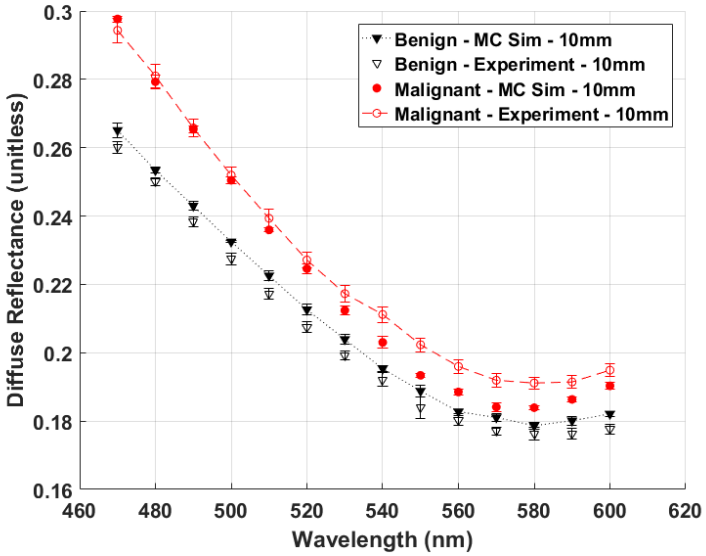

Figure 68. Diffuse reflectance of malignant and benign phantoms for the 10 mm radius test case.

The mean percent error between simulation and experiment is 2.33% for the benign phantom and 1.23% for the malignant phantom averaged over all wavelengths and curvatures. The average mean percent error for each curvature is listed in Table 3.

Table 3. Mean percent error for benign and malignant phantoms, averaged for each of five curvatures.

Radius of Curvature (mm)	Benign Phantom Mean Percent Error	Malignant Phantom Mean Percent Error
∞	0.71%	0.58%
50	3.39%	0.77%
25	3.57%	0.97%
15	1.98%	1.44%
10	2.01%	2.38%

The data points for simulated results are each the average of five simulations with 10^7 photons. The data points for the experimental results are the average of three reflectance experiments, each averaging 25 measurements of photocurrent. In Figure 69, the reflectance of five wavelengths is shown plotted against curvature, with all experimental and simulation radii (flat, 50 mm, 25 mm, 15 mm, and 10 mm) shown.

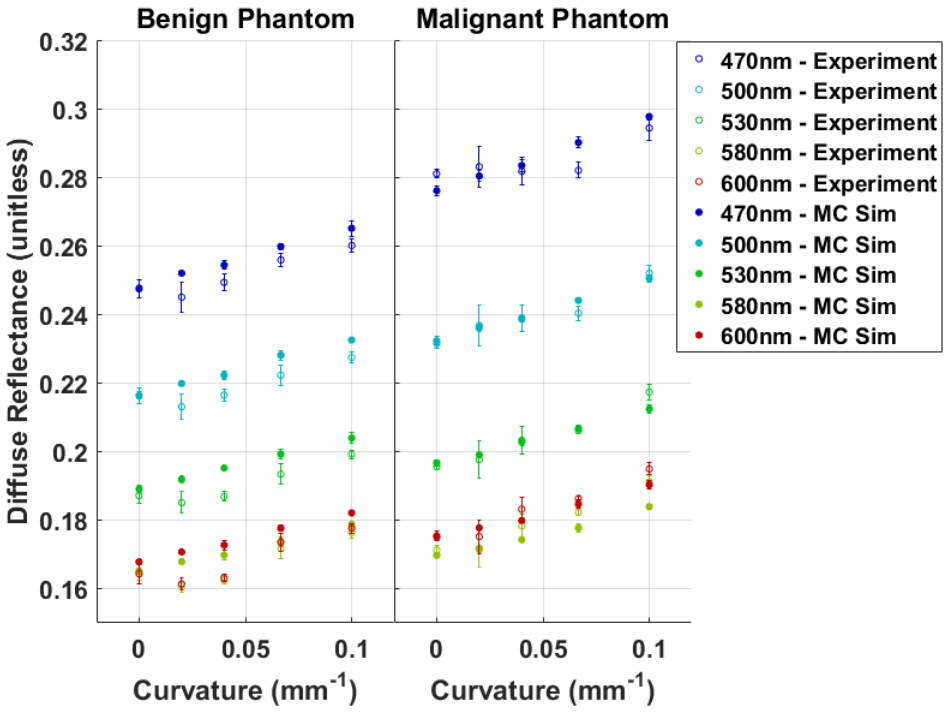

Figure 69. Benign (left) and malignant (right) phantom reflectance vs curvature, with simulation (filled circles) and experimental (open circles) results overlaid.

The reflectance data shows an increase in reflectance due to curvature for both experimental data and simulation. The highest degree of error between experiment and simulation occurs for the benign phantom at 600 nm, with a mean percent error of 3.56% across all curvatures at this wavelength. This wavelength shows the lowest reflection values of all compared μ_a and μ_s' pairs, and was subjected to the lowest optical power levels for all test points. However, the malignant phantom did not show the same level of error with nearly the same reflectance. The mean percent error at 600 nm for the malignant phantom was 1.36%, while the simulated reflectance was only an average of

4.2% higher as compared to the benign phantom. The mean percent error of the benign phantom exceeded that of the malignant phantom at all wavelengths. Additionally, the error observed in the benign phantom was always due to a higher simulated reflection than experimental reflection with only two exceptions: 480 nm and 490 nm for the flat curvature. As discussed in Chapter 5, the diffuse regime of scattering for a fixed source-detector distance is determined primarily by the reduced scattering coefficient. The value of μ_s' was lower for every wavelength in the benign phantom than the malignant phantom, with the highest μ_s' of the benign (8.382 cm^{-1} at 470 nm) almost 25% lower than the lowest μ_s' of the malignant phantom (10.94 cm^{-1} at 600 nm). Assuming that the physical scattering from the polystyrene microspheres in solution is well described by Mie theory, the major difference between simulation and experimental scattering is due to the difference in the modeled phase function. The Henyey-Greenstein phase function, used in the simulations, shows increased backscattering as compared to the Mie phase function, which would cause the simulation to show increased reflectance in the non-diffuse regime. The highest error between simulation and experiment occurs for the benign phantom at longer wavelengths, where μ_s' is the lowest. In addition, the simulation demonstrates a higher reflectance than the experimental results for these wavelengths. The difference in backscattering phase function would not cause such a discrepancy for the malignant phantom, which has a higher μ_s'. In the case of the

malignant phantom, the scattering is in the diffuse regime, where the Henyey-Greenstein and Mie phase functions are well matched.

6.2 Comparison of Crosstalk

Figure 70 shows the comparison of crosstalk reflectance for both experimental results and Monte Carlo simulations. For the benign phantom, the cross talk reflectance agrees well between simulation and experiment with a mean percent error of 4.85%.

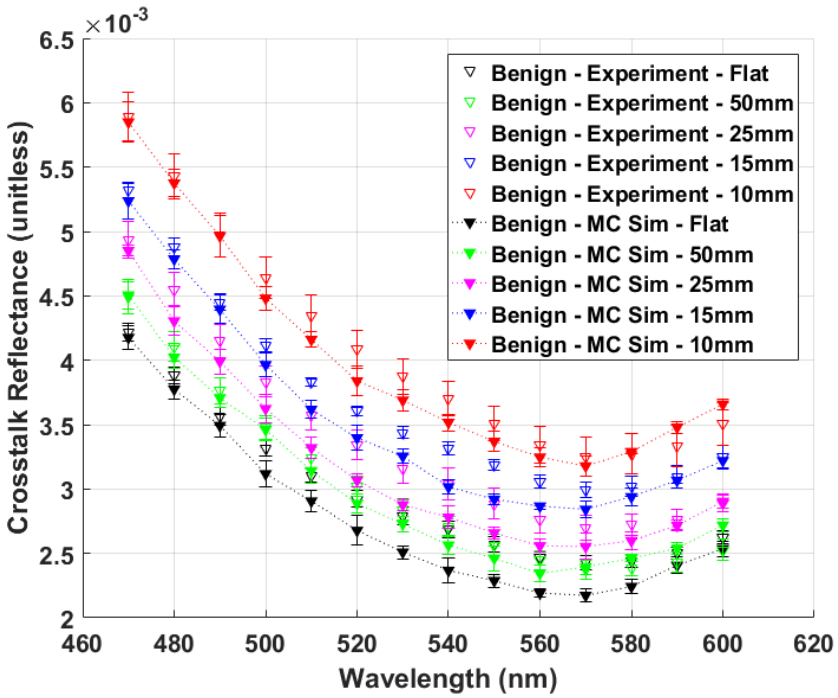

Figure 70. Cross talk reflectance of the benign phantom, overlaying experimental (open symbols) and simulated (filled symbols) data.

The mean percent error in cross talk for the benign phantom is higher than the error for the diffuse reflectance. In the MC simulations, the number of collected photons

at the cross talk detector was lower than at the diffuse reflectance detector. The accuracy of the MC simulation can be negatively impacted by the lower photon count, although repeated simulations showed high precision between trials (approximately 1.66% variation). In the experimental results, the recorded cross talk signal was far lower than the diffuse reflectance signal. However, the noise level, which includes light source variation and photodetector dark current, does not change regardless of which photodetector aperture is illuminated. The SNR, calculated as $SNR = 20\log_{10}\left(\frac{R}{\sigma_R}\right)$, where R is the reflectance signal and σ_R is the standard deviation of the reflectance signal, averaged 39.2dB for the benign phantom diffuse reflectance and 31.7dB for the benign phantom cross talk. Unlike the diffuse reflectance simulations, cross talk simulations do not suffer from the backscattering phase function mismatch between Henyey-Greenstein and Mie theoretical approaches. The cross talk source to detector spacing distance is 4.5mm, as compared to the diffuse reflectance source to detector spacing distance of 0.99mm. Thus, the cross talk scattering is within the diffuse regime.

The benign phantom cross talk also shows an increase in reflectance as a function of curvature, in both simulation and experimental results. Figure 71 shows the reflectance plotted as a function of curvature for of the benign phantom.

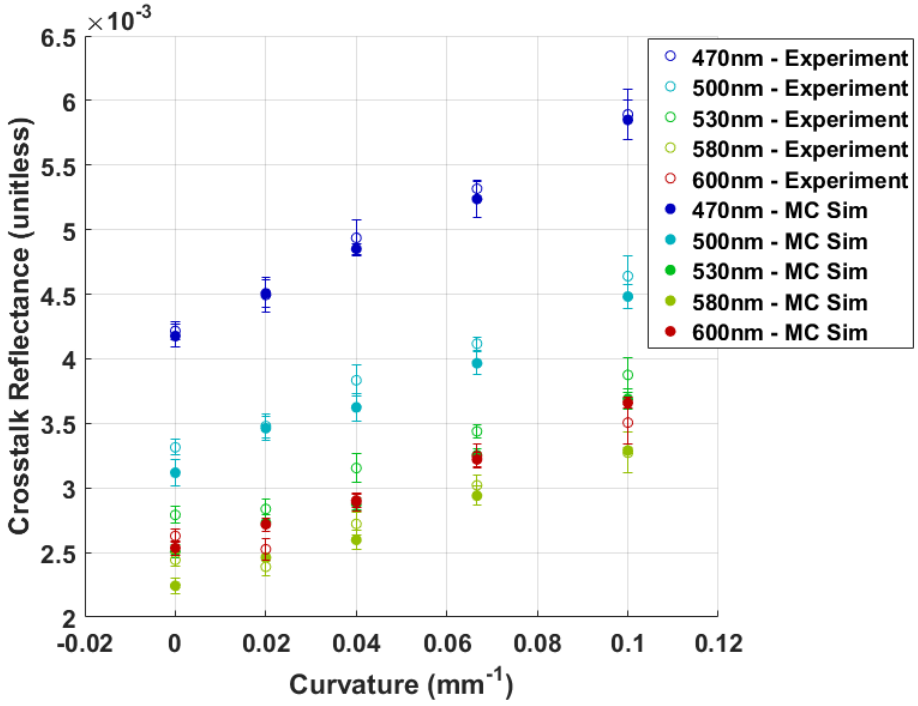

Figure 71. Benign phantom cross talk reflectance vs curvature, with simulation (filled circles) and experimental (open circles) results overlaid.

The simulated and experimental data both show an increase in cross talk signal of ~40% when the curvature increases from flat to a 10 mm radius of curvature. However, the cross talk as a percentage of the diffuse reflectance signal remains low, approximately 1.5% when flat and increasing to 2.0% at a 10 mm radius of curvature. While the simulations of the malignant phantom cross talk show an even higher increase in cross talk signal due to curvature, the simulated cross talk as a percentage of diffuse reflectance is even lower, approximately 0.1% when flat and 0.2% at a 10 mm radius of curvature.

In this chapter, the experimental results of diffuse reflectance from flat and flexed tissue-mimicking phantoms were compared to Monte Carlo simulations. The diffuse reflectance measurements show a mean percent error of 2.33% and 1.23% for the benign and malignant phantoms, respectively. The benign phantom mean percent error is higher than the malignant, which is likely due to the mismatch between backscattering calculations of the Mie and Henyey-Greenstein theoretical phase functions, amplified by the lower coefficient of scattering benign phantom. The mean percent error between the experimental results and theoretical model of the benign phantom crosstalk was 4.85. This error is likely due to the lower optical power reaching the detector due to crosstalk.

7. Conclusion and Future Work

This chapter summarizes the research presented in this thesis and discusses opportunities for future work and improvements in this field.

7.1 Conclusion

DRS can classify the optical properties of biological tissue, in particular the scattering and absorbing characteristics over the visible spectral range. The scattering and absorbing coefficients of biological tissue are strongly dependent on the tissue morphology and composition, including the concentration of chromophores such as beta-carotene and hemoglobin, which can be used to categorically identify the examined tissue. Using these extracted quantities, DRS has been shown, in some cases, to be able to differentiate between tissue types, providing non-invasive diagnostic information.

Traditional DRS probes consist of bundled pairs of source and detector optical fibers which are placed in contact with tissue to illuminate and collect the diffusely reflected spectra. Coupled with a spectrophotometer and broadband light source, the fiber-based DRS systems are limited in light collection efficiency due to the NA of the fiber, the fiber cladding diameter, and gaps between closely packed fibers. Many of these fiber-based probes are also limited to single-pixel DRS imaging – they only collect DRS measurements at a single point on a tissue surface. Higher pixel count imaging can be achieved by scanning a tissue surface with a single point detector [30], however, scanning increases the duration of the DRS measurement.

By replacing the collection optical fibers with a silicon photodiode on the tissue surface, the DRS collection efficiency increases. Silicon PDs have a larger NA and can be fabricated in any custom size and shape. This PD can also replace the separate photodetector or CCD traditionally coupled to the remote end of the collection optical fibers, which reduces the overall cost of the DRS system. Silicon PDs can be incorporated into arrays to enable simultaneous DRS imaging of multiple sites, and can be custom designed and fabricated in a PD array with through-silicon apertures [15].

These bulk silicon PD probes are not conformal to an uneven tissue surface; they are rigid and can cause inconsistent pressure regions or gaps between the detector and tissue surface. A flexible PD probe can reduce these gaps or high pressure regions by conforming to an uneven tissue surface. Additionally, the custom bulk silicon PDs have an exposed sidewall inside of the etched aperture, where the height of this sidewall is determined by the silicon wafer thickness. This exposed region increases the PD back illumination current since it provides extra surface area for photon absorption.

The work in this thesis addresses the challenges presented above. A thin film, single crystalline PD 2x1 pixel probe was fabricated on flexible Kapton film for tissue-conforming diffuse reflectance spectroscopy. The probe resolution matches that of the previously reported thick silicon array, with a 4.5 mm center-to-center pixel spacing. The two PDs measured a zero-bias responsivity of 0.20-0.34 A/W and 0.10-0.17 A/W for the wavelength range 470-600nm. The zero-bias dark current density for PD1 was 0.201

nA/cm^2, which results in a responsivity to dark current ratio of 0.99 – 1.69 cm^2/nW. PD2 demonstrated a higher dark current density of 8.28nA/cm^2, resulting in a responsivity to dark current ratio of 0.012-0.021cm^2/nW.

The flexible probe presented herein has little variation in responsivity and dark current characteristics when flexed, with responsivity changing only 0.61% over curvatures from flat to 10 mm radius. The zero bias dark current similarly showed little variation, with a range of 9-12 pA over all tested curvatures. Since the flexible probe characteristics were relatively unchanged with bending, no additional calibration or scaling was necessary for photocurrent measurements during flexure.

The flexible PD probe was tested on two liquid phantoms, each representing a benign or malignant breast tissue sample. The phantom optical properties covered a range of μ_a between 2.1-6.0 cm^{-1} and μ_s' between 6.9-13.3 cm^{-1}. The probe was tested by illuminating the tissue through the PD aperture, and measuring the photocurrent at five distinct curvatures from flat to a 10 mm radius. Reflectance was calculated by dividing the photocurrent during phantom measurement by the photocurrent recorded when illuminating a 99% reflectance standard. Although the reflectance between the two prepared phantoms had low contrast, the measurements taken on the flexible PD probe could be distinguished between both phantoms at all wavelengths for the same curvature. However, the DRS signal increases with curvature, and reflectance from the 15 mm and 10 mm curved benign phantoms increased beyond that of the flat malignant

phantom for $\lambda > 520$ nm. As long as the curvature is a known quantity, the increasing reflection can be accounted for without impeding differentiation between the reflectance from the two phantoms.

Crosstalk measurements were also taken for these curved phantoms. The cross talk signal similarly showed an increase in optical power for increasing radii of curvature. However, the increase in crosstalk was more pronounced for cases of very low crosstalk. The rate of increase is highest for higher μ_a and μ_s' values, where crosstalk is already reduced to nearly undetectable levels. For the experimental results on the benign phantom, the crosstalk signal increased by an average of 37.3% when the phantom surface curvature increased from flat to a 10 mm radius of curvature. The malignant phantom crosstalk showed an increase in signal due to curvature of 48.5% in Monte Carlo simulations. The experimental results for the malignant phantom were not measurable due to its low crosstalk signal.

Monte Carlo ray-tracing simulations were performed for the two phantoms at all five curvatures and at fourteen wavelengths, with five simulations of 10 million photons for each combination of curvature, wavelength, and phantom. The average variation in detected optical power across the five simulations was 0.42% for the diffuse reflectance signal and 2.38% for the crosstalk signal. The variation in optical power can be used to validate the MC simulation precision; with lower variation, the model provides repeatable results. Monte Carlo modeling precision can be improved by increasing the

photon count, at the expense of requiring additional computational resources or time. With low variation in the simulated data, further increases to the photon count will continue to require more computational resources, but will no longer improve precision. The MC simulations match the diffuse reflectance measurements very well, with a mean percent error between experiment and simulation of 2.33% for the benign and 1.23% for the malignant phantom at all simulated wavelengths and curvatures. For the longer wavelengths of the benign phantom, the MC simulation reflectance began to increase as compared to the experimental results. Since these test cases are very close to the non-diffuse regime of scattering, this divergence may be from the difference in backscattering between the simulated Henyey-Greenstein phase function and the assumed physical scattering phase function described by Mie theory. The benign phantom crosstalk measurement was also compared to simulation, with a mean percent error of 4.85%. Due to the low light levels and severely reduced SNR for the malignant phantom crosstalk, the experimental results were below the noise floor, and could not be compared to simulation.

7.2 Future Work

The work in this thesis motivates further exploration. These explorations include investigating stretchable materials, and incorporating light sources into the flexible array.

With a flexible diffuse reflectance spectroscopy probe, the surface curvature of examined tissue impacts the measured reflectance. Increasing curvature gives rise to increased measured reflectance. For the DRS measurements performed in this thesis, the increase in reflectance from a flat curvature to a 10 mm radius of curvature averaged 7.9%. If tissue types are compared without regard to the surface curvature, there is a reduction in signal contrast. The reflectance signal of a highly curved benign tissue surface approximates the reflectance of a malignant tissue at flat curvature, particularly at longer wavelengths (500 – 600 nm). To prevent a misdiagnosis due to this lower contrast, the surface curvature must be taken into account. This can be accomplished by introducing flexure sensors into the photodiode probe. Commercially available flex sensors, or electrogoniometers, include two overlapping resistive films, where the overlap area between the films changes due to curvature. The flexure can be calculated by measuring the electrical resistance. Alternatively, stacked thin film MOSFETs can measure flexure by using the relationship between lattice strain and drain current [121]. By incorporating either a resistance-based flex sensor or a chip-scale MOSFET flex sensor into the flexible probe, the surface curvature of a tissue sample can be measured simultaneously with DRS measurements. The surface curvature can then be included in Monte Carlo based optical property extraction techniques.

The flexible photodetector probe presented herein can conform to cylindrical bends at small radii, but other bending modes cannot be attained without deforming the

polymer substrate. For spherical bends, a stretchable substrate is required. The Kapton substrate used for the photodetector probe is considered flexible, but not stretchable. Alternative substrate materials, including polydimethylsiloxane (PDMS), could be used instead. Thermocompression bonding would be difficult or impossible on such a viscoelastic material. The substrate would undergo significant deformation before bonding pressure could be achieved. Instead, PDMS can be spin-coated to fully encapsulate fabricated thin film mesas on SOI wafers before removing the silicon handle. Once the handle is removed, the PDMS potentially serves as the permanent substrate material.

The test setup presented herein employs a separate optical fiber light source, manually aligned to one of the probe's photodetector apertures. The fiber source was fixed relative to the 3D printed test clamps, but the light source to PD aperture distance varied with curvature. Lower optical throughput was observed at higher radii of curvature due to the increased distance between the fiber tip and the PD aperture. To ensure that all tissue curvatures are illuminated evenly, light sources could be incorporated into the flexible probe. Optical fibers with 45° "side-firing" facets can be fixed along the flexible probe, with each fiber's facet aligned to an individual PD aperture. Alternatively, flexible or stretchable polymer optical waveguides can be fabricated using conventional photolithography techniques and incorporated into the detector probe. These light sources designs still require an external lamp and

spectrometer to provide illumination. To avoid including an external source, LEDs or laser diodes could be heterogeneously integrated with the detectors, allowing for the photodetector probe to perform in a standalone optoelectronic device role. With customized transimpedance amplifiers and laser/LED driver circuitry, this could enable a low-cost, conformal, DRS imaging system.

References

[1] A. Jemal, E. Ward, and M. J. Thun, "Recent trends in breast cancer incidence rates by age and tumor characteristics among U.S. women," *Breast Cancer Res.*, vol. 9, p. R28, 2007.

[2] A. Jemal, M. M. Center, C. DeSantis, and E. M. Ward, "Global Patterns of Cancer Incidence and Mortality Rates and Trends," *Cancer Epidemiol. Biomarkers Prev.*, vol. 19, no. 8, pp. 1893–1907, Aug. 2010.

[3] D. R. Mccready *et al.*, "Factors associated with local breast cancer recurrence after lumpectomy alone: Postmenopausal patients," *Ann. Surg. Oncol.*, vol. 7, no. 8, pp. 562–7, Sep. 2000.

[4] C. Kunos *et al.*, "Breast Conservation Surgery Achieving ≥ 2 mm Tumor-Free Margins Results in Decreased Local-Regional Recurrence Rates," *Breast J.*, vol. 12, no. 1, pp. 28–36, 2006.

[5] C. Dunne, J. P. Burke, M. Morrow, and M. R. Kell, "Effect of Margin Status on Local Recurrence After Breast Conservation and Radiation Therapy for Ductal Carcinoma In Situ," *J. Clin. Oncol.*, vol. 27, no. 10, pp. 1615–1620, Apr. 2009.

[6] M. S. Moran *et al.*, "Society of Surgical Oncology–American Society for Radiation Oncology Consensus Guideline on Margins for Breast-Conserving Surgery With Whole-Breast Irradiation in Stages I and II Invasive Breast Cancer," *Int. J. Radiat. Oncol.*, vol. 88, no. 3, pp. 553–564, Mar. 2014.

[7] L. Jacobs, "Positive Margins: The Challenge Continues for Breast Surgeons," *Ann. Surg. Oncol.*, vol. 15, no. 5, pp. 1271–1272, May 2008.

[8] Brender E, Burke A, and Glass RM, "Frozen section biopsy," *JAMA*, vol. 294, no. 24, pp. 3200–3200, Dec. 2005.

[9] T. Khamechian, J. Alizargar, and T. Mazoochi, "The Value of Touch Preparation for Rapid Diagnosis of Brain Tumors as an Intraoperative Consultation," *Iran. J. Med. Sci.*, vol. 37, no. 2, pp. 105–111, Jun. 2012.

[10] M. C. Smitt *et al.*, "The importance of the lumpectomy surgical margin status in long term results of breast conservation," *Cancer*, vol. 76, no. 2, pp. 259–267, 1995.

[11] L. G. Glance *et al.*, "The Surgical Mortality Probability Model: Derivation and Validation of a Simple Risk Prediction Rule for Noncardiac Surgery," *Ann. Surg.*, vol. 255, no. 4, pp. 696–702, Apr. 2012.

[12] I. J. Bigio and S. G. Bown, "Spectroscopic Sensing of Cancer and Cancer Therapy: Current Status of Translational Research," *Cancer Biol. Ther.*, vol. 3, no. 3, pp. 259–267, Mar. 2004.

[13] T. M. Bydlon *et al.*, "Performance metrics of an optical spectral imaging system for intra-operative assessment of breast tumor margins," *Opt. Express*, vol. 18, no. 8, p. 8058, Apr. 2010.

[14] B. Yu, J. Y. Lo, T. F. Kuech, G. M. Palmer, J. E. Bender, and N. Ramanujam, "Cost-effective diffuse reflectance spectroscopy device for quantifying tissue absorption and scattering in vivo," *J. Biomed. Opt.*, vol. 13, no. 6, pp. 60505-60505–3, 2008.

[15] S. Dhar *et al.*, "A diffuse reflectance spectral imaging system for tumor margin assessment using custom annular photodiode arrays," *Biomed. Opt. Express*, vol. 3, no. 12, p. 3211, Dec. 2012.

[16] B. S. Nichols, S. S. McCachren, G. Palmer, and N. Ramanujam, "Portable System for Wide-field, Sub-millimeter Functional Imaging of the Morphological Landscape of Breast Tumor Margins," 2016, p. TM4B.6.

[17] B. S. Nichols *et al.*, "A quantitative diffuse reflectance imaging (QDRI) system for comprehensive surveillance of the morphological landscape in breast tumor margins," *PLoS One*, vol. 10, no. 6, Jun. 2015.

[18] W. G. Zijlstra, A. Buursma, H. E. Falke, and J. F. Catsburg, "Spectrophotometry of hemoglobin: absorption spectra of rat oxyhemoglobin, deoxyhemoglobin, carboxyhemoglobin, and methemoglobin," *Comp. Biochem. Physiol. Part B Comp. Biochem.*, vol. 107, no. 1, pp. 161–166, Jan. 1994.

[19] F. P. Zscheile, J. W. White, B. W. Beadle, and J. R. Roach, "The preparation and absorption spectra of five pure carotenoid pigments," *Plant Physiol.*, vol. 17, no. 3, pp. 331–346, Jul. 1942.

[20] S. L. Jacques, "Optical properties of biological tissues: a review," *Phys. Med. Biol.*, vol. 58, no. 11, p. R37, Jun. 2013.

[21] J. M. Schmitt and G. Kumar, "Optical Scattering Properties of Soft Tissue: A Discrete Particle Model," *Appl. Opt.*, vol. 37, no. 13, p. 2788, May 1998.

[22] S. A. Prahl, M. Keijzer, S. L. Jacques, and A. Welch, "A Monte Carlo model of light propagation in tissue," *Dosim. Laser Radiat. Med. Biol.*, vol. 5, pp. 102--111, 1989.

[23] Z. Volynskaya *et al.*, "Diagnosing breast cancer using diffuse reflectance spectroscopy and intrinsic fluorescence spectroscopy," *J. Biomed. Opt.*, vol. 13, no. 2, pp. 24012-24012–9, 2008.

[24] J. E. Bender *et al.*, "A Robust Monte Carlo Model for the Extraction of Biological Absorption and Scattering In Vivo," *IEEE Trans. Biomed. Eng.*, vol. 56, no. 4, pp. 960–968, 2009.

[25] G. Zonios, J. Bykowski, and N. Kollias, "Skin Melanin, Hemoglobin, and Light Scattering Properties can be Quantitatively Assessed In Vivo Using Diffuse Reflectance Spectroscopy," *J. Invest. Dermatol.*, vol. 117, no. 6, pp. 1452–1457, Dec. 2001.

[26] N. Subhash, J. R. Mallia, S. S. Thomas, A. Mathews, P. Sebastian, and J. Madhavan, "Oral cancer detection using diffuse reflectance spectral ratio R540⁄R575 of oxygenated hemoglobin bands," *J. Biomed. Opt.*, vol. 11, no. 1, pp. 14018-14018–6, 2006.

[27] R. A. Schwarz, W. Gao, D. Daye, M. D. Williams, R. Richards-Kortum, and A. M. Gillenwater, "Autofluorescence and diffuse reflectance spectroscopy of oral epithelial tissue using a depth-sensitive fiber-optic probe," *Appl. Opt.*, vol. 47, no. 6, p. 825, Feb. 2008.

[28] G. Zonios *et al.*, "Diffuse reflectance spectroscopy of human adenomatous colon polyps in vivo," *Appl. Opt.*, vol. 38, no. 31, p. 6628, Nov. 1999.

[29] S. Kennedy *et al.*, "Optical breast cancer margin assessment: an observational study of the effects of tissue heterogeneity on optical contrast," *Breast Cancer Res.*, vol. 12, p. R91, 2010.

[30] N. Lue *et al.*, "Portable Optical Fiber Probe-Based Spectroscopic Scanner for Rapid Cancer Diagnosis: A New Tool for Intraoperative Margin Assessment," *PLOS ONE*, vol. 7, no. 1, p. e30887, Jan. 2012.

[31] M. G. Nichols, E. L. Hull, and T. H. Foster, "Design and testing of a white-light, steady-state diffuse reflectance spectrometer for determination of optical properties of highly scattering systems," *Appl. Opt.*, vol. 36, no. 1, p. 93, Jan. 1997.

[32] A. Garcia-Uribe, J. Zou, M. Duvic, J. H. Cho-Vega, V. G. Prieto, and L. V. Wang, "In Vivo Diagnosis of Melanoma and Nonmelanoma Skin Cancer Using Oblique Incidence Diffuse Reflectance Spectrometry," *Cancer Res.*, vol. 72, no. 11, pp. 2738–2745, Jun. 2012.

[33] H.-W. Wang, J.-K. Jiang, C.-H. Lin, J.-K. Lin, G.-J. Huang, and J.-S. Yu, "Diffuse reflectance spectroscopy detects increased hemoglobin concentration and decreased oxygenation during colon carcinogenesis from normal to malignant tumors," *Opt. Express*, vol. 17, no. 4, p. 2805, Feb. 2009.

[34] H. L. Fu, B. Yu, J. Y. Lo, G. M. Palmer, T. F. Kuech, and N. Ramanujam, "A low-cost, portable, and quantitative spectral imaging system for application to biological tissues," *Opt. Express*, vol. 18, no. 12, p. 12630, Jun. 2010.

[35] S. Dhar, J. Y. Lo, B. Yu, M. A. Brooke, N. Ramanujam, and N. M. Jokerst, "Custom annular photodetector arrays for breast cancer margin assessment using diffuse reflectance spectroscopy," in *2011 IEEE Biomedical Circuits and Systems Conference (BioCAS)*, 2011, pp. 440–443.

[36] E. M. C. Hillman, D. A. Boas, A. M. Dale, and A. K. Dunn, "Laminar optical tomography: demonstration of millimeter-scale depth-resolved imaging in turbid media," *Opt. Lett.*, vol. 29, no. 14, p. 1650, Jul. 2004.

[37] H. Cen and R. Lu, "Quantification of the optical properties of two-layer turbid materials using a hyperspectral imaging-based spatially-resolved technique," *Appl. Opt.*, vol. 48, no. 29, p. 5612, Oct. 2009.

[38] O. Senlik and N. M. Jokerst, "Concentric Multipixel Silicon Photodiode Array Probes for Spatially Resolved Diffuse Reflectance Spectroscopy," *IEEE J. Sel. Top. Quantum Electron.*, vol. 22, no. 3, pp. 7–12, May 2016.

[39] O. Senlik, G. Greening, T. J. Muldoon, and N. M. Jokerst, "Spatially resolved diffuse reflectance spectroscopy of two-layer turbid media by densely packed multi-pixel photodiode reflectance probe," in *SPIE BiOS*, 2016, vol. 9700, p. 97000O–97000O–6.

[40] N. Rajaram, T. H. Nguyen, and J. W. Tunnell, "Lookup table–based inverse model for determining optical properties of turbid media," *J. Biomed. Opt.*, vol. 13, no. 5, pp. 50501-50501–3, 2008.

[41] B. S. Nichols, N. Rajaram, and J. W. Tunnell, "Performance of a lookup table-based approach for measuring tissue optical properties with diffuse optical spectroscopy," *J. Biomed. Opt.*, vol. 17, no. 5, pp. 0570011–0570018, 2012.

[42] R. Hennessy, S. L. Lim, M. K. Markey, and J. W. Tunnell, "Monte Carlo lookup table-based inverse model for extracting optical properties from tissue-simulating phantoms using diffuse reflectance spectroscopy," *J. Biomed. Opt.*, vol. 18, no. 3, pp. 037003–037003, 2013.

[43] D. Contini, F. Martelli, and G. Zaccanti, "Photon migration through a turbid slab described by a model based on diffusion approximation. I. Theory," *Appl. Opt.*, vol. 36, no. 19, pp. 4587–4599, Jul. 1997.

[44] R. M. P. Doornbos, R. Lang, M. C. Aalders, F. W. Cross, and H. J. C. M. Sterenborg, "The determination of in vivo human tissue optical properties and absolute chromophore concentrations using spatially resolved steady-state diffuse reflectance spectroscopy," *Phys. Med. Biol.*, vol. 44, no. 4, p. 967, 1999.

[45] C. Zhu, G. M. Palmer, T. M. Breslin, J. Harter, and N. Ramanujam, "Diagnosis of breast cancer using diffuse reflectance spectroscopy: Comparison of a Monte Carlo versus partial least squares analysis based feature extraction technique," *Lasers Surg. Med.*, vol. 38, no. 7, pp. 714–724, Aug. 2006.

[46] G. M. Palmer and N. Ramanujam, "Monte Carlo-based inverse model for calculating tissue optical properties. Part I: Theory and validation on synthetic phantoms," *Appl. Opt.*, vol. 45, no. 5, p. 1062, 2006.

[47] G. M. Palmer, C. Zhu, T. M. Breslin, F. Xu, K. W. Gilchrist, and N. Ramanujam, "Monte Carlo-based inverse model for calculating tissue optical properties Part II: Application to breast cancer diagnosis," *Appl. Opt.*, vol. 45, no. 5, p. 1072, Feb. 2006.

[48] A. B. Chagpar, R. C. G. Martin II, L. J. Hagendoorn, C. Chao, and K. M. McMasters, "Lumpectomy margins are affected by tumor size and histologic subtype but not by biopsy technique," *Am. J. Surg.*, vol. 188, no. 4, pp. 399–402, Oct. 2004.

[49] P. I. Tartter *et al.*, "Lumpectomy margins, reexcision, and local recurrence of breast cancer," *Am. J. Surg.*, vol. 179, no. 2, pp. 81–85, Feb. 2000.

[50] H. Shangguan, S. A. Prahl, S. L. Jacques, L. W. Casperson, and K. W. Gregory, "Pressure effects on soft tissues monitored by changes in tissue optical properties," in *BiOS'98 International Biomedical Optics Symposium*, 1998, vol. 3254, pp. 366–371.

[51] R. Reif, M. S. Amorosino, K. W. Calabro, O. A'Amar, S. K. Singh, and I. J. Bigio, "Analysis of changes in reflectance measurements on biological tissues subjected to different probe pressures," *J. Biomed. Opt.*, vol. 13, no. 1, pp. 10502-10502–3, 2008.

[52] L. Lim, B. Nichols, N. Rajaram, and J. W. Tunnell, "Probe pressure effects on human skin diffuse reflectance and fluorescence spectroscopy measurements," *J. Biomed. Opt.*, vol. 16, no. 1, pp. 11012-11012–9, 2011.

[53] P. Bhattacharya, *Semiconductor optoelectronic devices*, 2nd ed. Upper Saddle River, NJ: Prentice Hall, 1997.

[54] S.-W. Seo, S.-Y. Cho, and N. M. Jokerst, "A thin-film laser, polymer waveguide, and thin-film photodetector cointegrated onto a silicon substrate," *IEEE Photonics Technol. Lett.*, vol. 17, no. 10, pp. 2197–2199, Oct. 2005.

[55] L. Luan, R. D. Evans, N. M. Jokerst, and R. B. Fair, "Integrated Optical Sensor in a Digital Microfluidic Platform," *IEEE Sens. J.*, vol. 8, no. 5, pp. 628–635, May 2008.

[56] J. Brouckaert, G. Roelkens, D. V. Thourhout, and R. Baets, "Thin-Film III–V Photodetectors Integrated on Silicon-on-Insulator Photonic ICs," *J. Light. Technol.*, vol. 25, no. 4, pp. 1053–1060, Apr. 2007.

[57] F. Fixe, V. Chu, D. M. F. Prazeres, and J. P. Conde, "An on-chip thin film photodetector for the quantification of DNA probes and targets in microarrays," *Nucleic Acids Res.*, vol. 32, no. 9, pp. e70–e70, May 2004.

[58] A. Afzalian and D. Flandre, "Physical modeling and design of thin-film SOI lateral PIN photodiodes," *IEEE Trans. Electron Devices*, vol. 52, no. 6, pp. 1116–1122, Jun. 2005.

[59] D. K. Schroder, *Semiconductor material and device chacterization*. John Wiley & Sons, 2006.

[60] J. Yoon *et al.*, "Ultrathin silicon solar microcells for semitransparent, mechanically flexible and microconcentrator module designs," *Nat. Mater.*, vol. 7, no. 11, pp. 907–915, Nov. 2008.

[61] H. C. Ko *et al.*, "A hemispherical electronic eye camera based on compressible silicon optoelectronics," *Nature*, vol. 454, no. 7205, pp. 748–753, Aug. 2008.

[62] S. Dhar and N. M. Jokerst, "High responsivity, low dark current, large area, heterogenously bonded annular thin-film silicon photodetectors," in *2012 IEEE Photonics Conference (IPC)*, 2012, pp. 378–379.

[63] M. A. Hopcroft, W. D. Nix, and T. W. Kenny, "What is the Young's Modulus of Silicon?," *J. Microelectromechanical Syst.*, vol. 19, no. 2, pp. 229–238, Apr. 2010.

[64] J. D. Wu, C. Y. Huang, and C. C. Liao, "Fracture strength characterization and failure analysis of silicon dies," *Microelectron. Reliab.*, vol. 43, no. 2, pp. 269–277, Feb. 2003.

[65] D. Armani, C. Liu, and N. Aluru, "Re-configurable fluid circuits by PDMS elastomer micromachining," in *Twelfth IEEE International Conference on Micro Electro Mechanical Systems, 1999. MEMS '99*, 1999, pp. 222–227.

[66] T. K. Kim, J. K. Kim, and O. C. Jeong, "Measurement of nonlinear mechanical properties of PDMS elastomer," *Microelectron. Eng.*, vol. 88, no. 8, pp. 1982–1985, Aug. 2011.

[67] J. M. Gere, *Mechanics of Materials*, 6th ed. Brooks/Cole - Thomson Learning, 2004.

[68] C. Landesberger, G. Klink, G. Schwinn, and R. Aschenbrenner, "New dicing and thinning concept improves mechanical reliability of ultra thin silicon," in *International Symposium on Advanced Packaging Materials: Processes, Properties and Interfaces, 2001. Proceedings*, 2001, pp. 92–97.

[69] E. Yablonovitch, T. Gmitter, J. P. Harbison, and R. Bhat, "Extreme selectivity in the lift-off of epitaxial GaAs films," *Appl. Phys. Lett.*, vol. 51, no. 26, pp. 2222–2224, 1987.

[70] J.-H. Ahn *et al.*, "High-speed mechanically flexible single-crystal silicon thin-film transistors on plastic substrates," *IEEE Electron Device Lett.*, vol. 27, no. 6, pp. 460–462, 2006.

[71] K. J. Lee *et al.*, "Large-Area, Selective Transfer of Microstructured Silicon: A Printing- Based Approach to High-Performance Thin-Film Transistors Supported on Flexible Substrates," *Adv. Mater.*, vol. 17, no. 19, pp. 2332–2336, Oct. 2005.

[72] L. Zhou, S. Jung, E. Brandon, and T. N. Jackson, "Flexible substrate micro-crystalline silicon and gated amorphous silicon strain sensors," *IEEE Trans. Electron Devices*, vol. 53, no. 2, pp. 380–385, Feb. 2006.

[73] M. Mativenga, M. H. Choi, J. W. Choi, and J. Jang, "Transparent flexible circuits based on amorphous-indium--gallium--zinc--oxide thin-film transistors," *IEEE Electron Device Lett.*, vol. 32, no. 2, pp. 170–172, Feb. 2011.

[74] F. C. Krebs, "Polymer solar cell modules prepared using roll-to-roll methods: Knife-over-edge coating, slot-die coating and screen printing," *Sol. Energy Mater. Sol. Cells*, vol. 93, no. 4, pp. 465–475, Apr. 2009.

[75] F. C. Krebs *et al.*, "A complete process for production of flexible large area polymer solar cells entirely using screen printing—First public demonstration," *Sol. Energy Mater. Sol. Cells*, vol. 93, no. 4, pp. 422–441, Apr. 2009.

[76] R. H. French *et al.*, "Optical properties of materials for concentrator photovoltaic systems," in *2009 34th IEEE Photovoltaic Specialists Conference (PVSC)*, 2009, pp. 000394–000399.

[77] R. R. Rye, A. J. Howard, and A. J. Ricco, "Photolithographic metallization of fluorinated polymers," *Thin Solid Films*, vol. 262, no. 1–2, pp. 73–83, Jun. 1995.

[78] A. Celerier and J. Machet, "Metallization of polytetrafluoroethylene substrates by ion plating," *Thin Solid Films*, vol. 148, no. 3, pp. 323–332, Apr. 1987.

[79] C.-A. Chang, J. E. E. Baglin, A. G. Schrott, and K. C. Lin, "Enhanced Cu-Teflon adhesion by presputtering prior to the Cu deposition," *Appl. Phys. Lett.*, vol. 51, no. 2, pp. 103–105, Jul. 1987.

[80] H.-C. Yuan *et al.*, "Flexible photodetectors on plastic substrates by use of printing transferred single-crystal germanium membranes," *Appl. Phys. Lett.*, vol. 94, no. 1, p. 13102, Jan. 2009.

[81] R. Shabannia and H. A. Hassan, "Characteristics of photoconductive UV photodetector based on ZnO nanorods grown on polyethylene naphthalate substrate by chemical bath deposition method," *Electron. Mater. Lett.*, vol. 10, no. 4, pp. 837–843, Jul. 2014.

[82] D. Chen and H. G. Zachmann, "Glass transition temperature of copolyesters of PET, PEN and PHB as determined by dynamic mechanical analysis," *Polymer*, vol. 32, no. 9, pp. 1612–1621, 1991.

[83] DuPont, "DuPont Kapton HN Technical Data Sheet." Apr-2011.

[84] DuPont Teijin Films, "Mylar Optical Properties." Jun-2003.

[85] P. W. Barth, S. L. Bernard, and J. B. Angell, "Flexible circuit and sensor arrays fabricated by monolithic silicon technology," *IEEE Trans. Electron Devices*, vol. 32, no. 7, pp. 1202–1205, 1985.

[86] N. Marin and Y. Serruys, "Diffusion of metals deposited on a polyimide film (Kapton) under and out of irradiation," *Nucl. Instrum. Methods Phys. Res. Sect. B Beam Interact. Mater. At.*, vol. 105, no. 1–4, pp. 175–180, Nov. 1995.

[87] Y.-H. Tseng, Y.-J. Huang, M.-K. Chen, and Y.-L. Lin, "Micro-scale Cu metallization on polyimide substrate for high-speed interconnects," in *2012 IEEE Global High Tech Congress on Electronics (GHTCE)*, 2012, pp. 139–140.

[88] S. Ikeda, Y. Kobayashi, Y. Fujiwara, K. Akamatsu, and H. Nawafune, "All-Wet Metallization Process for Transparent Polyimide Films," *J. Phys. Conf. Ser.*, vol. 417, no. 1, p. 12019, Mar. 2013.

[89] Y. B. Park, I. S. Park, and J. Yu, "Interfacial fracture energy measurements in the Cu/Cr/polyimide system," *Mater. Sci. Eng. A*, vol. 266, no. 1–2, pp. 261–266, Jun. 1999.

[90] J. Y. Song and J. Yu, "Analysis of the T-peel strength in a Cu/Cr/Polyimide system," *Acta Mater.*, vol. 50, no. 16, pp. 3985–3994, Sep. 2002.

[91] Y. Zhang *et al.*, "Mechanics of ultra-stretchable self-similar serpentine interconnects," *Acta Mater.*, vol. 61, no. 20, pp. 7816–7827, Dec. 2013.

[92] I. Christiaens, G. Roelkens, K. D. Mesel, D. V. Thourhout, and R. Baets, "Thin-Film Devices Fabricated With Benzocyclobutene Adhesive Wafer Bonding," *J. Light. Technol.*, vol. 23, no. 2, p. 517, Feb. 2005.

[93] J. Ouyang and Y. Yang, "Conducting Polymer as Transparent Electric Glue," *Adv. Mater.*, vol. 18, no. 16, pp. 2141–2144, Aug. 2006.

[94] Z. Lai and J. Liu, "Anisotropically conductive adhesive flip-chip bonding on rigid and flexible printed circuit substrates," *IEEE Trans. Compon. Packag. Manuf. Technol. Part B*, vol. 19, no. 3, pp. 644–660, Aug. 1996.

[95] C. H. Tsau, S. M. Spearing, and M. A. Schmidt, "Fabrication of wafer-level thermocompression bonds," *J. Microelectromechanical Syst.*, vol. 11, no. 6, pp. 641–647, Dec. 2002.

[96] K. N. Chen, C. S. Tan, A. Fan, and R. Reif, "Morphology and Bond Strength of Copper Wafer Bonding," *Electrochem. Solid-State Lett.*, vol. 7, no. 1, pp. G14–G16, Jan. 2004.

[97] S. K. Kang, "Thermocompression bonding of aluminum bumps in TAB applications," in *48th IEEE Electronic Components & Technology Conference, 1998*, 1998, pp. 1305–1310.

[98] X. F. Ang, A. T. Lin, J. Wei, Z. Chen, and C. C. Wong, "Low Temperature Copper-Copper Thermocompression Bonding," in *Electronics Packaging Technology Conference, 2008. EPTC 2008. 10th*, 2008, pp. 399–404.

[99] T. J. Farrell, M. S. Patterson, and B. Wilson, "A diffusion theory model of spatially resolved, steady-state diffuse reflectance for the noninvasive determination of tissue optical properties invivo," *Med. Phys.*, vol. 19, no. 4, pp. 879–888, Jul. 1992.

[100] S. Dhar, "Development of Custom Imaging Arrays for Biomedical Spectral Imaging Systems," Duke University, 2012.

[101] J. Y. Lo *et al.*, "Diffuse reflectance spectral imaging for breast tumor margin assessment," in *SPIE BiOS*, 2012, vol. 8214, pp. 821407-821407–7.

[102] J. Y. Lo *et al.*, "Wavelength Optimization for Quantitative Spectral Imaging of Breast Tumor Margins," *PLOS ONE*, vol. 8, no. 4, p. e61767, Apr. 2013.

[103] S. Larouche and L. Martinu, "OpenFilters: open-source software for the design, optimization, and synthesis of optical filters," *Appl. Opt.*, vol. 47, no. 13, p. C219, May 2008.

[104] H. A. MacLeod, *Thin-Film Optical Filters, Third Edition*. CRC Press, 2001.

[105] M. Gonzalez, F. Axisa, M. V. Bulcke, D. Brosteaux, B. Vandevelde, and J. Vanfleteren, "Design of metal interconnects for stretchable electronic circuits," *Microelectron. Reliab.*, vol. 48, no. 6, pp. 825–832, Jun. 2008.

[106] "PI-2525, PI-2555, PI-2574 Non-photodefineable, dry etch | HD MicroSystems™." [Online]. Available: http://www.hdmicrosystems.com/ec/liquid-polyimides-and-pbo-precursors/products/sub-products/pi-2500-series.html. [Accessed: 25-Sep-2016].

[107] W. N. Sharpe, J. Pulskamp, D. S. Gianola, C. Eberl, R. G. Polcawich, and R. J. Thompson, "Strain Measurements of Silicon Dioxide Microspecimens by Digital Imaging Processing," *Exp. Mech.*, vol. 47, no. 5, pp. 649–658, Feb. 2007.

[108] S. Dhar, D. M. Miller, and N. M. Jokerst, "High responsivity, low dark current, heterogeneously integrated thin film Si photodetectors on rigid and flexible substrates," *Opt. Express*, vol. 22, no. 5, p. 5052, Mar. 2014.

[109] T.-K. Chuang, A. Usenko, and J. Cites, "The Study of the Bonding Energy on Silicon-to-Glass Wafer Bonding," *ECS Trans.*, vol. 33, no. 4, pp. 501–507, Oct. 2010.

[110] K.-M. Chen, T.-H. Wang, J.-S. King, and A. Hung, "Effect of imidization temperature on properties of polymide films," *J. Appl. Polym. Sci.*, vol. 48, no. 2, pp. 291–297, Apr. 1993.

[111] N. Nishida, H. Yano, T. Nishida, T. Kamura, and M. Kojiro, "Angiogenesis in Cancer," *Vasc. Health Risk Manag.*, vol. 2, no. 3, pp. 213–219, Sep. 2006.

[112] C. Mätzler, "MATLAB functions for Mie scattering and absorption, version 2," Institut für Angewandte Physik, Bern, Switzerland, Res. Rep. 2002-11, Aug. 2002.

[113] C. Zhu and Q. Liu, "Review of Monte Carlo modeling of light transport in tissues," *J. Biomed. Opt.*, vol. 18, no. 5, pp. 050902–050902, 2013.

[114] A. E. Profio, "Light transport in tissue," *Appl. Opt.*, vol. 28, no. 12, p. 2216, Jun. 1989.

[115] S. T. Flock, M. S. Patterson, B. C. Wilson, and D. R. Wyman, "Monte Carlo modeling of light propagation in highly scattering tissues. I. Model predictions and comparison with diffusion theory," *IEEE Trans. Biomed. Eng.*, vol. 36, no. 12, pp. 1162–1168, Dec. 1989.

[116] L. Wang and S. L. Jacques, "Hybrid model of Monte Carlo simulation and diffusion theory for light reflectance by turbid media," *J. Opt. Soc. Am. A Opt. Image Sci. Vis.*, vol. 10, no. 8, pp. 1746–1752, Aug. 1993.

[117] D. Toublanc, "Henyey–Greenstein and Mie phase functions in Monte Carlo radiative transfer computations," *Appl. Opt.*, vol. 35, no. 18, p. 3270, Jun. 1996.

[118] W. J. Wiscombe, "Improved Mie scattering algorithms," *Appl. Opt.*, vol. 19, no. 9, p. 1505, May 1980.

[119] K. W. Calabro and I. J. Bigio, "Influence of the phase function in generalized diffuse reflectance models: review of current formalisms and novel observations," *J. Biomed. Opt.*, vol. 19, no. 7, pp. 075005–075005, 2014.

[120] F. Bevilacqua and C. Depeursinge, "Monte Carlo study of diffuse reflectance at source–detector separations close to one transport mean free path," *J. Opt. Soc. Am. A*, vol. 16, no. 12, p. 2935, Dec. 1999.

[121] S. Endler, S. Ferwana, H. Rempp, C. Harendt, and J. N. Burghartz, "Two-Dimensional Flex Sensor Exploiting Stacked Ultrathin Chips," *IEEE Electron Device Lett.*, vol. 33, no. 3, pp. 444–446, Mar. 2012.

Biography

David was born in Stamford, Connecticut on February 28, 1987. He received his BS and MS, both in Electrical Engineering, from Northwestern University in June 2008. David was employed by GE Aviation in Lynn, MA from 2008-2010 and Boston Engineering Corporation in Waltham, MA from 2010 to 2012. He then joined the doctoral program at Duke in 2012, with research specializing in thin film flexible optoelectronic devices for health care diagnostics.

Publication History

Sulochana Dhar, **David M. Miller**, and Nan M. Jokerst, "High responsivity, low dark current, heterogeneously integrated thin film Si photodetectors on rigid and flexible substrates," Optics Express 22, 5052-5059 (2014).

Manuscript in Preparation

David M. Miller and Nan M. Jokerst, "Flexible Silicon Sensors for Diffuse Reflectance Spectroscopy of Tissue."